Experimental Investigation of Fan-Stage Interaction Noise of a Turbofan Engine

Sidharth Krishnan Kalyani

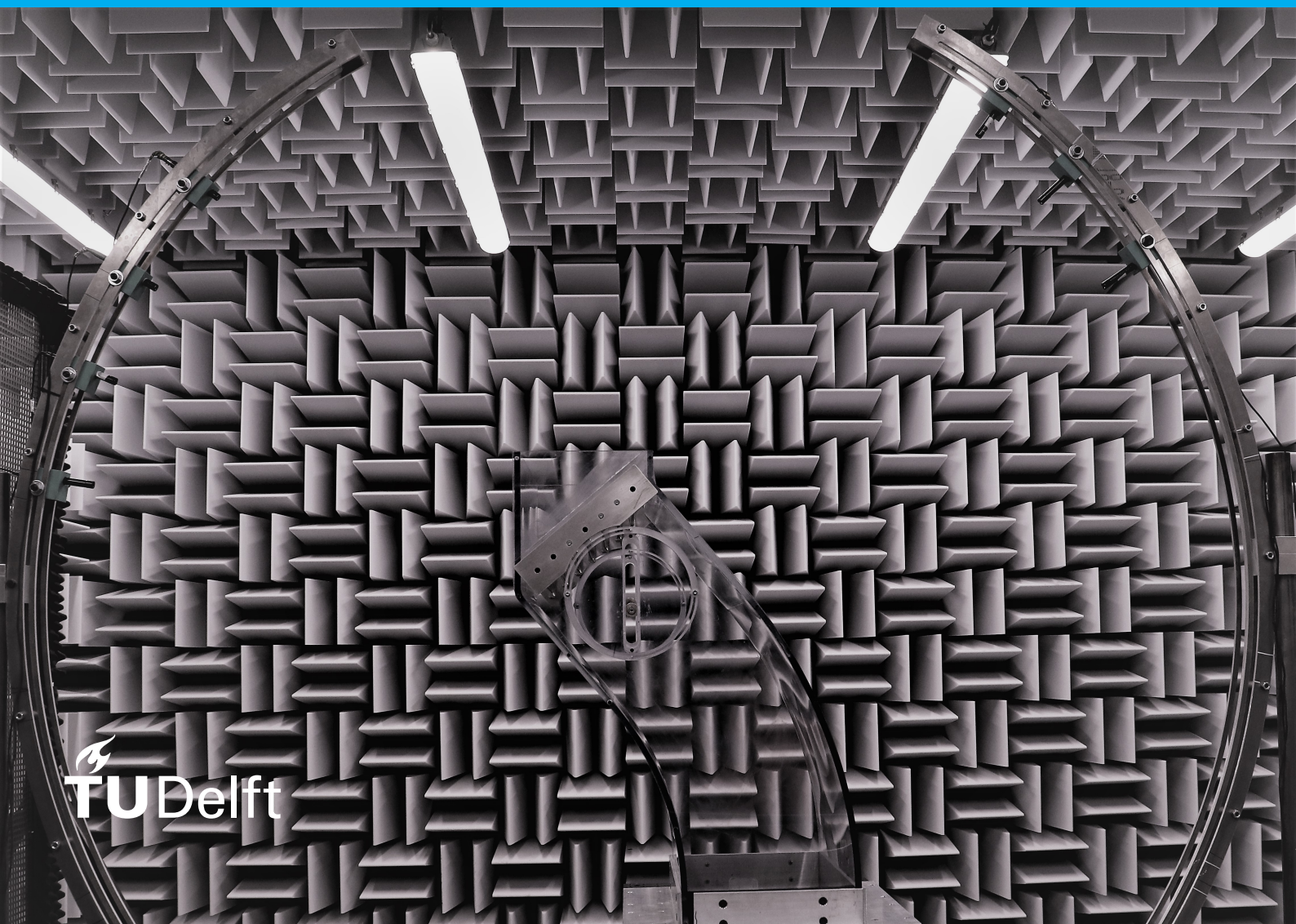

Experimental Investigation of Fan-Stage Interaction Noise of a Turbofan Engine

by

Sidharth Krishnan Kalyani

to obtain the degree of Master of Science
at the Delft University of Technology,

Student number:	4737237	
Project duration:	December 1, 2018 – September 18, 2019	
Thesis committee:	Prof. Dr. Damiano Casalino,	TU Delft, Chair- Aeroacoustics, Thesis committee head
	Dr. Marios Kotsonis,	TU Delft, Aerodynamics, External committee member
	Dr. Daniele Ragni,	TU Delft, Aeroacoustics, Responsible thesis supervisor
	MSc. Christopher Teruna,	TU Delft, Aeroacoustics, Supervisor

An electronic version of this thesis is available at http://repository.tudelft.nl/.

Acknowledgement

If there is one thing I've learned in Masters, it's living the day as it comes and making the most out of it. There were days where I've counted minutes, and there were days which just flew by, it all feels like a two year dream. A dream that was filled with learnings of life and one of the very few which were realized. A dream, which I might not dream again, but the characters in this dream of mine are ever etched in my heart and soul.

Gratitude is one of the life hacks which I use to earn happiness points. Well yeah, it works for me. I was very kind to myself these 2 years, which I'm not usually, so my first expression of gratitude is towards me. Thank you for doing this, you are awesome and you know it. Amma & Appa, I love you both, and I couldn't have done this without your support.

Knowledge is like a hurricane. It's all turbulent and has the capacity to break you until you get to the eye, where it's calm. I hope one day, from the guidance and knowledge imparted to me by Chris, Dani, Damiano, Francesco, Tercio, I can set my course towards the eye of the storm. A special mention to Ale and Salil, without whom, my experimental campaign and post-processing would have been a headache. You guys have been very supportive of my stupidity, answering the same questions (only worded differently hahaha :P) and I'm very much grateful to have had you all during my 9 month venture into Acoustics and to many more years to come, hopefully.

I am indebted to the lab assistants, Stefan and Emile, who worked overtime just so I could complete my experiments within the given time-frame. I learnt a great deal about the practicalities of performing an experiment, and I will never forget them. I'd also like to thank Rob for manufacturing the equipments on time. You guys rock.

My munchkins, the House of Aerodynamics, you guys are the best. From doing assignments to spending quality time out, to all the poker nights and cricket evenings, you guys gave me a lot of memories and I am smiling at them as I type this (yes, I smile too, fyi). To Sampy, Raman, BJ, Thakidadom, T-B, Kushu, Lankesh, Ashley, Shru, Vishal, . (not a typo), Santhosh, Rajath, Aditi, Sniggy, Aps and all my other well-wishers from all over the world, thank you for making these 2 years bearable. I bet a 1000 bucks and I say this: These years wouldn't have been smooth without you in it.

Sidharth
Delft, September 2019

Abstract

Future designs of turbofan engines are heading towards High By-Pass Ratios (HBPR) to satisfy the requirements of improving the overall efficiency, but there is an inherent acoustic penalty related to this. An increase in the by-pass ratio imposes structural constraints on the engine leading to a decrease in the axial distance between the rotor and the stator. The turbulent fan wake thus becomes more coherent on the OGVs, resulting in an increased tonal noise production. A test setup which can emulate the noise production mechanisms on a smaller scale and study the noise mitigation process is currently lacking.

A characterization experiment of such a simplified test setup to assess its ability to predict the vortex-cascade interaction noise as in a realistic fan-stage is performed in this master thesis. The setup consists of an arrangement of linear cascade of OGVs, and a rod which mimics the rotor of a turbofan engine. Two experimental campaigns are undertaken. The first one consists of a wing (NACA 5406) and a rod mounted on flat plates. The wing mimics the mean aerodynamic loading of the central blade of the cascade. This experiment is performed to study the individual characteristics of the OGV blades, when placed in a cascade. The second setup is that of the Rod Linear Cascade model. Far-field directivity of noise sources are analysed using microphones placed on directivity arcs. Ability to quantify the upstream propagation of noise from the cascades is realized using a beamforming array, which is recessed on the test section wall and facing the pressure side of the OGVs. The flow-field at different locations in the test section is analysed using Hot-Wire Anemometry. The Hot-Wire measurements are also used to supplement the acoustic results.

The test section is observed to successfully emulate the vortex-cascade interaction noise and this noise is observed to scale with the sixth power of flow speed. The beamforming array is found to help in improving the SNR of acoustic measurements in the test section and hence allows the quantification of the upstream propagation of vortex-cascade interaction noise.

Contents

List of Abbreviations

BGN	Background Noise
BPF	Blade Passage Frequency
CAA	Civil Aviation Authority
CFDBF	Conventional Frequency Domain Beamforming
CSM	Cross Spectral Matrix
EASA	European Aviation Safety Agency
EI	Stiffness
FAA	Federal Aviation Administration
FFT	Fast-Fourier Transform
He	Helmholtz Number
HWA	Hot-Wire Anemometry
LE	Leading Edge
MATLAB	Matrix Laboratory
NASA	National Aeronautics and Space Administration
OGV	Outlet Guide Vane
OSPL	Overall Sound Pressure Level
PSD	Power Spectral Density (in Pa^2/Hz)
PWL	Sound Power Level (in dB/Hz)
RLC	Rod-Linear Cascade
RPM	Revolutions Per Minute
RSA	Rod-Single Airfoil
SDT	Source Diagnostics Test
SNR	Signal to Noise Ratio
SPL	Sound Pressure Level (in dB)
TBL-TE	Turbulent Boundary Layer - Trailing Edge
TE	Trailing Edge

List of Symbols

Greek Symbols

α	Coefficient of thermal resistivity
α_{wing}	Angle of attack of the wing
Γ_1, Γ_2	Non-dimensional scalar functions
γ^2	Coherence
δ^*	Displacement thickness
θ_{scan}	Resolution of beamformer in °
λ	Wavelength
ξ_j	Source location at a grid point on the scan plane
ρ	Density
σ	Cascade solidity
σ_U	Standard deviation of a velocity time series
ϕ	Angle of microphone placement from center of the array
ω	Rotational frequency

Roman Symbols

c_0	Speed of sound
f	Frequency
f_q	Cut-off frequency
k	Wavenumber
$\boldsymbol{p}$	Fourier transform of pressure
$\boldsymbol{p}^*$	Complex conjugate of fourier transform of pressure
R	Resolution of beamformer
$\boldsymbol{w_j}$	Steering vector

1

Introduction

Our everyday life is accompanied by sound. From the ringing of the morning alarm to the sound of your snoring partner, sound is an integral part of our lives. Sound is produced when something vibrates. These vibrations are characterized as pressure fluctuations in the medium (water, air, etc.) which causes the medium around it to vibrate. Vibrations in air are in the form of traveling longitudinal waves, which we can hear. The human hearing threshold is a wide spectrum, ranging from 20 Hz to 20 kHz. Sound waves consist of areas of high and low pressure called compressions and rarefactions, respectively. The unwanted sound is usually characterized as noise. In the Aerospace sector, the study of sound generated aerodynamically is termed *Aeroacoustics*. Aerodynamic sound arises due to fluctuations of velocity in the flowfield. But these are not directly translated into acoustics. The coupling between aerodynamics and acoustics is very elusive and this makes the analysis of flow related sound, tricky and interesting.

To supply to the demands of the growing population, there has been a steady increase in air traffic over the years. This has an adverse effect on the population residing close-by airports, since the noise of the aeroplanes taking off and landing are the most perceivable to the human ear. The Federal Aviation Administration (FAA) regulates the maximum noise level that an individual civil aircraft can emit through requiring aircraft to meet certain noise certification standards. According to FAA, a maximum day-night average sound level of 65 dB is incompatible with residential communities. These regulations become stringent every year with increasing air traffic. An example of limits set for the approach and departure noise of aeroplanes is shown in figure 1.1. Quite recently, there has been a deviation in the trend, and the approach noise has not been conforming to the limits placed. The approach noise is usually dominated by the overall noise at the fan-inlet and exhaust, which in turn is attributed to noise generation mechanisms in the turbofan bypass duct.

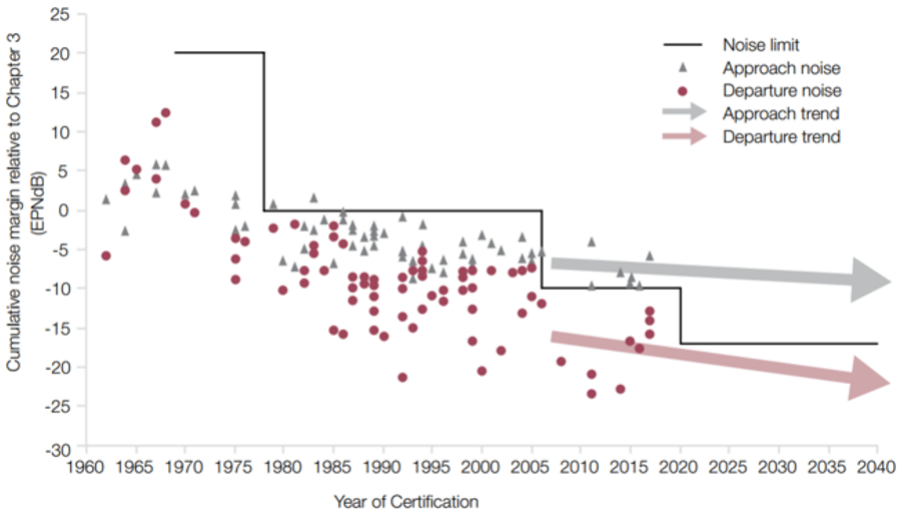

Figure 1.1: Aircraft noise emission limits over time *Source: EASA*

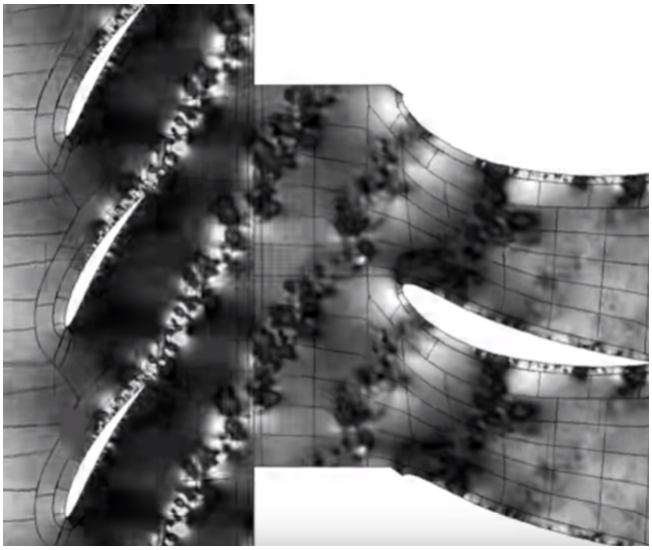

Figure 1.2: Visualization of fan wake impingement on a cascade [1]

1.1. The Turbofan noise problem and the proposed solution

With improvement in technology, turbofan engines have replaced the turbojets in commercial aircrafts due to its ability to generate the same thrust by minimal utilization of fuel compared to a jet engine [2]. Replacement with turbofan engines also ensured that overall efficiency of the engine was higher than that of a turbojet. As an added advantage, the increase in bypass ratio was also seen to reduce noise levels initially. The important noise sources from a turbofan engine include the fan blade (rotor) self noise and the fan wake impinging on cascade blades in the bypass duct (rotor-stator interaction noise (Figure1.2)).

With an increase in the bypass ratio, the distance between between the rotor and the stator decreases. The decrease in the distance enables the fan wake (vortices) to be more coherent on the stator blades. The vortices which interact with the leading edges of the OGVs are stretched, resulting in a highly unsteady pressure fluctuation on the surface of the OGV. These fluctuations are translated into acoustics, causing an increase in the tonal noise production. Many attempts have been successfully made in quantifying this noise source using a simple rod - airfoil model, which mimics the vortex airfoil impingement noise. This would be the simplest configuration to analyse the vortex - leading edge interaction. But in a turbofan stage, the OGVs are present in a cascade and all the blades which are excited by the fan wake have a phase relation. This leads to a noise generation, which is not only produced by the vortex interaction , but also modified due to the presence of the nearby blades. The blades diffract the sound waves, modifying it's shape and amplitude. In addition to the effect of nearby blades, the OGVs are encased in an annular duct and this modifies the sound waves (duct modes) propagating from the bypass.

A simple test setup, which can replicate the fan wake impingement on the cascade and thereby help in isolating the different noise sources which can arise, has not been looked into, atleast, quite clearly. A major advantage of such a setup is its ability to be useful in studying noise mitigation techniques. Thus, to isolate different noise sources and analyse the effect of the cascade in modifying the vortex-airfoil impingement noise, a linear-cascade model is utilized in this master thesis. This model is symbolic of the annular cascade (without considering the rotational component of flow). The periodicity in the tonal noise produced by the rotor is replicated by a rod, which is designed to shed vortices at the same period as that of fundamental blade passage frequency of a rotor. Thus, this configuration could prove vital in replicating the fan stage interaction noise and is represented in Figure 1.3.

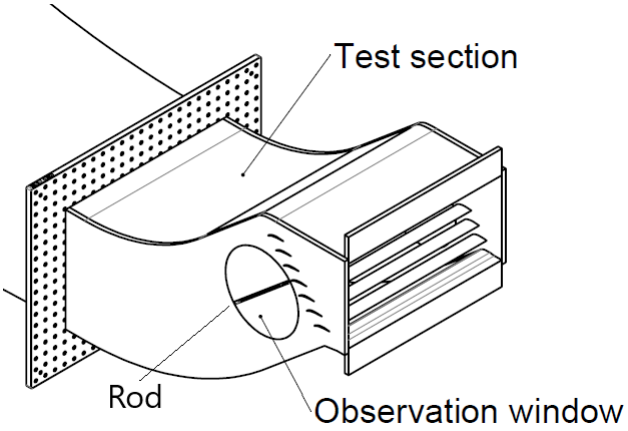

Figure 1.3: Rod-Linear Cascade (RLC) model, [3]

1.2. Research goals

The objectives of the current research include;

- Ability of the test setup to predict the vortex-cascade interaction noise as in a realistic fan-stage
- Ability of the beamforming array to account for reflections, improving the SNR and quantify the upstream noise-propagation
- Ability to capture the directivity of the noise downstream of the cascade and enabling the estimation of scaling laws

The questions to be addressed in achieving the research goals are detailed below:

1. Isolation of the central OGV blade on which the vortex street impinges is to be achieved by utilizing a simpler configuration consisting of a rod and an isolated airfoil (NACA 5406), which mimics the same aerodynamic loading (computationally observed [3]) as the central OGV blade when placed in the cascade. Does NACA 5406, experimentally too, have the same loading as the OGV blade? Can this be validated by utilizing a load cell which calculates the overall lift on the airfoil and compared to the lift produced by the central OGV blade? If yes, does this LE noise produced also dominate the TE noise which would be produced by the same blade?
2. Would tilting the rod such that a portion of the vortex street impinges on different spanwise locations of multiple blades be more representative of an actual fan-stage? If so, what would be the noise signature of a single blade (NACA 5406) and tilted rod configuration when compared to the default case for full span-wise wake impingement configuration?
3. Can the isolated LE noise effect arising from a single airfoil be compared to the noise arising from the RLC configuration ?
4. Can the upstream radiation of the cascade noise be quantified by having recessed microphones in the walls of the test section? Will this microphone array be able to account for the reflections from the walls of the test section?
5. Can scaling laws and directivity from the RSA as well as the RLC configuration be obtained from the measurements taken by the microphones on the directivity arcs?

1.3. Structure of the Thesis report

The research questions stated above will be tackled by experimental Aerodynamic and Acoustic measurement techniques.

Vortex - structure interaction noise forms the basis of any turbulent flow interacting with a surface or an airfoil and the literature will be addressed in Chapter 2. Cascade acoustics, microphones and duct acoustics will also be explained and the contributions from various researchers will be summarized in this chapter.

Chapter 3 involves explanation of the experimental setup, detailing the motivation for Aerodynamic and Aeroacoustic measurements and their locations, the flow conditions, the various geometries and the measurement quantities of interest. Finally, a discussion of some preliminary analyses undertaken to justify the utilization of measurement techniques are done.

Chapter 4 involves the results and discussion from the two experimental campaigns. Acoustic measurements are two-fold, one performed in the Rod-Single Airfoil (RSA) configuration and the other in the RLC configuration. In the isolated airfoil configuration, the acoustic measurements obtained from the directivity arc in far-field are utilised to discuss the different noise sources, particularly that of partial-spanwise wake impingement noise. The Aerodynamic measurements are performed only in the RLC configuration. Velocity spectra obtained using hot wire anemometry at different locations are discussed. The directivity of different noise sources from the circular array of microphones placed downstream are obtained as a part of the acoustics measurements. The acoustic spectra obtained from the microphones placed upstream are compared against the downstream circular array and discussed. Scaling laws are also obtained for various noise sources of interest and discussed.

The conclusions of this experimental results are summarized in Chapter 5. Answers to the research goals are outlined and recommendations for future research in the vortex-cascade interaction noise are stated.

2

Literature survey

2.1. Vortex-airfoil interaction noise

One of the most important noise sources in Aeroacoustics is a blade moving through a region of turbulence. The sound that radiates to the farfield from this interaction is termed the leading edge noise or the vortex-airfoil interaction noise or vortex-leading edge interaction noise. In an incompressible flow, information propagates at the speed of sound, so the TE (Trailing Edge) boundary condition is unaltered until the acoustic pulse generated at the LE (Leading Edge) reaches the TE. Since wave propagation is enhanced by the mean flow, time taken for this acoustic wave to travel to the TE is given as $\frac{c}{c_\infty + U_\infty}$. Phase shift between LE pressure fluctuations and TE ones can be then written as $\frac{\omega c}{c_\infty + U_\infty}$. For incompressible flow, c_∞ is infinite and phase shift is 0. But since a gust excites all frequencies, the incompressible flow theory is valid only if

$$\frac{kc}{1+M} << 1$$

Mach number also plays an important role and if M < 0.333, the incompressible flow theory is usually valid.

The physics behind the vortex-leading edge interaction mechanism is explained as follows.

An airfoil in a turbulent flow experiences a fluctuating lift which radiates sound to the far-field. This fluctuating lift is a result of unsteady pressure field produced by the airfoil in response to turbulence. The pressure fluctuations are generated by the interaction between the turbulence and the solid surface of the airfoil. The interaction of a vortex representing turbulence with the leading edge an airfoil is shown in figure 2.1.

A 2-D vortex is convected towards the airfoil. As the vortex gets closer to the airfoil, the unsteady lift reaches a maximum and at this point, the radiated pressure is maximum. The vortex then gets stretched around the leading edge and the unsteady lift decreases, causing a proportional decrease in the radiated pressure. The noise thus radiated to the far-field is termed as the vortex-leading edge interaction noise.

Acoustic radiation from a vortex-airfoil interaction was first analysed by R.K.Amiet. The relation between total fluctuating lift on an airfoil in an turbulent stream and far-field sound was formulated by considering the observer located directly overhead [4]. According to him, a typical turbulent eddy consists both of parallel and skewed gusts.

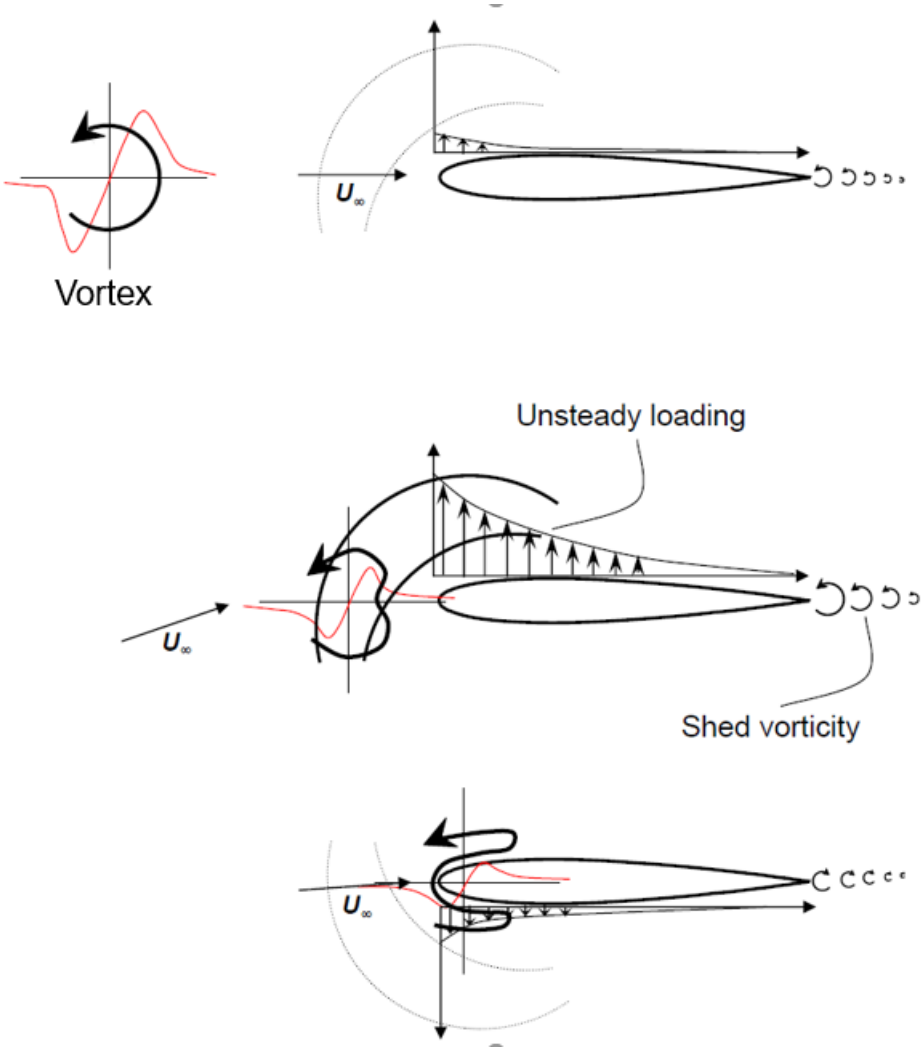

Figure 2.1: Vortex-leading edge noise production mechanism [5]

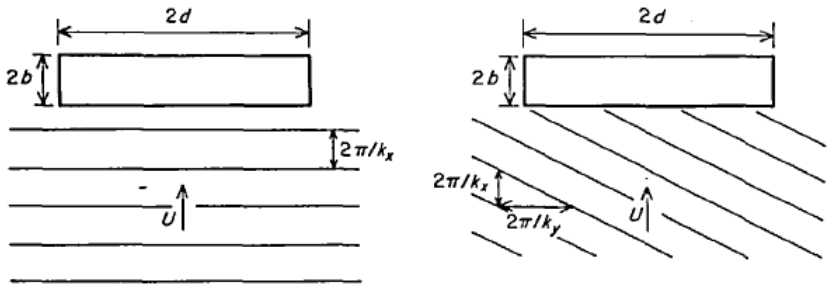

Figure 2.2: Parallel and skewed gust [4]

These gusts are taken to be incident on the leading edge of an airfoil. A parallel gust is an efficient sound producer and poses no problem to far field sound measurements. The skewed gust varies sinusoidally along the span of the airfoil, hence there is substantial cancellation of lift produced by adjacent spanwise stations. A flat plate airfoil with infinite span was considered for analysis and pressure jump across the flat plate was used to calculate the cross power spectral density (PSD). It was observed that the dominant noise source would be from a parallel gust.

In addition to his previous analyses, Amiet also contributed to the prediction of unsteady blade loading and the effects of varying relevant parameters, including the observer position, the core diameter of the vortex

and vortex orientation on the far field noise.

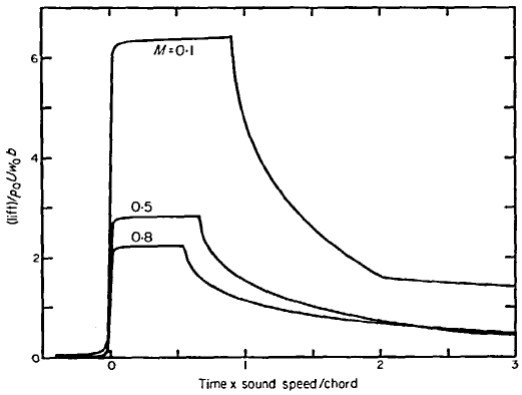

Figure 2.3: Airfoil response to delta function gust, unit span [6]

For a delta function gust, lift is independent of time until the generated acoustic wave reaches the TE. The point at which the decay begins is readily seen to be the acoustic propagation time from LE to TE (Figure 2.3). Sound propagates in moving fluid, relative to airfoil, and has a speed c_0(1+M). The second break point is due to the wave reflected from the TE reaching the LE. The propagation speed for disturbances moving upstream is c_0(1-M). The flat portion shows that sound has not yet reached the TE. For different observer positions, the phasing of sources on the airfoil will be different because of differences in propagation times. With the observer directly overhead, phase shift can be neglected. It was also observed that the shape of far-field pressure-time curve was found to be independent of vortex orientation, differing only in amplitude. Greater the angle of the vortex with respect to span, greater was the measured amplitude.

Perhaps the most important result from his analysis was the effect of vortex orientation. The shape of far-field pressure-time curve was found to be independent of vortex orientation, differing only in amplitude. Greater the angle of the vortex with respect to span, greater was the measured amplitude, as shown in Figure 2.4

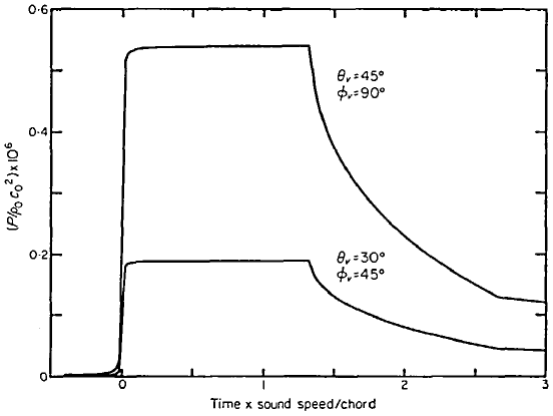

Figure 2.4: Effect of vortex orientation [6]

According to Curle [7], acoustic response of an airfoil can be determined by distributing dipoles over the airfoil surface, equal in strength to the aerodynamic force acting on the surface. Linearized airfoil theory, infinite span airfoil theory were utilized for the formulation and the geometrical parameters of the airfoil like camber and thickness were not accounted for. An important result from the linearized theory was that, only the gust component normal to the airfoil surface produces a lift response, and if the airfoil were to intersect the vortex normal to the line of vortex, no lift would be produced.

Howe [8] analysed the acoustic signature of a vortex-airfoil interaction comprising of two components, asssociated with axial and azimuthal vorticity. He proposed a general formula for the acoustic pressure when the airfoil is rigid and acoustically compact, by including the effect of thickness, camber and twist of the

airfoil. *For a flat airfoil of uniform chord and large span, the sound produced by vorticity shed from the TE in order to satisfy the Kutta condition interferes destructively with the 'direct' sound generated by the impinging vorticity when near field energy of the latter is diffracted at the TE. When the shed vorticity is assumed to convect at the same mean stream velocity as the impinging vorticity, the destructive interference is total, and no sound emanates from the trailing-edge region. When the shed vorticity convects at a smaller, near-wake velocity, however, the TE radiation is small and finite, but still dominated by radiation from the LE.* An airfoil with constant chord, with large aspect ratio was assumed in his analysis. A comparison of TE noise with incident fluctuation noise is represented in Figure 2.5.

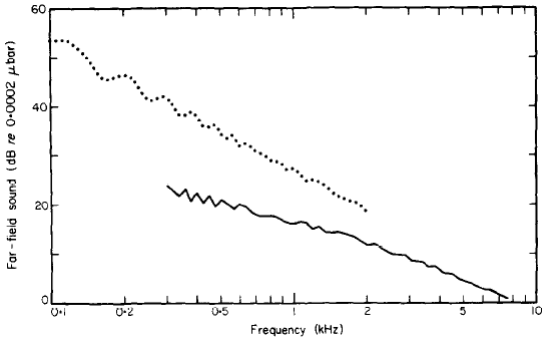

Figure 2.5: Trailing edge noise compared with incident turbulence noise; - TE noise; ... LE noise[9]

The effect of airfoil parameters such as thickness, camber, angle of attack and LE nose radius on the turbulence - airfoil interaction noise were studied experimentally by many.

Paterson and Amiet [10] investigated the far-field noise and unsteady surface pressure on a NACA 0012 airfoil operating in a homogeneous, isotropic turbulence field. They observed that the noise associated with the interaction of the turbulence with the airfoil was an order of magnitude higher than other noise sources such as those associated with the turbulent boundary layer and the stalled flow. The largest peak in the unsteady pressure was found to be located close to the leading edge, with the leading edge being the dominant source of noise propagating to the far-field. The radiated noise was found to increase by 2dB as the angle of attack was increased, which was contradictory to what was observed by researchers before. Accuracy of prediction of the far-field noise from inflow turbulence properties was greater than from the unsteady surface pressure.

Oerlemans and Migliore studied the effect of grid generated turbulence and concluded that inflow turbulence noise increases for increasing sharpness of model LE. Also, there was an increase in the radiated noise upto 5 dB as the angle of attack was increased from 0 to 8 ° in the frequency range of 1-2 kHz. Moreau [11] experimentally studied the turbulence-airfoil interaction noise on flat plate and airfoils of different thicknesses. The upstream turbulence was produced by a turbulence grid. The test was for three different velocities and four different angles of attack. From the experiment, angle of attack was found not to play a role in the far field noise, however, an increasing airfoil thickness was found to reduce the turbulence interaction noise significantly, particularly at high frequencies.

Quite recently, Chaitanya et al.[12] experimentally studied the geometrical effects of airfoils (Figure 2.6) on turbulence interaction noise to solve the mystery of the conflicting findings regarding the effect of angle of attack, leading edge radius and thickness. In addition to this, effect of camber was also studied. Aircraft self noise was found to dominate overall noise radiation at high frequencies. The upper frequency at which self noise dominates was found to reduce with increasing airfoil thickness. Angle of attack and camber have been shown to only weakly affect interaction noise suggesting that mean loading does not affect the unsteady loading that consists of aerodynamic noise sources. It was concluded that the geometrical effects cannot be addressed by a single length scale and that, the global geometry of the airfoil has to be taken into account when considering the effects due to mean flow.

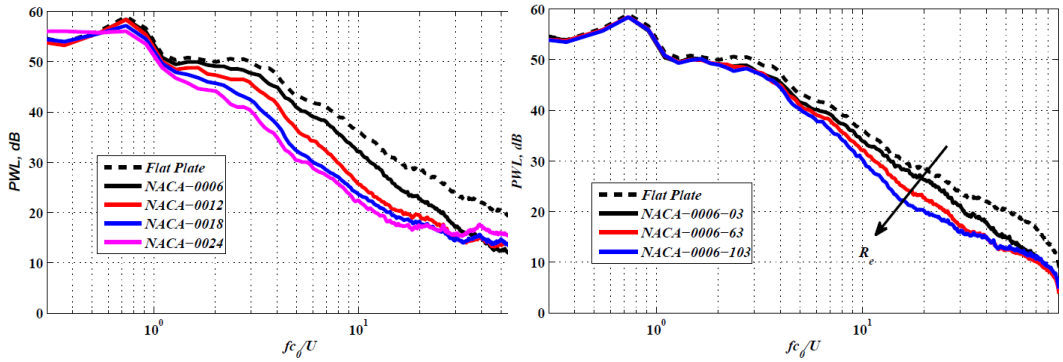

(a) Effect of airfoil thickness on noise radiation (b) Effect of nose radius on noise radiation

Figure 2.6: Geometrical effects of airfoils on radiated noise [12]

The concept of incident turbulence interaction took a different turn when the interaction noise of vortex-airfoil configuration was quantified using a rod-airfoil configuration which proved vital in studying the noise emanating from turbofan bypass ducts. Casalino et al. successfully studied the rod-airfoil configuration [13] as a potential benchmark for broadband noise modelling in turbulence interaction noise. A cylindrical rod in a flow sheds vortices in the form of Von-karman vortex street. This vortex street is fully turbulent when Reynold's number (Re) is in the range 300 - 3×10^5. Vortical structures were identified with dimensionless scalar functions $\Gamma_1(x)$ and $\Gamma_2(x)$. These functions are based on normal angular momentum and is derived from the measured velocity field and the analysis of far field noise spectra was done (shown in Figure 2.7). It was inferred from the experiment that the vortex shedding is not merely responsible for a tonal sound radiation, but also accompanied by a spectral broadening. Another important observation from figure 2.7 is that the sound levels are higher in the presence of the airfoil, thus the overall sound level is dominated by the vortex-airfoil interaction.

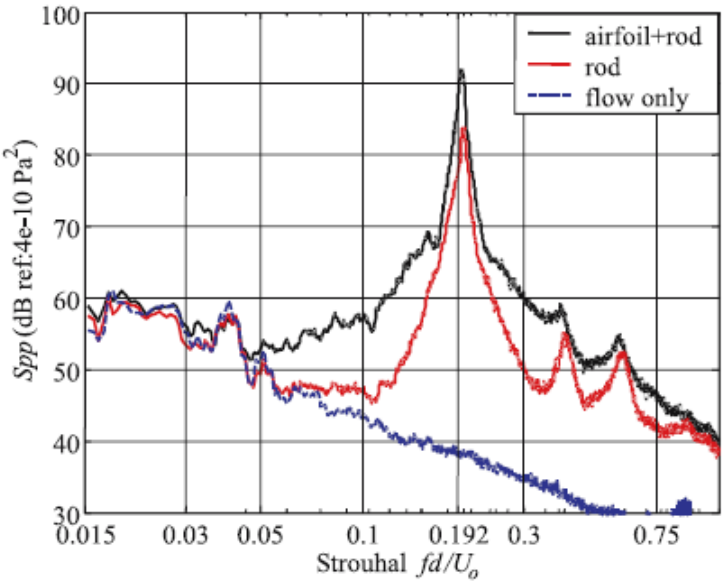

Figure 2.7: PSD - far field spectra [13]

In another follow-up experiment, the effect of rod diameter, rod-airfoil streamwise gap was experimentally studied by Yong Li et al. [14]. The noise source maps indicated that both the location and level of dominant noise vary with changing rod diameter. It was also observed that the radiated noise from the test model is generated mainly by the upstream rod due to the unsteady loads induced by the vortex shedding. The conclusion being, the intensity of vortex–structure interaction at the airfoil leading edge is reduced as the rod diameter is decreased. It was observed that, both vortex shedding Strouhal number and corresponding peak SPL vary with change of the gap. The noise levels increases as the streamwise gap between the rod and the

airfoil is reduced. But after a particular clearance, the noise levels drop, suggesting that, due to the vicinity of the airfoil, the feedback mechanism is strong thereby preventing the formation of Von-Karman vortices.

2.2. Cascade acoustics

It is of paramount importance to understand the Turbulent Boundary Layer- Trailing Edge (TBL-TE) noise, before proceeding with the effect of cascade blades. Turbulent boundary layers are characterized by unsteady fluid motions and pressure fluctuations, caused by turbulent structures with varying sizes. The pressure fluctuations close to the wall are convected downstream and the sudden jump in boundary conditions at the TE leads to scattering of this pressure fluctuations to the far-field, and the sound thus produced is termed TBL-TE noise. As a result of the varying sizes of turbulent structures, the scattered TBL-TE noise spectrum is broadband. This is depicted in figure 2.8

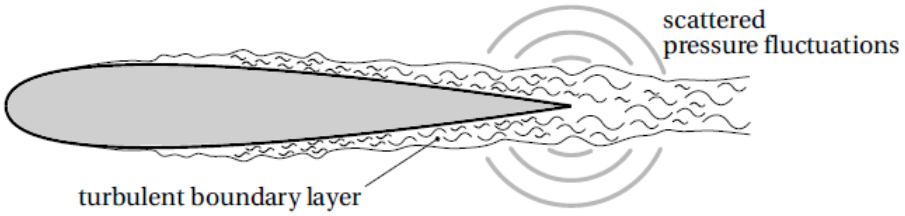

Figure 2.8: TBL-TE noise [15]

The presence of a blade row in a compressor stage is crucial in determining the propagation of acoustic radiation. Cascade effects on acoustics have been studied extensively since the beginning of the acoustics era. An interesting aspect of the effect of cascades is not just reflection, refraction and transmission of sound waves, but also includes the propagation of the acoustic waves in the ducts formed by the cascades which are termed as duct modes.

In 1966, R.Parker performed experiments to study the resonance effects in wake shedding from parallel plates [16]. When resonance occurs, vortices are considered to be shed at a natural frequency of vibration, which is at the natural frequency of shedding from a rigid plate. For his test, plates with different thicknessess were used. It was observed that the natural frequency for any mode of vibration is proportional to the thickness of the plates while the natural wake shedding frequency at a given velocity is inversely proportional to thickness. Bruel and Kjael half-inch microphones were placed upstream of the plates to detect resonances. For single plates, the pressure fluctuations could only be detected in and near the plate wakes, with the maximum pressure amplitude being a function of the dynamic head. There was progressive increase in frequency with no detectable resonance. The important conclusions from this experiment were;

- Resonances associated with wake shedding from parallel plates in a fluid stream were unrelated to mechanical vibration and were caused by acoustic effects
- The natural wake frequency which corresponds to a wavelength considerably greater than twice the distance between the plates and the overall dimensions of the fluid passage control the frequency, rather than the plate spacing.

The first major acoustic modelling of cascade effect was done by Kaji and Okazaki who worked on propagation of sound waves through a blade row. They studied the sound propagation using a semi-actuator disk theory and by considering a 2-D flat plate cascade model with finite chord length and infinitesimal blade spacing. Effect of blade camber and thickness were not considered, since they are, in most cases, compressors, sufficiently small in dimension compared with wavelengths of generated sound waves. Three kinds of incident waves considered: a pressure wave from the upstream side, pressure wave from the downstream side and a vorticity wave from the upstream side of the cascade. Formulation of the problem is depicted in Figure 2.9. Linearized theory was adopted and the effect of mach number, angle of incidence upon reflection and transmission of sound waves, the effect of wave number and stagger angle of the blades were studied. Based on the study, the following conclusions were made:

- Sound wave transmission coefficient decreases with an increase in mach number

- There exists an angle of incidence, apart from the chordwise direction, at which the sound wave has no reflection
- The phase difference between cascade inlet and exit influences the transmissions and reflection of the incident wave
- The steady aerodynamic blade loading has no substantial effect on sound transmission and reflection

In another publication, Kaji and Okazaki also theoretically studied the effect of finite spacing of blades on the sound propagation through it [17]. When the product of wave number with blade spacing became large (high frequency regime), a number of waves with wavelength in the cascade direction different from that of the incident wave begin to propagate far upstream and downstream. In the low frequency regime, the wavelength of the transmitted/reflected wave in the cascade direction is the same as that of the incident wave.

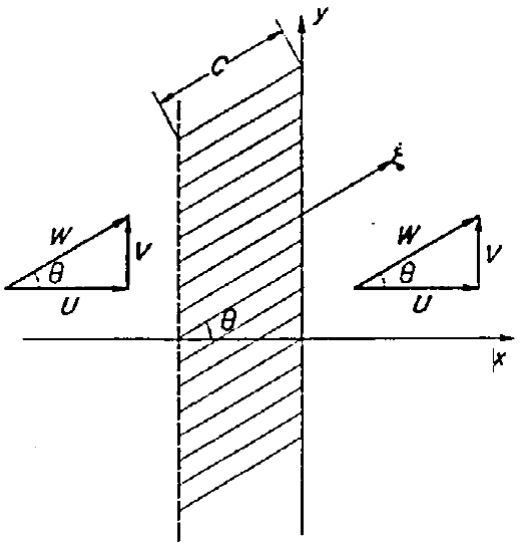

Figure 2.9: Flow field and semi actuator disk[18]

Amiet [19] worked on the 2-D problem of a plane sound wave impinging on a flat plate airfoil cascade in the low frequency regime (wavelength longer than blade spacing and chord). Infinite span was assumed. Successful comparisons with Kaji's [18] theory were made. In another attempt, Amiet [20] studied the effect of sound propagating upstream through the blade rows. This situation is similar to rotor-stator interaction. The vorticity shed by the rotor blades were accounted for. Again, low frequency assumption was made. Distance between the blade rows was large compared to spacing between two blade rows. It was observed that the sound reflected and vorticity shed from the upstream row due to interaction with a sound wave will impinge on the downstream blade row affecting the transmission properties of the downstream row. Viscous wake of upstream blade row was neglected since their interaction with downstream blade row produced only sound of Blade Passage Frequency (BPF) and its harmonics. A schematic of the setup considered by Amiet is shown in Figure 2.10. The individual blades were compact sound sources, hence in the far field, were considered as point dipoles.

An important observation from the current analysis was the absence of resonance, meaning there is no significant amount of mean flow energy being converted to acoustics. Sound wave interacting with a pair of blade rows does not appear to be a source of additional acoustic energy, even though the unsteady vorticity shed from the upstream row is allowed to interact with the downstream row.

M.S.Howe also studied the blade-vortex interaction in a 2-D cascade flow. The interaction of tip vortices from a fan impinging on a cascade was modelled using helical vortices. It was assumed that the dominant acoustic wavelengths were, on the one hand, large relative to the cascade blade-pitch but, on the other, small compared to the relevant dimensions of the duct containing the mean flow (so that the strength of the radiation may be estimated by assuming an infinite acoustic medium).

Although the latter approximation is generally applicable in practice only at very high frequencies, it was convenient because it allowed the influences on sound production of purely acoustic and hydrodynamic mechanisms to be distinguished. A simple manner of influence of cascade solidity and non-compactness of blade passages on the sound produced were formulated. In the particular cases of discrete rectilinear or helical vortices impinging on the cascade from upstream (and having core diameters that are small relative to the cascade pitch and blade chords), it was shown that the strength of the acoustic pulse generated when the vortex is severed by the leading edge of a blade decreases rapidly with increasing cascade solidity.

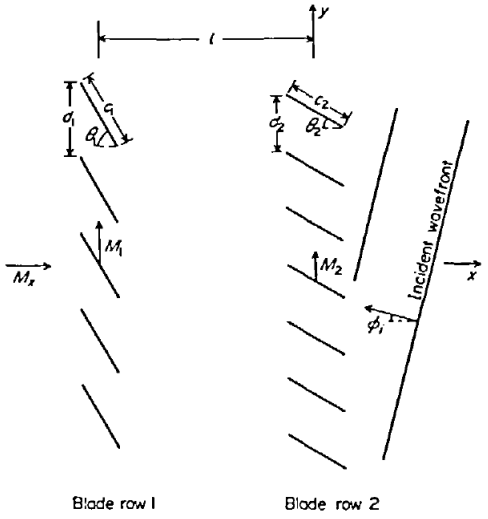

Figure 2.10: Blade row geometry [19]

Airfoil self noise from fans and rotors was found to be generated by blade boundary layer turbulence interacting with the trailing edges of the blades. Stewart A.L.Glegg [21] studied the airfoil self noise generated in a cascade and compared the magnitude of the noise mechanism with the field that would be generated by a single airfoil without adjacent blade scattering. The main difference here was, the isolated blade radiates waves that propagate spherically into acoustic far field, whereas the cascade generates acoustic modes that are bounded and propagate with minimal attenuation. The leading edge interaction mechanism was important, since in a cascade, waves traveling upstream were trapped in the blade passages and propagated to the leading edge without attenuation. At the LE, the trapped waves were reflected and propagate in the downstream direction, interacting with the trailing edge again and radiating away into the region downstream of the cascade. He concluded that the Mach number has a relatively weak effect on acoustics, and scaling with flow speed will be unaltered by the effect of adjacent blades. The dominant mechanism for additional scattering was due to the presence of the nearest blade acting as a hard reflecting plane and causes increase in levels as well as interference dips or nulls in the spectra.

The upstream acoustic radiation from a flat plate cascade interacting with an gust was analysed by Peake and Kerschen [22]. They studied the influence of mean loading on the upstream radiation by considering harmonic components of the incident field with reduced frequency, k. Based on his analysis, in a high frequency limit, the forward radiation consists of 4 types of sound generated as discussed below;

- Sound is generated by the interaction between the gust and each blade leading edge, and propagates directly to the observer without interacting with any other blades (this is exactly equivalent to the radiation produced by the interaction between the gust and an isolated leading edge, and is referred to as the direct field)
- The direct field from a given LE will travel along the front face of the cascade according to a complicated Fresnel-diffraction process, and will interact with all the other leading edges to produce more radiation, some of which will then travel directly to the observer
- From a given LE, the direct field in the negative direction will be reflected by the lower blade and then re-scattered by the leading edge from which it originated. Some of this re-scattered field will then reach

the observer directly and some will be re-reflected by the lower blade back to the leading edge, and the process will continue indefinite

- For a staggered cascade the total field emitted from a given leading edge is reflected by the adjacent lower blade, before reaching the observer

The above-mentioned mechanism of sound propagation is represented in Figure 2.11.

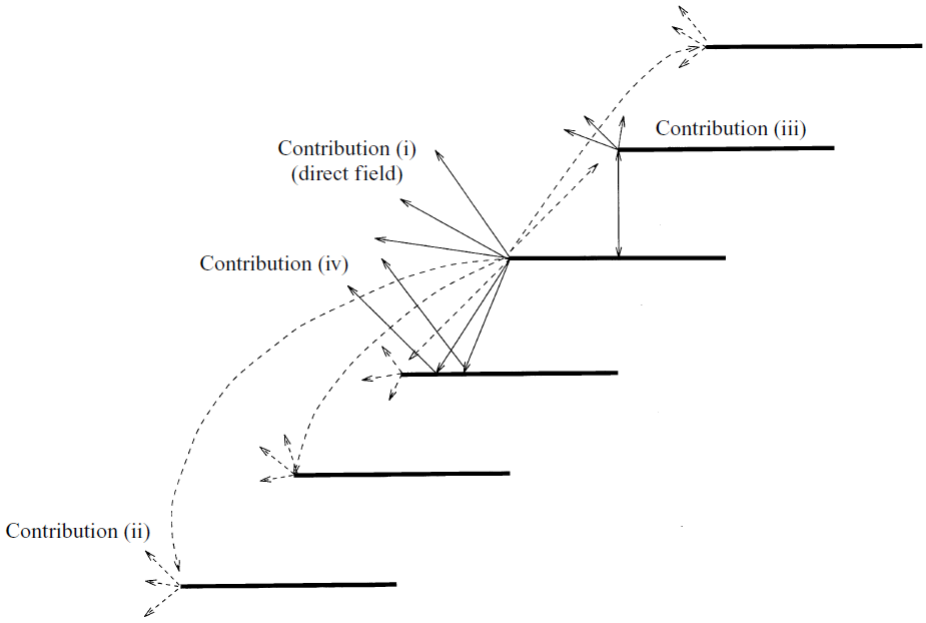

Figure 2.11: The principal radiation components reaching an upstream observer for kw ≫ 1 ; kw is the acoustic reduced frequency [22]

In another attempt, Evers and Peake [23] included the effects of small, but non zero camber and thickness in modeling the upstream radiation from a cascade. Reinforcing previous findings by many researchers, it is important to establish that, at high frequency, the noise generation may effectively be described by acoustic point sources at the leading edge, and that any other sources, specifically those at the trailing edge, along the airfoil surface and along the wake, are asymptotically smaller. It was observed that, increasing the thickness keeping the angle of attack same, increased the spectrum level, particularly at high frequencies, by 2-3 dB. However, these effects average when the gust responses are integrated over the full incident turbulence spectrum.

Experimental determination of cascade noise was kick-started mainly by Sabah et al. [24]. Blade loading was thought of as an important parameter (previous analyses were based on lightly loaded blades with negligible angles of attack). A linear cascade was considered in his analysis, as shown in Figure 2.12. The only draw back of the experiment could be that, in absence of sidewalls, flow might not be spatially periodic and sources, not correctly simulated. But if rigid side walls were added in order to ensure spatial periodicity, acoustic resonances would occur and radiated noise would not be measured properly outside. The acoustic pressure in the far field was measured in the range of 0-20 kHz. When the upstream velocity field was increased, there was an overall increase in the spectrum level. But this difference decreases in the high frequency range, hence it is dominated by self-noise. From further experiments, it was observed that;

- Cascade self noise scaled to $U^{5.8}$ and turbulence interaction noise intensity scaled with $U^{5.3}$ less rapidly. Hence, self -noise could play a dominant role at higher speeds encountered in turbofan engines. Self noise was found to be a decreasing function of angle of attack, as long as flow remains attached to the blades

- Another interesting observation was that, the measured directivity pattern had two lobes; one, in the direction of blade alignment, radiating from cascade suction side and another one with smaller intensity radiating from the pressure side. these results suggest that sound is preferentially radiated in aft directions

An experiment involving a stationary annular model of cascade vanes with an upstream turbulence grid was pursued by Poson and Roger [25] to validate the cascade response function for fan broadband noise predictions. Two sets of cascade measurements were taken, one with higher solidity, and another with lower solidity with different vane numbers, but the same vane design. Presence of upstream turbulence was found to increase the noise levels in the cascade with higher solidity.

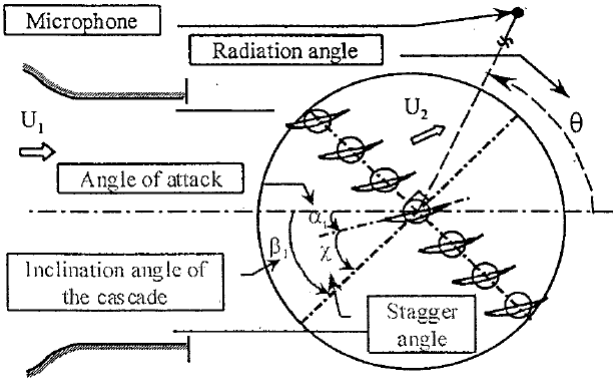

Figure 2.12: Experimental setup of Sabah [24]

Finez et al.[26] tried validating the broadband noise models from the trailing edge of the cascades using a simple, linear cascade model involving cambered airfoils. Amiet's isolated TE noise model was used to compare the cascade effect with experimental results. The measured far-field noise, as well as Howe's cascade model and Glegg's cascade model were compared to the Amiet's model for quantification of the cascade effect. The duct influence was separated from the cascade acoustics by having a closed wall upstream of cascade, and an open windtunnel downstream of the cascade. To measure the upstream sound measurements, kevlar walls were used for both the test section walls. Kevlar walls must be tested in-situ. Upon measurement, kevlar walls led to a noise increase of almost 10 dB upto 5kHz. It was found by hot-wire measurements that the boundary layer thickness increased by 50mm a few cm upstream of the leading edges. This led to discarding of Kevlar side walls from further analyses. From the far-field sound spectra obtained for different velocities, the PSD was found to increase with velocity, but the curves had similar shapes with peaks occurring at the same frequency. This was an important observation that the peaks were not Strouhal dependent. The data was hence scaled with Helmoltz number, meaning, the acoustic phenomena such as cascade resonances are governing the sound spectrum, rather than the flow itself. This is depicted in figures 2.13a and 2.13b which also represents the coalescing of acoustic far field PSDs upon scaling with U^6 law. From the directivity measurements, a comparison between the suction and the pressure side was made and was observed that the acoustic radiation from the cascade is mainly directed towards the suction side (which also benchmarks Sabah's findings).

The above experiment was compared with Amiet's isolated trailing edge noise model [9] (Figure 2.14a), The model assumed flat plate blades arranged in a cascade , with each blade at a different downstream location and the isolated TE noise model was applied to each blade with shear layer corrections. The following observations were made:

- The cascade effect was found to be negligible if the acoustic wavelength was smaller than the blade pitch, hence there was a good correlation between the measurements and the isolated TE theory in the high frequency region

- In the lower frequency region, a large discrepancy was found where the acoustic wavelength is greater than the blade pitch; the cascade effects play an important role and the model does not account for mechanisms governing the cascade effects

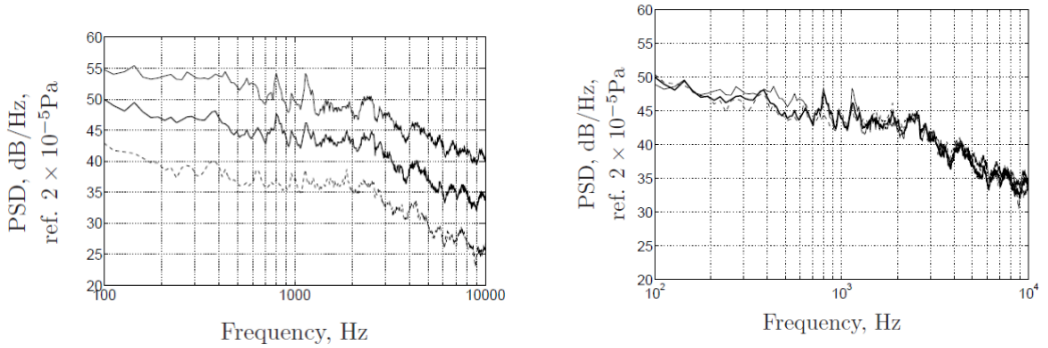

(a) Far field sound pressure levels , non treated [26]

(b) Far field sound pressure levels ,Helmoltz scaled and U^6 law scaling [26]

Figure 2.13: Far-field SPL [26]

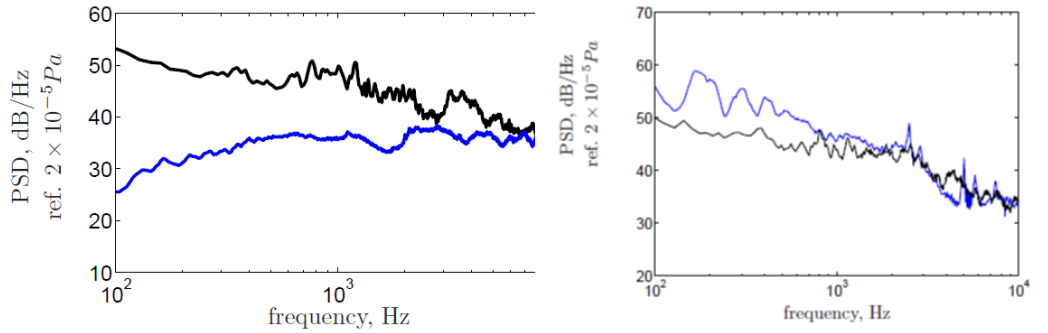

(a) Experiments vs isolated TE model

(b) Experiments vs cascade model

Figure 2.14: Experiments vs model [26]

The experiment was also compared with Glegg's cascade TE noise model [21] (Figure 2.14b) and the important observations summarized as follows:

- The cascade broadband noise is well predicted in the mid to high frequency range
- The discrepancies at low frequencies are attributed to the assumptions of the model, including the presence of finite number of scattering blades (whereas in the model it's infinite)

On a whole, the cascade effects cannot be neglected unless the wavelength is smaller than the pitch. From the experiments, it is observed that the presence of a cascade amplifies the acoustic effects in the region where the wavelength is larger than or comparable to the cascade pitch (also upon comparison with analytical models).

2.3. Duct acoustics

The ducts are important because they could cause an amplification of the sound power with resonance. In a duct, the sound power is assumed to be conserved and this assumption allows us to relate the duct sound levels directly to the far field, assuming there is no absorption at the duct walls and no sound power is reflected back toward the source by the duct exits or internal features (which is valid for duct diameters larger than the acoustic wavelength). For turbofan engines, the duct diameters are so large that the waves propagate freely out of the inlet or exhaust. This characteristic is very important for engine design since the sound power measured provides an effective noise source level, which corresponds to expected level of far-field sound.

Duct transmission was analysed by Tyler and Sofrin [27] in their overall study about axial compressor noise. They found that the sources produce rotating pressure patterns called spinning modes. When the tip speed of the generated pressure pattern is sufficiently high, the pressure fluctuations propagate in the

duct as a wave of undiminished intensity. a simple formulation for understanding the duct modes was the consideration of a thin, infinite rectangular duct (2D) and a reference plane where the pressure is taken to be oscillatory in the y direction, as depicted in figure 2.15.

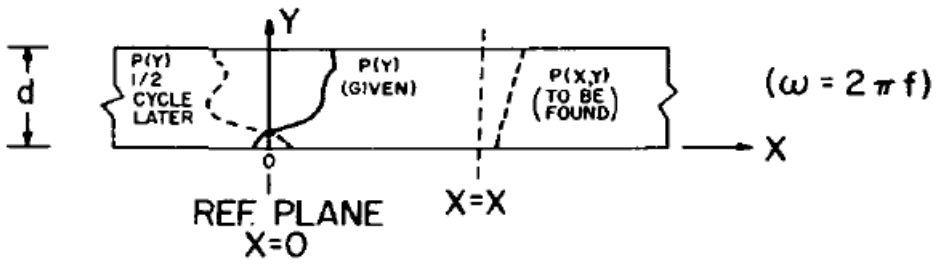

Figure 2.15: Defining a rectangular duct [27]

The solution to this is obtained in a stepwise manner where initially, the pressure distribution at x = 0 is resolved into a properly weighted sum of simple modes (modes refer to the simplest ways in which pressure can be distributed according to mathematical expressions). Then, the manner in which these modes are modified in amplitude and phase by travel in the duct is analysed. Finally, the modified modes are reassembled with the original weighting to give the resultant field. Apart from a plane wave, modes have form of cosine waves with an integral number of half cycles written as

$$p_q(y) = a_q \cos\left(\frac{q\pi}{d} y\right) \qquad ; q = 0, 2, 4, ...n$$

where $p_0(y) = a_q$ is a plane wave. The cosine here means that the tangent to each curve at the top and bottom of wall is perpendicular to the wall surface.Hence, the normal pressure gradient at the wall is zero, a necessary boundary condition (physically, no inflow of air through the walls), hence the sine component cannot be used here. The variation of pressure in the x direction is studied by considering a single representative mode and can be twofold, above or below the cutoff frequency. The wavelength in the y direction for each mode is λ_y = 2d/q. Considering no walls, these waves would propagate in y direction with a frequency $f_q = c/\lambda_y$. This frequency is the cutoff for the q^{th} mode. The change in transmission properties as the driving frequency is gradually swept through cutoff becomes more credible when it is pointed out that the following parameter f and f_q are given in the analysis as:

$$k_x = \frac{2\pi}{c}\sqrt{f^2 - f_q^2}$$

The complete pressure field can then be given as

$$p(x, y, t) = a_q \cos\left(\frac{q\pi}{d} y\right) e^{-k_x x} \cos\omega t \qquad (\text{decay}, f < f_q)$$

$$p(x, y, t) = a_q \cos\left(\frac{q\pi}{d} y\right) \cos(k_x x - \omega t) \qquad (\text{propagation}, f > f_q)$$

the following conclusions were drawn based on the above analysis:

- The y-distribution is a cosine wave of same shape as input with a plus or minus maximum at walls
- Variation of pressure with x takes different forms based on cutoff frequency for y distribution mode
- For $f < f_q$, intensity of pressure fluctuation falls exponentially. At all points located at a fixed distance from bounding walls, pressure fluctuations are exactly in phase
- For $f > f_q$, wave motion propagates in the duct and plane waves always propagate (cut off frequency is 0)

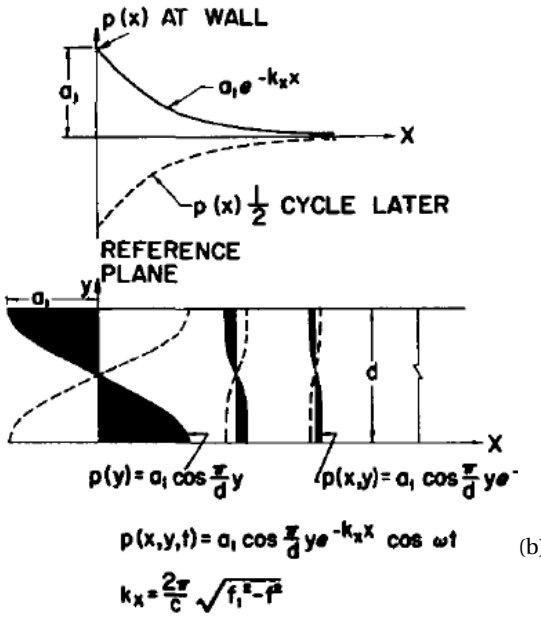

(a) Decaying field f < f_q

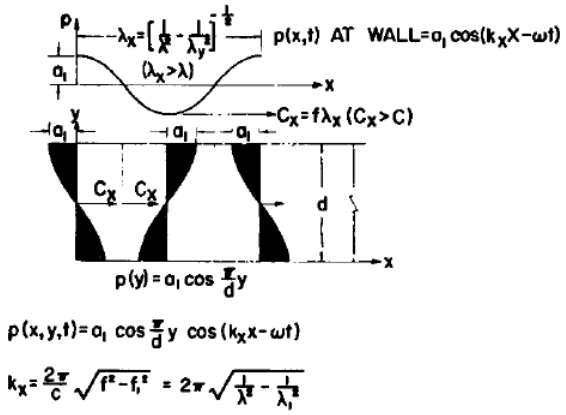

(b) Propagating field f > f_q

Figure 2.16: Duct mode [27]

The radiation of sound propagation from a thin rectangular duct was also analysed by Tyler. When frequency is increased, the peak of the radiation field tends to move toward the center line of the duct and vanishes at the center line. Hence, radiation from a rectangular duct possesses strong angular directivity which depend explicitly on frequency and mode number. This is shown in figure 2.17.

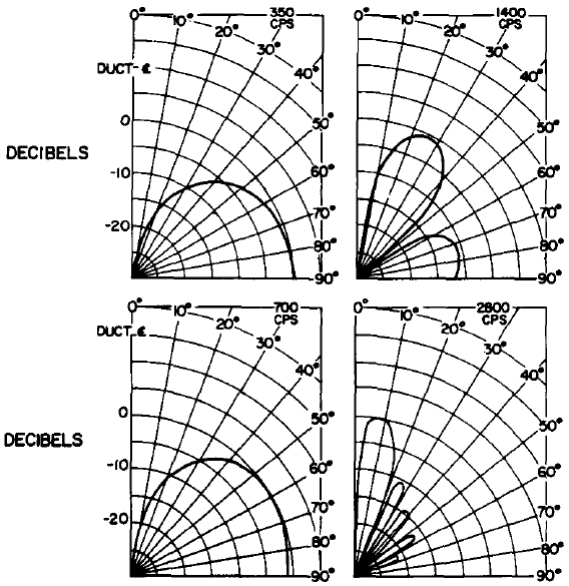

Figure 2.17: Directionality of radiation for thin rectangular duct for q=1 mode [27]

2.4. Microphones

The membrane of the microphone (depicted in Figure 2.18) vibrates in response to sound. These vibrations change the capacitance since the distance between the membrane and the backing plate fluctuates as a function of time. This is the working principle of a microphone. The sensitivity of microphones to the pressure fluctuations can be estimated using a pistonphone [28]. It produces pressure fluctuations of a known am-

plitude by using a mechanical motion of a vibrating piston at a fixed frequency to simulate a sound wave by compressing a fixed volume of air to which the microphone diameter is exposed.

Characteristics of microphones:

Selection of microphones is based on the frequency range and the type of experiment to be performed. This in turn gives a constraint on the selection of the size of the diaphragm diameter, which can be large or small. Large diameter microphones are more sensitive to acoustic fluctuations because these fluctuations are integrated over a bigger diaphragm area. They are useful is accurately measuring sound at low frequencies [28]. The smaller diaphragm microphones suffer from lower sensitivity, but have a greater range, both in frequency and in amplitude. The size of the diaphragm is also important compared to the wavelength of the sound.

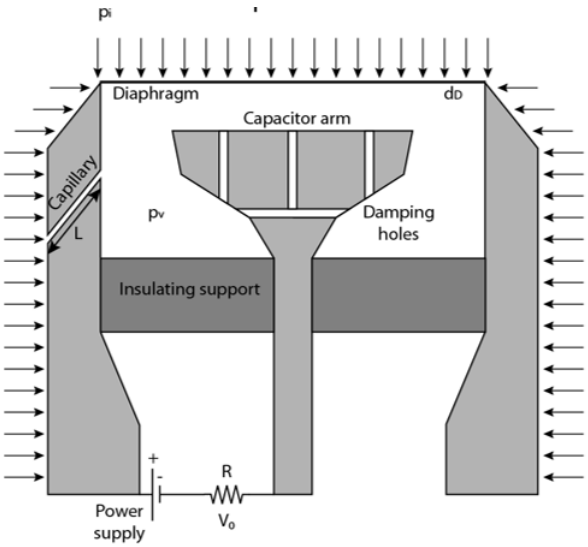

Figure 2.18: Schematic of a microphone [29]

When the wavelength becomes comparable to the diameter, the scattering of the sound field around the end of the microphone and the spatial distribution of the diaphragm sensitivity become important in determining the response. In far field measurements, it is important that the microphones are placed farther away from the flow so that there is no contamination of sound by the near-field pressure fluctuations associated to the turbulent free shear. It is also favourable to orient the microphone to point as directly as possible at the source. This aligns the wavefronts parallel to the diaphragm, thereby extracting the most favorable response. Perhaps the most important consideration in terms of obtaining accurate data is to have a high Signal to Noise Ratio (SNR). To achieve high SNR, microphones should be placed as close as possible to the source. Summarizing, the selection of microphones based on diaphragm size is dependent on a particular experiment. Also, microphones should be placed as close as possible to the source to increase SNR but also away from the flowfield disturbances (in the far field), so that spurious noise sources are not detected as much as they would be if these constraints are not taken into account.

Microphone arrays:

Microphones can also be used in isolating the sound sources by a source map or for obtaining the directionality of the source. To obtain the latter, a 1-D line array of microphones is enough, but to obtain the source map, beamforming is required. Beamforming or spatial filtering is a signal processing technique used in microphone (sensors in general) arrays for directional signal transmission or reception [30][31][32]. For beamforming, a 2-D array of microphones is required. In general, such microphones in an array can be referred to as phased arrays. This section deals with concepts which include the spacing of microphones (spatial resolution), aliasing and a general approach to array processing. In general ,the array output depends on the angle subtended by the source to the array. At lower frequencies, the sensitivity of the array output to the source is relatively weak and the directivity map displaces a single lobe. At higher frequencies, the main

lobe of the array sensitivity is much narrower (Figure 2.19), but with additional lobes. These additional lobes are false sources (spatial aliases) and are reduced by having a transducer spacing of less than half an acoustic wavelength. To obtain a good resolution at low frequencies, the length of the array needs to be as large as possible.

If there are multiple sources, there is another problem of *sidelobe leakage*, which occur as small peaks on either side of the sources. The sidelobes can then be reduced by multiplying each array signal by a weighting factor. This reduces the sidelobe leakage, but also the amplitude of the main source, which is a trade-off. The resolution limit of a microphone array is, perhaps, the most important and can be defined as the minimum angle at which two sources can be separated into individual images. This resolution is also termed as Rayleigh's [33] [34] limit and is given by ;

$$R = 2\text{htan}\left(\frac{\theta_{\text{scan}}}{2}\right)$$

where,

$$\theta_{\text{scan}} = 1.2196\frac{\lambda}{D}$$

h is the distance between the array plane and the source plane, D is the diameter of the array. If the resolution (R) is known, we can obtain the lower limit of frequency from which the sources can be clearly isolated or vice-versa and beamforming to isolate the sources can be made possible.

Figure 2.19: Main lobe at low frequency (and lower resolution)(left) and additional side lobes at high frequency (and better resolution)(right) [28]

The two main parameters which determine the acoustic array's beamforming performance is the main lobe width and the maximum side lobe level [28] [35].

- **Main lobe width**: Represents the magnitude and location of the true sound source in the scan plane and is defined as the maximum distance between two points representing the main lobe contour at -3 dB from the main lobe's peak
- **Maximum side lobe level:** In the absence of sound source, the source map shows a false source, formed due to constructive interference as side lobes. Can be calculated by measuring the relative magnitudes of the main lobe to the maximum side lobe level in the acoustic image

The array design: In a microphone array, the performance is improved by having microphones close enough to eliminate spatial aliasing at high frequencies with a large enough aperture to maximize source resolution at lower frequencies. If the number of transducers is limited, then a logarithmic array [28] can be quite advantageous, since it extends the frequency range that can be considered by a limited number of transducers. Typical designs which cater to the limited space are the rectangular and circular arrays (planar). In a planar array configuration, the spiral array provides a good compromise between spatial resolution and spatial aliasing for a limited number of receivers [36]. This was vastly studied by Underbrink [37], in his single arm and multi arm spiral array configurations (Figure 2.20). For an equal spacing along the spiral for M transducers, Underbrink [38] gives

$$h\theta_m = \ln\left(1 + \frac{(m-1)(r_{max} - r_s)}{(M-1)r_s}\right)$$

For a multi-arm spiral design, the radius and angle of the n^{th} microphone and m^{th} arm are defined in polar coordinates as

$$\phi_{\mathrm{m,n}} = \frac{ln\frac{r_{m,n}}{R_o}}{\cot v} + \frac{m-1}{N_a}2\pi$$

$$r_{m,n} = \sqrt{\frac{2n-3}{2N_m-3}}R_{max}$$

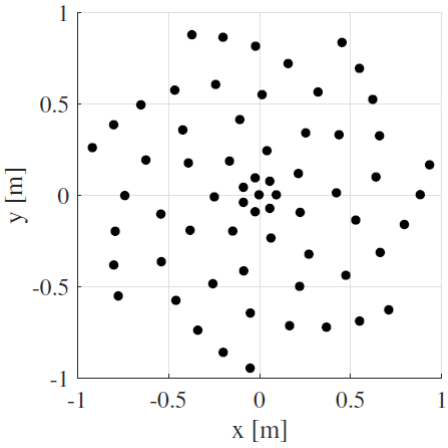

Figure 2.20: Underbrink's configuration of multi arm array [37]

Flush mounted microphones:

Flush mounted microphones are usually installed to account for the high intensity hydrodynamic fluctuations. There are post processing techniques which can negate these spurious contributions , but their performances are limited to certain frequencies and would additional supplementary tests. These fluctuations can arise from the boundary layer on the walls. Flush mounted microphones, hence, indirectly, also increase the signal to noise ratio of the sources under consideration.

Apart from installing flush mounted microphones, recessing and covering the recess with a material that can filter out the hydrodynamic fluctuations has been researched by NASA [39], and Kevlar has been found to be the best suited material. But, it was also recognized that high frequency spurious noise was produced due to the interaction between the cloth and the turbulence [40]. Metallic cloths [41] were also studied, since the wire diameter can be as small as 20 μm and the weave size, around 100 μm, which is smaller compared to the size of Kevlar. Hence, they provide a good tradeoff between flow-noise suppression and low acoustic impedance. Also, the metallic cloth were easier to install compared to Kevlar. Recessing a microphone from the walls can induce a piston mode, where the acoustic waves are constantly reflected and attain resonance. This can cloud the measurements of a recessed microphone and is attributed to the presence of a hard wall which houses the microphone. The spurious effect, which was a part of insertion loss, was isolated [41] by adding a foam material and the result is depicted in Figure 2.21.

Better attenuation characteristics of turbulent wall pressure fluctuations was observed for a microphone recessed Kevlar covering when compared to a flush mounted microphone without any recess (Figure 2.22a). In addition to this, different types of recessions were studied, which included a cylindrical aperture, a conical aperture and a deep, recessed plate and was concluded that a deep, recessed plate attenuated the hydrodynamic fluctuations the most (Figure 2.22b).

On comparing the Kevlar cloth and metallic cloth, it was observed that Kevlar did a better job in attenuating the hydrodynamic pressure fluctuations but the metallic cloth had better workability.

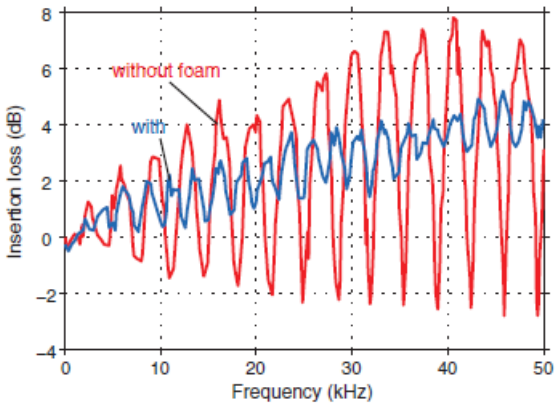

Figure 2.21: Insertion loss of kevlar cloth covering a recessed microphone [41]

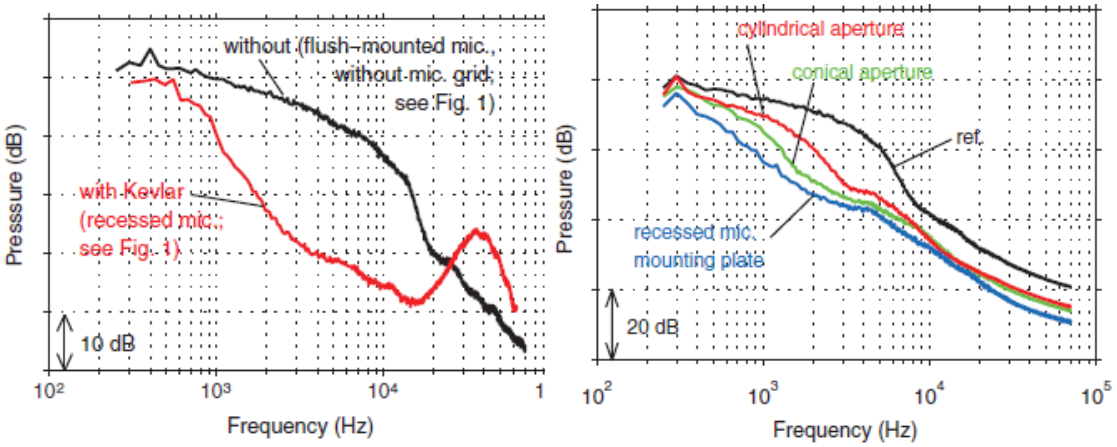

(a) Flush mounted vs recessed microphone [41]

(b) Comparison of different types of recession [41]

3

Experimental setup

The experimental setup for this thesis involves two configurations. Detailed explanation of each configuration with the measurements performed in these will be explained in this chapter.

3.1. Rod - Single Airfoil (RSA) configuration

The first configuration involved an open test section with two flat plates on which a rod and a wing can be mounted (Figure 3.1). Isolating the OGV blade to analyze the vortex-airfoil interaction noise was not possible, since the flow separates over the OGV blades. Hence, was was required, for the isolation of vortex-airfoil interaction noise that a differet airfoil having the same aerodynamic and acoustic characteristics as the OGV in the RLC configuration be sought after. The search for a blade which would preserve the same mean aerodynamic loading as that of the OGV blade, when placed in a cascade environment and under the influence of the vortex shed from the rod, was pursued.

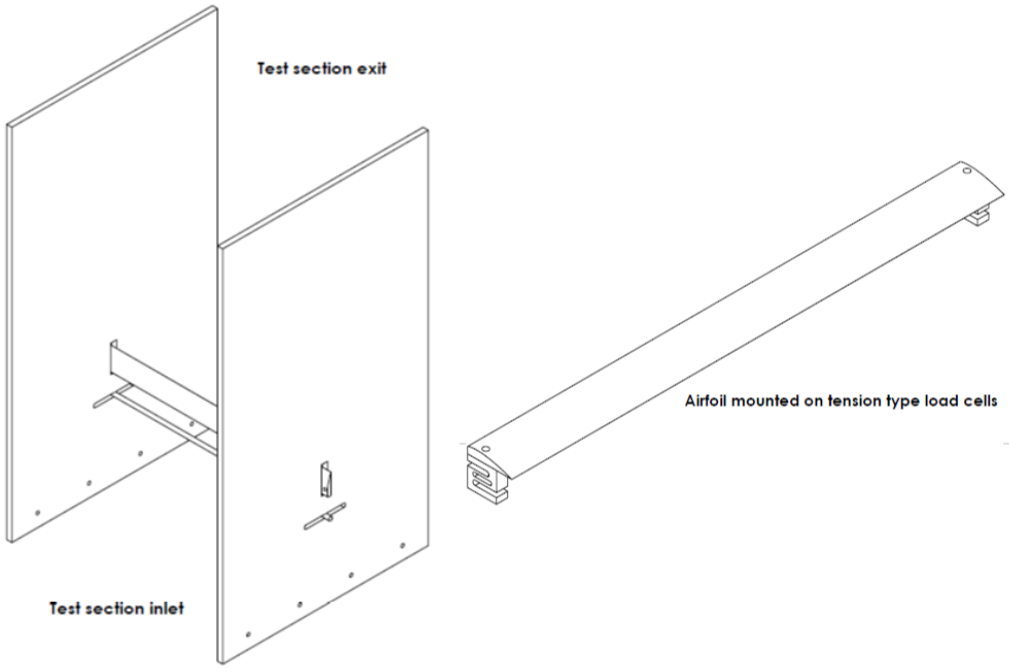

Figure 3.1: Rod-Single Airfoil setup (Left); Wing mounted on load cell attached to the flat plate externally (Right)

The result of this search was a NACA 5406 airfoil at 8 ° angle of attack. Also, from literature, it was seen that the leading edge radius and thickness of the airfoil had a significant on far-field acoustics. Geometrical

similarity in terms of thickness (6%) was maintained the same since, of all geometrical parameters of an airfoil, thickness was universally found to affect the far-field noise. Also, the leading edge radius was similar to that of the OGV blade. Other parameters like angle of attack and camber were observed to have negligible effect at low angles of attack, less than 12 °. The NACA 5406 used for this experiment had a chord of 40 mm and a span of 400 mm, the same dimensions as the OGV blade [3]. The diameter of rod used for this setup was 4mm. The housing of the rod was designed to allow movement/relocation of rod in the transverse direction with respect to inflow direction, for partial spanwise wake impingement analyses. Far-field acoustics due to partial spanwise wake impingement was also studied using this configuration. The experiments were performed at 4 different velocities, 30 m/s, 40 m/s, 50 m/s and 55 m/s.

3.2. Rod - Linear Cascade (RLC) configuration:

The second and the most important configuration was that of the RLC [3] (figure 3.2). The RLC consists of OGV blades with a rod placed upstream in a curved test section. The contraction shown in figure 3.2 was to increase the velocity to 60 m/s. The setup was to be mounted on the Anechoic Vertical Tunnel at Delft University of Technology. The contraction was 1m long and had a circular inlet with a diameter of 0.6m and a rectangular outlet of 0.4m wide and 0.25m high. Consequently, the test section was designed with the same dimensions as the contraction outlet, with its width equal to the span of the rod and the cascade blades (i.e., 0.4 m). For compensating the flow deflection induced by the linear cascade (i.e., 40 °), the test section included a curved segment upstream of the RLC, where the in-flow is turned in the direction opposite of the flow deflection angle. This treatment also prevented the outflow from the test section from potentially damaging the walls of the anechoic chamber when an experiment was to be performed. The curved segment started at 50mm downstream of the test section inlet and ended at 180mm upstream of the rod center. The radius of curvature (i.e., 650mm) had been carefully chosen to avoid flow separation within the test section.

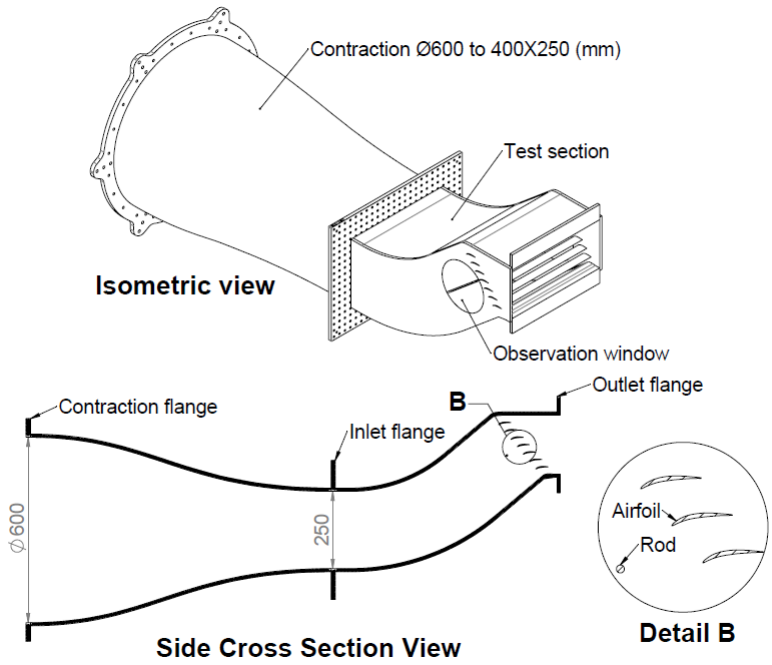

Figure 3.2: Rod-Linear cascade setup [3]

It is important to mention that the side wall downstream of the cascade blades on the suction side was removed to enable the calculation of BGN with lesser installation effect, and that the turning would be uniform only in the presence of the cascade blades. But the wall that was cut-off could not be attached later on. Thus, all the acoustic measurements in this configuration were a consequence of a non-uniform exit plane. Though the exit plane of the test section was not uniform, the flow still exited vertically (was verified by attaching tufts to the cascade blades).

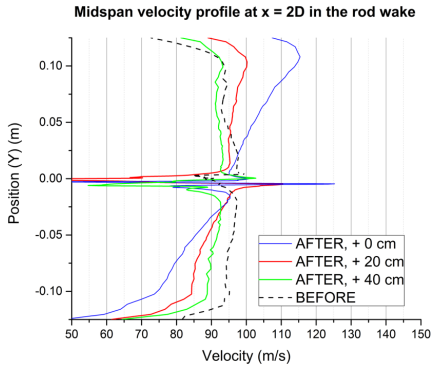

Figure 3.3: Analysis of curvature before (BEFORE) and after (AFTER) the cascade, measured in streamwise direction

Geometric scaling of the OGV blade in a cascade of a turbofan bypass duct can be envisioned as choosing a location, where significant acoustic energy is produced due to high mean flow velocity. This location would be the actual cascade blade tip (or near it), since, the velocity increases with increasing radius ($v = r\omega$) and ensures that the flow-surface interaction noise accounted for will be sufficient to address the interaction noise generated at other blade locations as well. For this thesis, the cascade profile was taken from NASA Glenn Source Diagnostics Test (SDT) rig [42], sampled at 90% of the outer radius. The SDT OGV profile was scaled at 1:1 and extruded to obtain a blade that spanned 400mm with constant chord. The blade solidity was also an important parameter which must be maintained in an OGV configuration, to represent the flow physics and was significant in addressing the acoustic interactions between one blade and the other [21]. Maintaining the same solidity at the location of the blade tip (or the location at which the OGV blade is sampled) ensured this condition. The solidity (σ) of the OGV in the SDT rig at the selected radial location was 1.22, which corresponded to a blade-to-blade separation of 32.5 mm. With the given cascade solidity, 7 blades were accommodated within the test section. The blades were installed at an incidence of 1 ° to achieve the blade outlet angle as measured from previous numerical studies on the SDT rig, and at 29 ° stagger angle to ensure that the leading edges of all the blades were at the same stream-wise distance from the rod.

Additionally, carborundum particles (grit type transitional element) of thickness 0.2 mm were installed in a sparse manner on both the suction and the pressure sides of the blades at 10% chord length from the leading edge to force laminar-turbulent transition. Experiments [43] had revealed that the transitional Reynolds number based on grit height was approximately 600 (for a ratio of particle height to width of 1) which corresponded to a grit height of 0.147 mm for the current flow speed. It was also observed that an increase in the grit height by a factor of 2 can be related to very little or no drag increase. A grit size larger than what corresponded to Reynolds number of 600 was proposed to ensure a margin for conservatism for transition. Hence value of 0.2 mm.

The function of the rod was to mimic the rotor. This was to done by designing a rod which shed vortices at the same frequency as that of first Blade Passage Frequency (BPF) of the SDT fan (≈2.87 kHz). The rod diameter and flow velocity were the parameters modified to maintain the same frequency. The velocity chosen here was slightly lower than that measured in the SDT fan stage at approach conditions (i.e., 49.3 % of the maximum RPM) due to the limitation of the wind tunnel facility where the experiment was planned. For the current configuration, this corresponded to a rod diameter of 4 mm and a mean flow velocity of 60 m/s.

Certain limitations were imposed during runtime which led to a change in the measurement variables. The airfoil profile manufactured was at 5.71 ° angle of attack instead of 8. The wind tunnel velocity could only handle 58 m/s at maximum rpm with some fluctuations. Therefore, the maximum attainable stable speed configuration was 55 m/s, which corresponded to a shedding frequency of 2.68 kHz for the open test section, and 40 m/s for the RLC configuration (due to blockage), corresponding to a shedding frequency of 2 kHz. A rod of smaller diameter to obtain the same vortex shedding frequency could not be manufactured owing to manufacturing constraints. Since the overall aim of the experiments was to test the ability of the test section to predict the vortex- cascade interaction noise, the experiments were still performed taking into account these constraints.

As regards to the acoustic measurements, a directivity arc (figure 3.4) was designed for this experiment, also accounting for future research at TU Delft. It was made of two semi-circular arcs, each with it's own base, over which 16 microphones per arc can be mounted currently. The housing for the microphones were dynamic and not fixed, hence the microphones can be rotated about its location in the arc. Both 1/2 inch

and 1/4 inch microphones can be used in this semi-circular arc. The radius of the arc was designed so that the microphones measure at 1m from a reference location, the location being the rod for this experiment. The main motivation behind the design of the arc was to obtain the directivity of various noise sources. The arc has housings made of 3-D printed material (shown as green cubes in figure 3.4) which can accommodate microphones with different sizes.

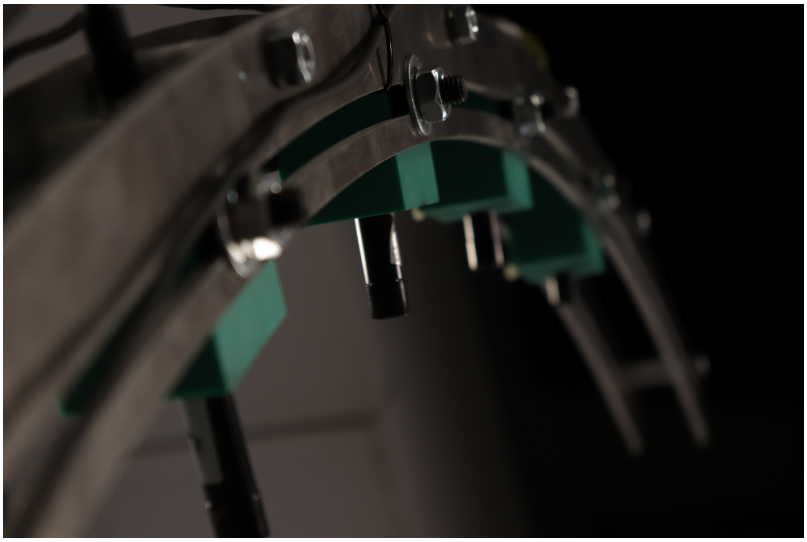

Figure 3.4: Microphones mounted on the dynamic arc for directionality measurements

The microphones used for directivity measurements were LinearX M51 and M53 (also shown in figure 3.4). They are high performance low voltage electret condenser microphones and are 8 in number. The operating voltage is around 9-11 V, with 150 dB SPL capability. On the other hand, 16 smaller Sonion 8400 microphones were used for beamforming array. A typical operating range of these microphones are 0.9 V, with a measurement capability of 123.5 dB.

The beamforming array was used instead of a single recessed microphone, to try and isolate the reflections occurring in the test section. The recessions were then covered with metallic mesh, capable of attenuating the hydrodynamics, allowing only the acoustic waves to pass through. The array design followed the Underbrink's configuration of multi-spiral arrays [37]. Due to manufacturing and space constraints, the maximum number of microphones installed were 16, with each arm containing 5 microphones (3 arms in total) and one central microphone. This configuration also allowed the placement of a reference microphone in between two arms. The minimum distance between two consecutive microphones was 22.4 mm and the maximum was 62.1 mm. The array diameter was non-uniform, with the diameter in the stream-wise direction being 0.12 m and in the span-wise direction, being 0.28 m. This is shown in figure 3.5

Calibration devices used for the experiment, as mentioned before, include the pistonphone and the omnidirectional source. The output from the pistonphone was a known pressure amplitude at a particular frequency and was used for amplitude correction. The output from this particular device was a 114 dB sound level at 250 Hz. The omnidirectional source, on the other hand, had numerous settings, and was used for frequency calibration. It had an inbuilt amplifier and the utilized setting was 45 dB amplifiation. The obtainable broadband noise sources can be varied as white noise or pink noise. White noise was chosen since it has equal intensity throughout the frequency range of operation, the range being 500 - 6300 Hz (again, a setting in the omnidirectional source).

Velocity statistics with a good temporal resolution could be obtained using Hot-Wire Anemometry (HWA). The acquisition frequency of the hot wire anemometer setup used was 50 kHz. The locations where Hot-Wire measurements were performed include; upstream of the rod in clean flow, in the rod wake, and at different vertical locations (in between cascade blades) near the leading edge impingement region and at the exit. These locations are depicted in figure 3.6. The rod was translated forward and the measurements are taken 41 mm downstream of the rod location. Measurement at the exit plane was taken at 5 rod diameters away from the test section exit, i.e., 20 mm from the exit plane. also notable from the figure is the nomenclature of the blades, C being the central blade, B being series of blades bottom of C and T being the series of blades on top of C.

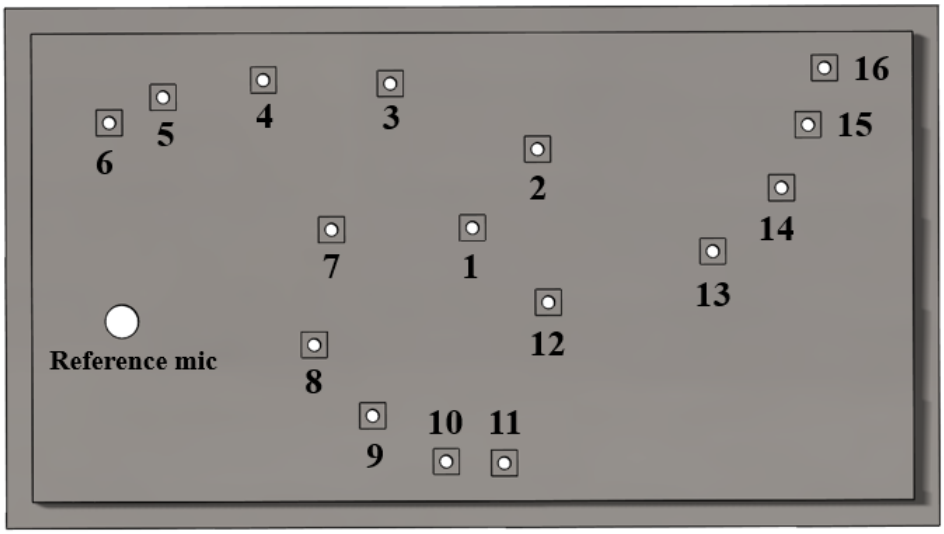

Figure 3.5: Recessed microphone array and its nomenclature

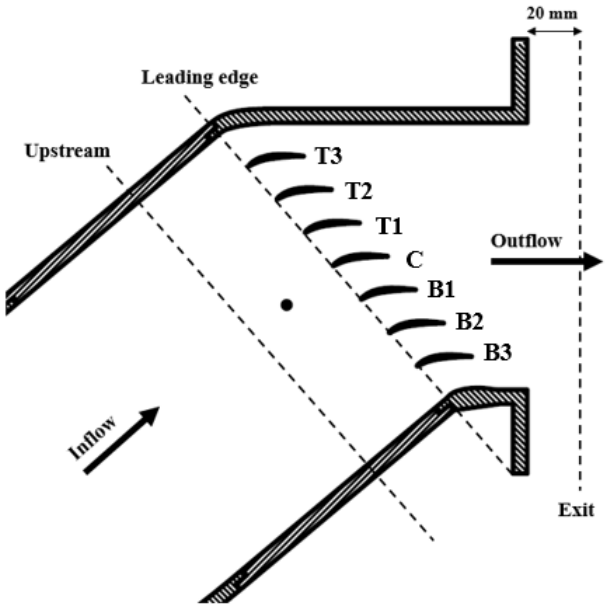

Figure 3.6: Hot wire measurement locations

The measurements done using hot wire in the downstream were enabled using an automatic 3-D traverse system provided by Zaber®. The maximum traversing length for two axes was 150 mm and 300 mm for the third axis. Due to the complexity of the RLC model, the HWA measurements to be performed were classified into two based on the location of measurement. For the first two cases, i.e., upstream of the rod or in the rod wake, a novel airfoil strut was designed to house the hot wire probe. This strut was designed to pass through the same slot as that provided for the rod. The airfoil strut was used instead of a cylindrical holder so that it does not oscillate under the influence of the wake like a cylinder does. The manufactured strut is shown in figure 3.7.

For the third case, i.e., in the location of cascade blades, a separate filament holder was used which was inserted from the exit of the test section using a connecting rod, long enough to place the filament in the impingement region, and small enough to fit in-between the cascade blades. HWA was used in an attempt to obtain the velocity spectra at different locations and be able to address the far field noise. The novel hot wire airfoil strut could also be used for future experiments which utilize HWA.

Figure 3.7: Airfoil shape strut for hot-wire measurements

3.2.1. Simulation of the Hot-wire strut

A 2-D Ansys Fluent simulation was done on the airfoil strut profile. The reason behind this simulation was to find the location ahead of the airfoil, where stagnation streamline started curving, so that design can be achieved appropriately. The distance from the leading edge of the strut to the location where the streamline started bending was compared with the positioning of the hot wire filament, and it was concluded that the filament samples at a location well ahead of the location of the bending of the stagnation streamline. As seen in Figure 3.8, the distance between the location where the streamline starts bending and the leading edge is approximately 4.5 mm, which was well behind the sampling location measured in streamwise direction.

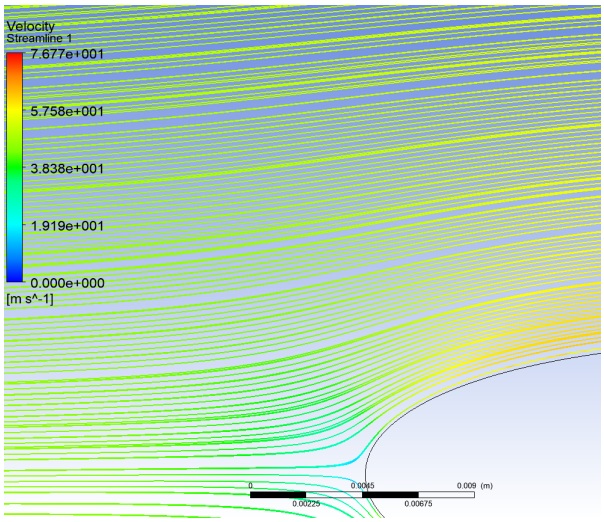

Figure 3.8: 2-D simulation on airfoil shaped hot wire strut

3.2.2. Simulation of beamforming capabilities of the microphones in the RLC configuration

As mentioned in literature, the underbrink array configuration was chosen initially for beamforming, in an attempt to isolate and quantify the different sources from the OGV blades, and also to analyse the upstream propagation of acoustic waves, against the flow. The minimum frequency, based on the resolution (distance between two different sources) required for the isolation of sources was given by Rayleigh's criterion [33]. Calculation of this frequency for the current configuration resulted in approximately 7 kHz, which was slighty more than the frequency range of interest [3]. To cross verify and validate this prediction, a small simulation was performed. In this simulation, the casacde blades were considered as having point sources and the microphones were located in a plane perpendicular to the cascade blades (respresnting actuality). For our analysis, monopole sources of equal strength were considered for all the blades and the source autopower

A, at a source located at a grid point ξ_j was obtained by minimizing the difference between the recorded pressure vector, p, and modeled pressures for a source at that grid point ξ_j [34]. This formulation is given as:

$$A(\xi_j) = w_j^* C w_j$$

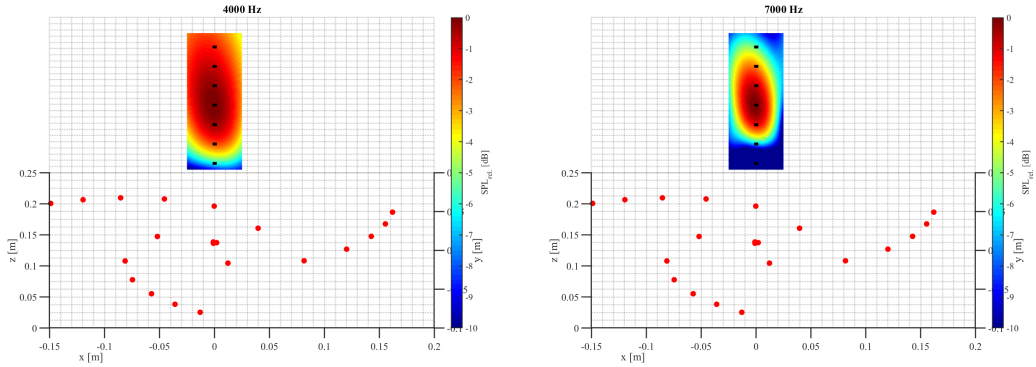

Figure 3.9: Source power snapshot taken at 4kHz (left) and 7 kHz (right) considering the central blade as the only source

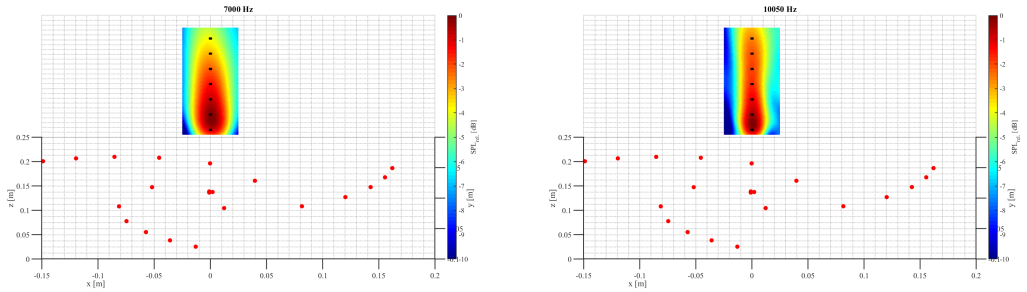

Figure 3.10: Source power snapshot taken at 7kHz (left) and 10 kHz (right) considering equal power on all 7 OGV blades

Plots of source autopower were extracted and is shown in Figures 3.9 and 3.10. Initially, the central blade was considered as the only source and the corresponding source autopower plots obtained are shown in figure 3.9. The central blade source was clearly distinguishable from the next consecutive blade (31.25 mm) only from around 7 kHz and that it was not possible to distinguish at a lower frequency, around 4 kHz, which was expected. A similar analysis was done considering equal sources for all the 7 blades kept at mid-span and the results are plotted in figure 3.10. As observed from the figure, the sources are distinguished starting from a frequency of 10 kHz and not at any frequency below it.

From this analysis, it was concluded that beamforming to isolate the sources was not satisfactory for the current thesis, owing to constraints of the current setup. But the beamforming array was still retained throughout the experimental campaign. This was done to improve the SNR inside the test section, so that the upstream propagation of noise from the cascade could be quantified. If a beamforming array were absent, the measured value would be clouded by the reflections from the walls, defeating the very purpose of the having the array to quantify the upstream propagation.

4

Results and discussion

This section deals with the results extracted and analysed from the two configurations, RSA and RLC. The results are methodologically explained , thereby also including the procedure used to obtain them.

4.1. RSA configuration:

As mentioned before, the experiments were first performed on the RSA configuration and acoustic measurements were performed. Important results from this experiment include partial spanwise wake impingement, with emphasis given on the scaling laws and the relative dominance of this noise source with other types of sources such as vortex-leading edge interaction noise and Turbulent Boundary Layer-Trailing Edge (TBL-TE) noise. Other results from this configuration include the estimation of mean aerodynamic load, lift, using compression type load cells. The directivity of noise in far-field for this configuration was obtained by using 8 microphones, 4 on the suction side and 4 on the pressure side. The microphone placement angles are shown in figure 4.1.

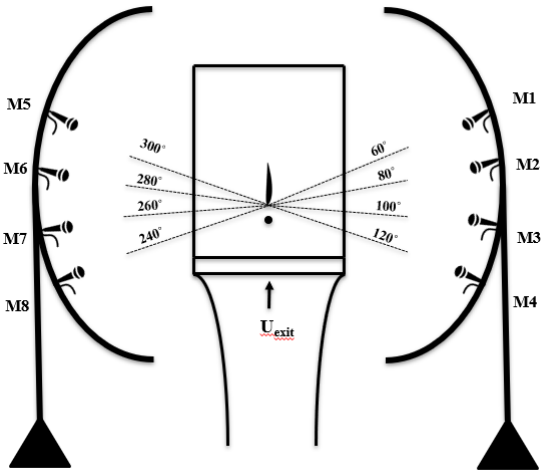

Figure 4.1: Far-field microphone placement; *In-flow from bottom to top, as indicated*

The first step in any experiment is the calibration of the instrumentation used for extracting data. For the far-field measurements, amplitude calibration of microphones in the directivity arc was done using a pistonphone, which gave the sensitivity of the microphones. Sensitivity is defined as

$$\text{Sensitivity} = \frac{\text{Pressure(Pa)}}{\text{Voltage(V)}}$$

and has a S.I. unit, Pa/V. The sensitivity values of different microphones are tabulated as shown in table 4.1.

Mic 1	10.01
Mic 2	110.94
Mic 3	9.91
Mic 4	7.73
Mic 5	8.35
Mic 6	76.91
Mic 7	6.86
Mic 8	104.01

Table 4.1: Pistonphone calibration

The results discussed further are in the same chronological order as the experiments. The experiments were performed at different velocities, 20 m/s, 30 m/s, 40 m/s, 50 m/s and 55 m/s. Scaling laws were obtained by averaging the OSPL values from the microphones on the directivity arc and suitable explanation was given for the procedure undertaken. The MATLAB function ,**pwelch**, was utilized to calculate the Power Spectral Density (PSD) using Welch's method. A Hanning window was used in all the measurements to ensure continuity between segmented signal windows. PSD was calculated in 25 Hz bands and SPL values were obtained as

$$\mathrm{SPL} = 10 \times \log_{10}\left(\frac{\mathrm{PSD} \times \mathrm{df}}{{\mathrm{P_{ref}}^2}}\right)$$

where df is the bandwidth in Hz, P_{ref} is the reference pressure which is 2e-5 Pa.

4.1.1. Turbulent Boundary Layer- Trailing Edge (TBL-TE) noise

The first experiment in this configuration was the measurement of airfoil self-noise, or in this case, the TBL-TE noise. This experiment was performed to enable a comparison with other noise sources of interest, the vortex-leading edge interaction noise and that due to partial span-wise wake impingement. The sound pressure levels measured are shown in figure 4.2.

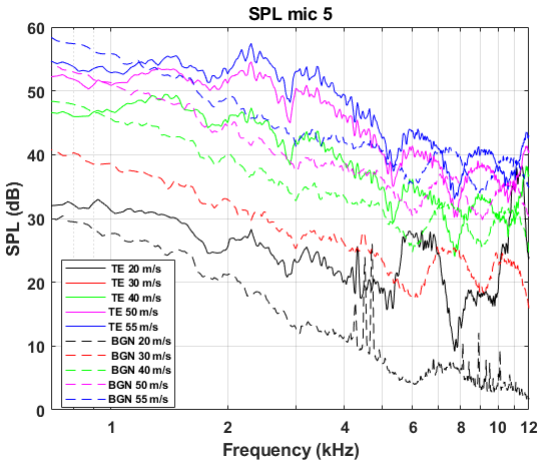

Figure 4.2: SPL of TBL-TE noise at different velocities; *Note: Absolute levels of background noise are plotted in dashed lines for reference*

The Reynolds number based on the chord was obtained to be 0.1-0.135 $\times 10^6$. Tripping was done to maintian the control variables in design (the cascade blades of RLC had trips installed on them). tripping also ensured early transition from laminar to turbulent boundary layer.

For any analysis, it was important to decide the frequency range of interest to be utilised. From figure 4.2, it was seen that with an increase in velocity, the frequency range at which the flow-self noise was dominant over the TBL-TE noise increased. To enable a common frequency range which can be used for any analysis, the maximum velocity (55 m/s) was taken as the reference, the corresponding frequency being 1000 Hz. Hence, the overall frequency range of interest was considered to be 1000 - 12000 Hz.

Velocity (m/s)	X-Foil predicted δ^* (in m) NACA 5406	Empirical formula predicted δ^* (in m) NACA 0012
30	1.32e-4	0.0075
40	1.16e-4	0.0073
55	1.01e-4	0.0007

Table 4.2: Displacement thickness δ^* for NACA 5406 and NACA 0012 [44]

The scaling of TBL-TE noise was done to analyse the dependence of noise on the flow parameters and geometry. To obtain the dependence of the noise with flow speed, the Overall Sound Pressure Level (OSPL) was calculated in the frequency range of interest (1000 - 12000 Hz), and is plotted (as shown in figure 4.3a) as a function of velocity for every microphone. Scaling laws are usually obtained using PWL, but due to the limited number of microphones used, the estimated PWL would provide an improper prediction. Hence the effective OSPL per velocity was obtained, by averaging the values between microphones, neglecting the effects of directionality of the noise source. This was an approximation, since the directionality is also velocity (hence frequency) dependent. To validate this assumption, a quick analysis from X-FOIL for obtaining the δ for three different velocities, 30, 40 and 50 m/s (shown in table 4.2) shows that there is a minimalistic change. Since the maximum energy content of TBL-TE noise is concentrated on the integral scales (approximated by δ), the change in directionality for the given velocities could be considered to be negligible.

A linear curve fitting was utilized to predict the scaling law (the slope of the curve gives the exponent of U). From analysis of individual microphones, it was seen that scaling law obtained had a range of $U^{5.6}$ to U^6, the higher values shown by microphones with higher sensitivities. Hence, by averaging the OSPL values between microphones having lower sensitivities and applying the linear curve fit to the averaged data, the noise scaled with $U^{5.79}$. The standard deviation of microphones from the averaged value was calculated to check for any inconsistencies and is shown in figure 4.3b. It is seen the difference in values measured by microphones per velocity do not differ much (less than 0.5 dB) for the velocity range under consideration. The maximum deviations are measured by microphones with high sensitivities (microphones 2 and 8). This means that source directionality in the velocity range of interest has negligible change and this validates the use of the method of averaging, to obtain the scaling laws.

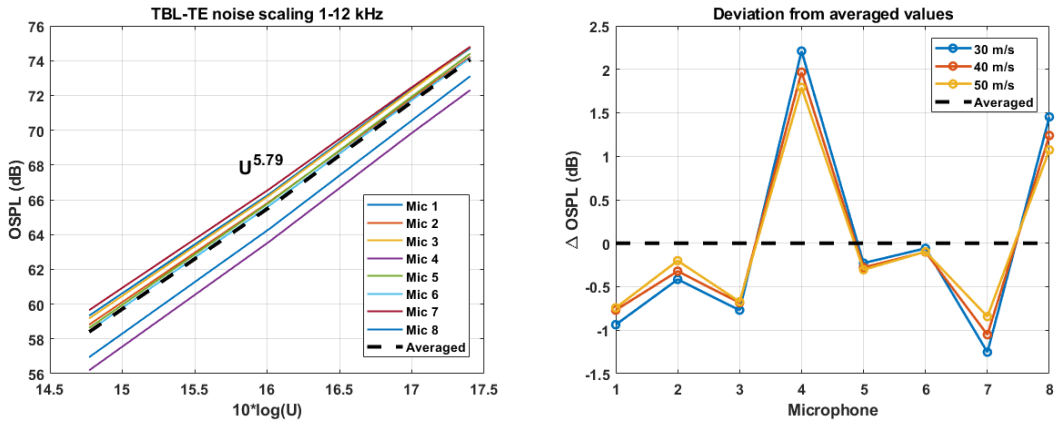

(a) Scaling law for TBL-TE noise

(b) Deviation of measured OSPL from averaged levels

Figure 4.3: Analysis of scaling laws for TBL-TE noise, velocities under consideration being 30,40 and 50 m/s

The scaling parameter used usually in TBL-TE noise case is the Strouhal number, defined as;

$$St = \frac{f\delta^*}{U_\infty}$$

But, a good look into the sound pressure spectra (figure 4.4a) shows that the far-field noise due to turbulent boundary layer exiting the trailing edge was not frequency dependent, hinting at the possibility of a Helmholtz scaling, rather than Strouhal scaling.

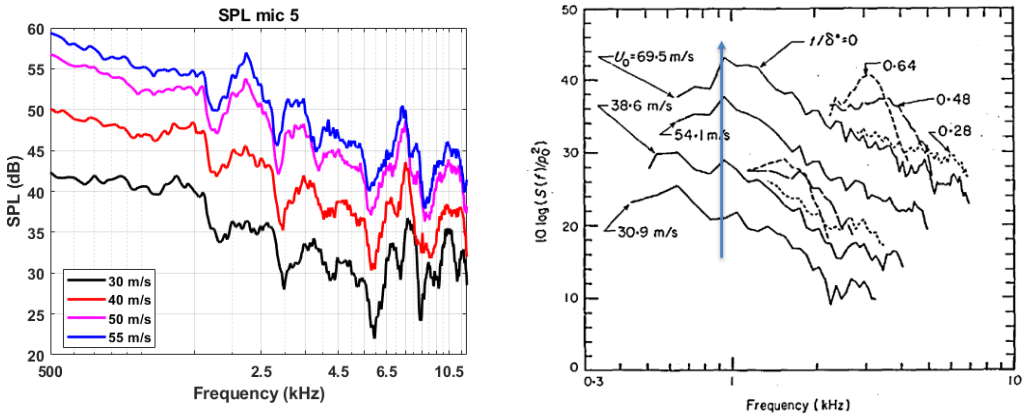

(a) NACA 5406 from experiment

(b) NACA 0012 from experiment of Brooks[44]

Figure 4.4: Left: SPL of TBL-TE noise; arrow indicates that scaling might not be flow dependent, rather geometry dependent; Right: Sound pressure spectra from teh experiment of Brooks [44]

Brooks [44] had observed similar results (shown in figure 4.4b) when calculating the far-field pressure spectra of NACA 0012 airfoil with a geometric angle of attack of 0 ◦. Displacement thickness for NACA 5406 airfoil were extracted using X-FOIL. Empirical formulation as derived by Brooks et. al. [45] was used in extracting the values of δ^* for NACA 0012 and is shown in table 4.2.

The displacement thickness of the boundary layer for the different flow regimes considered show that there is no significant change in δ^*, i.e., it is of the same order. This could be a possible explanation for the flow features not shifting to higher frequency with an increase in velocity. Hence a scaling law, i.e., Helmholtz scaling based on span of the airfoil, rather than chord, was utilized. It is formulated as,

$$\mathrm{He} = \frac{\mathrm{f^* L}}{\mathrm{c_o}}$$

where c_o is the speed of sound in m/s and L is the span of the airfoil, in m.

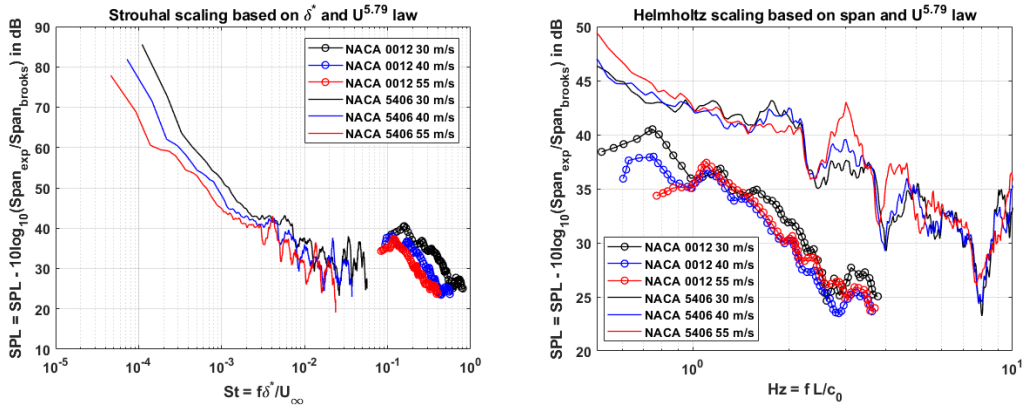

(a) Strouhal based scaling

(b) Scaling based on Helmholtz number

Figure 4.5: TBL-TE noise scaling, data for NACA 0012 extracted from the experiment of Brooks [44]

As seen from the figures 4.5a, 4.5b, scaling with Strouhal number did not give satisfactory results, for both the experiments, whereas, scaling with Helmholtz number brought the spectra from both the experiments together. The sound pressure levels in both the figures have been scaled to account for the difference in span. The difference seen in the amplitudes of NACA 0012 and NACA 5406 could be attributed to the difference in thickness of the airfoils under consideration since it was shown that an increase in thickness caused a reduction in the sound levels [12].

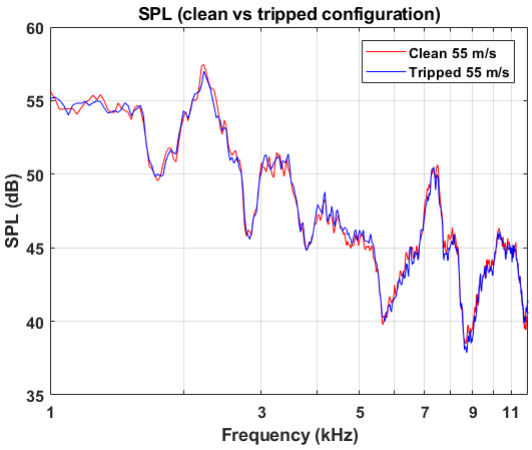

Figure 4.6: Averaged SPL values for tripped vs clean case at 55 m/s

To check for the effect of trip on the TBL-TE noise, a small experiment was done with a clean configuration (no trip), at 55 m/s and the results are plotted in figure 4.6. Surprisingly, the power spectra obtained for every microphone, for both the cases, tripped and non-tripped, were identical. This meant that the trip had no effect in forcing transition, for this case.

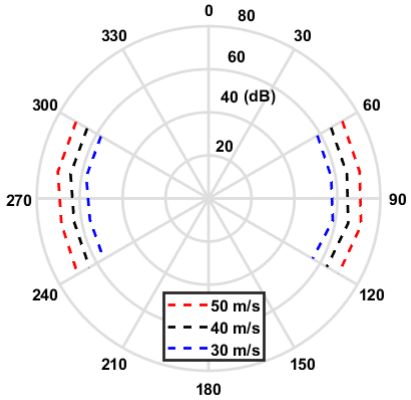

Figure 4.7: Directivity of TBL-TE noise as seen by the microphones; *flow from bottom to top*

The directionality of the TE noise was obtained using all the microphones in the directivity arc at different velocities. This is shown in figure 4.7. **Note:** The left hand side of the directivity plot represents the pressure side and right side represents the suction side of of NACA 5406. The flow direction is from bottom to top, as shown in figure 4.1. This convention will be followed in all directivity results for this configuration.

4.1.2. Vortex-leading edge interaction noise

The default configuration of this experimental campaign was the one with the complete span-wise wake impingement due to vortices shed by the rod. The pressure fluctuations created due to vortex impinging and stretching over the leading edge of the wing are expected to have a higher intensity than that created due to the boundary layer exiting the trailing edge. Hence, the noise produced due to this mechanism of vortex-leading edge impingement is expected to dominate the airfoil sef-noise. This experiment was hence performed to bolster the typical dominance of the vortex-leading edge interaction noise over TBL-TE noise. A small check was done to verify that the placement of rod resulted in a proper leading edge impingement, to ensure that the rod wake did not convect away from the LE with lesser interaction. It was observed that the placement was good enough to result in an accurate impingement of vortex on the LE. This result is shown in Appendix-C. The SPL spectra calculated from the experiments for different velocities are shown in figure 4.8

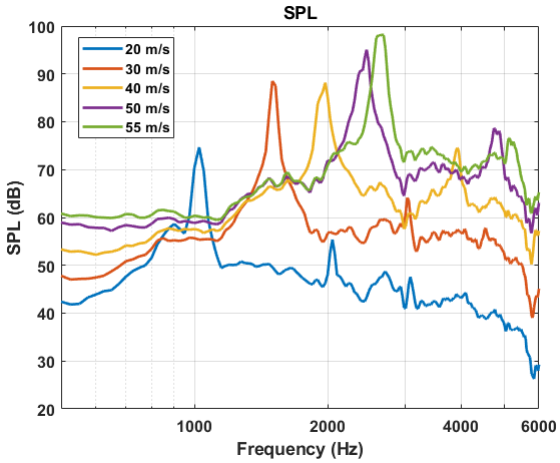

Figure 4.8: SPL spectra

The scaling law for this noise is discussed first. From previous experiments, [13], it was seen that the fundamental peak scaled with $U^{5.2}$. A similar methodology was utilized in obtaining the scaling law for the most dominant contributor to the noise using the fundamental peak. This is depicted in figure 4.9a, where the slope of the curve resulted in the exponent of velocity, and was found to be $U^{5.11}$. The dominant contributor to the noise is due to the localized pressure fluctuations on the leading edge of the blades.

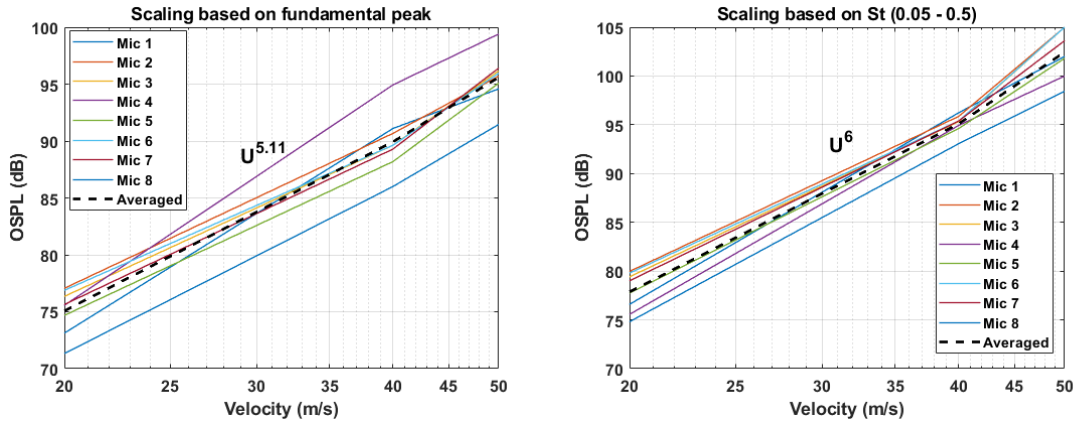

(a) Scaling based on fundamental peak

(b) Scaling based on Strouhal range

Figure 4.9: Analysis of scaling laws for vortex-leading edge interaction noise

The same method of averaging between microphones was performed, since the scaling law varied from $U^{4.6}$ to $U^{5.6}$ between microphones. The deviation from averaged value for the fundamental peak is plotted in figure 4.10a. The maximum deviations between microphones for different velocities was found to be around 3 dB for the velocity range under consideration. Nevertheless, averaging between the fundamental peaks from different microphones gave an excellent result.

Another scaling routine was performed to see how the total noise scales. The OSPL was calculated in a Strouhal range (based on rod diameter, 0.1 - 0.42) which included the fundamental, the first harmonic and the broadband levels in-between the peaks. This is shown in figure 4.9b. The scaling law obtained from the same microphone showed U^6. This could mean that, although the dominant noise production mechanism arises only due to the edge diffraction phenomenon at the leading edge, the pressure fluctuations over the entire surface of the wing could be of the same order when considering the overall levels, thus radiating to the far-field as a compact dipole.

The deviations between microphones for this analysis are also calculated and shown in figure 4.10a. Thus, it is seen that, by following the methodology prescribed, it would be possible to isolate mechanisms of sound production from the overall noise to see their relevant scaling with velocity.

The results of this experiment were also compared with the benchmark experiment of Rod-Airfoil configuration [13].

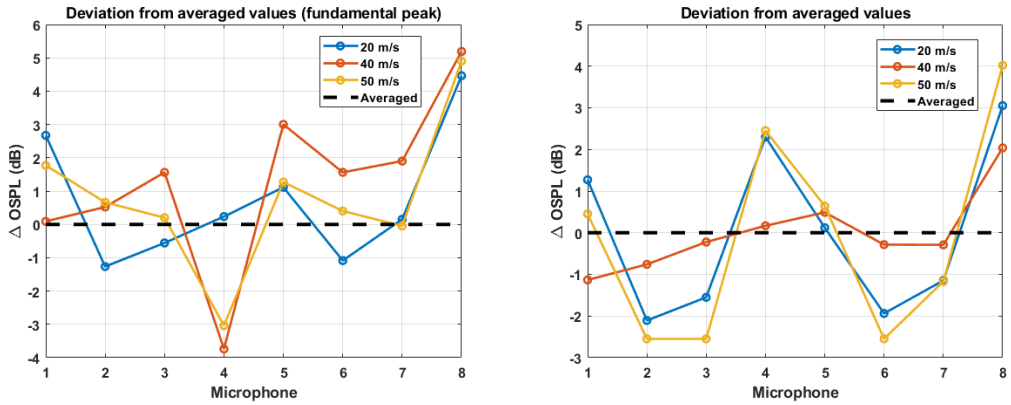

(a) Deviation in fundamental peak (b) Deviation in Strouhal range

Figure 4.10: Deviation of measured OSPL from averaged levels

The directionality of this noise source can be visualized using the OSPL obtained in the frequency range of interest from each microphone at different velocities. This is shown in figure 4.11. It is also worthwhile to note the very minimalistic change in the directionality of vortex-leading edge interaction noise in the given velocity range of interest, also validating the methodology used in calculating the scaling laws.

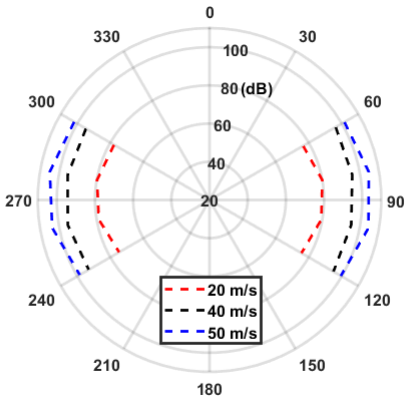

Figure 4.11: Directivity of vortex-leading edge interaction noise; *flow from bottom to top*

4.1.3. Partial spanwise wake impingement

The far-field noise due to partial span-wise wake impingement on the leading edge of the wing was analysed since it will be important to replicate similar conditions in the RLC configuration. This experiment was performed because in an actual turbofan bypass duct, the blade wakes impinges on all the OGV blades and in the current RLC configuration, impingement on all blades with a single rod can only be brought about by tilting the rod. This causes a partial span-wise wake impingement and only on inner 5 blades (T2-B2). Since there were no available literature on leading edge noise due to partial span-wise wake impingement, at an angle, this experiment was performed considering two vortex angles by varying the rod tilt, to observe the effect of vortex angle on the far-field noise. The rod tilt angle tested in this experiment would be the same angle of tilt which would be chosen in the RLC configuration, to achieve simultaneous impingement on the 5 blades.

The two different rod tilt angles chosen for the experiment were 9 ° and 18 °, which correspond to vortex orientations of 81 ° and 72 °. Tilting of the rod was achieved by translating the ends rod in the opposite direction, which was possible because of the slot present with bearings. The sound pressure spectra obtained for both the tilt angles is compared with the default configuration is shown in figure 4.12

Amiet [6], in his analytical formulation predicted a decrease in the amplitude of pressure pulse when the wake angle was decreased from 90 °. This was also observable from the experiment. With a decrease in wake angle (increase in rod tilt angle), the far-field sound pressure levels decreased and was attributed to two factors,

- Effect of vortex orientation on unsteady loading near leading edge
- Effect of wetted area of span

When the vortex is angled, the streamwise velocity fluctuations, u′ remain the same when compared to the case when the vortex is at 90 °. But the transverse fluctuations, v′, takes the angle of the vortex. Since the unsteady velocity fluctuations over the airfoil which contribute to lift act in the direction perpendicular to flow, only a component of the vortex, $v'\cos\theta$ contributes to the lift. This causes a decrease in the pressure fluctuations of the same order, reducing the radiated noise to the far-field.

When the rod is tilted, only a part of span was wetted by the rod wake, unlike the default configuration, where the whole leading edge is under the influence of rod wake. From Ffowcs Williams and Hawkings theory [46], the square of far-field pressure amplitude is proportional to the span, $p^2 \propto L$. The wetted region for the two cases of tilt can be estimated from the figure 4.12 and is given by the following equation:

$$SPL_f = SPL_p - 10 \times \log_{10} \frac{L_p}{L_f} \tag{4.1}$$

where SPL_f and SPL_p are SPL values concerning full and partial wake impingement. L_p is the wetted span due to partial wake to be estimated and L_f is the span of default configuration, 0.25 m. Considering the max values of fundamental peaks from figure 4.12, the wetted span for 9 ° and 18 ° rod tilt using equation (4.1) were calculated to be approximately 49 mm and 25 mm.

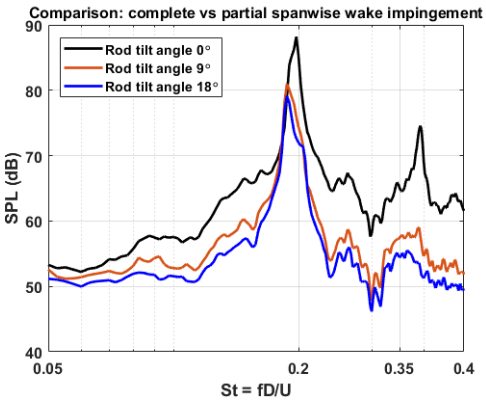

Figure 4.12: Comparison: full vs partial spanwise wake impingement at 40 m/s

Scaling laws were analysed for this noise source for both the vortex orientations. Similar to previous cases, the deviation from the averaged levels were calculated between the microphones, since the scaling law varied in the range of $U^{4.58}$ to $U^{6.05}$ for 9 ° rod tilt, and between $U^{4.2}$ to $U^{5.6}$ for the 18 ° tilt (based on strouhal range). The maximum difference in the levels of microphones per velocity was found to be 3 dB for the strouhal range under consideration. Since a partial span-wise wake impingement was also an edge diffraction phenomenon, it was expected that, this noise source also scaled according to U^5 law.

For 9 ° rod tilt, a similar methodology was followed in obtaining the scaling law. It can be seen from the figure 4.13a that the scaling law obtained is $U^{5.02}$, in the given strouhal range of interest. For 18 ° rod tilt, scaling within the strouhal range gave a scaling of $U^{4.8}$. This was an interesting observation, which could possibly mean that, with a reduction in vortex orientation from 90 °, a decrease in the rate of vortex-airfoil impingement noise with velocity was to be expected.

Scaling laws were also analysed for the fundamental peak, for both the vortex angles. It was observed that, for 18 ° rod tilt, the sound levels scaled as $U^{4.02}$, whereas for 9 ° rod tilt, the sound levels scaled as $U^{3.95}$. The reasons for this were unknown. Nevertheless, the plots of the analysis are presented in Appendix-C along with the deviation analysis for the microphone levels per velocity.

The directivity of partial spanwise wake impingement was also visualized using OSPL obtained in the frequency range of interest from each microphone at different velocities. Interestingly, the directivity of the partial spanwise wake impingement was found to be similar to the default configuration (figure 4.11) and the directionality of the noise source still followed that of vortex-leading edge interaction noise, only with changes in the amplitude and the scaling law. Again, the plots of this analysis are presented in Appendix-C.

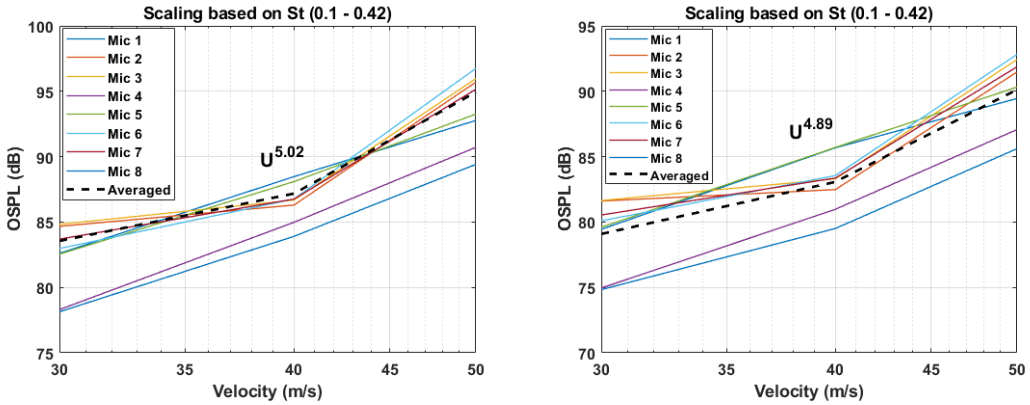

(a) Scaling based on Strouhal range

(b) Scaling based on Strouhal range

Figure 4.13: Analysis of scaling laws for partial spanwise wake interaction noise; Left: At a rod tilt angle of 9 °, Right: At a tilt angle of 18 °

4.1.4. Lift measurement

Lift experienced by the wing was measured using a compression type load cell. As mentioned earlier, the wing was manufactured in such a way that both the ends of the span rested on compression type load cells. Each of the load cell measured half the load acting on the wing, and summing the contributions from both, the total lift experienced by the wing was to be calculated. The attachment location to load cell was done by choosing the center of pressure as the suitable location to be fixed to the load cell. Owing to a few manufacturing snags, there seemed to be a problem of wing bending. But the bending was accounted for, utilizing a combination of displacement measurement using laser and analytical formulation, the details of which, are given in Appendix B. Open jet corrections were also done on this configuration and the method is detailed in Appendix B. At 40 m/s, a comparison of the corrected experimental C_l with X-Foil gave a difference of 6.1%.

4.1.5. Dominance of different noise sources

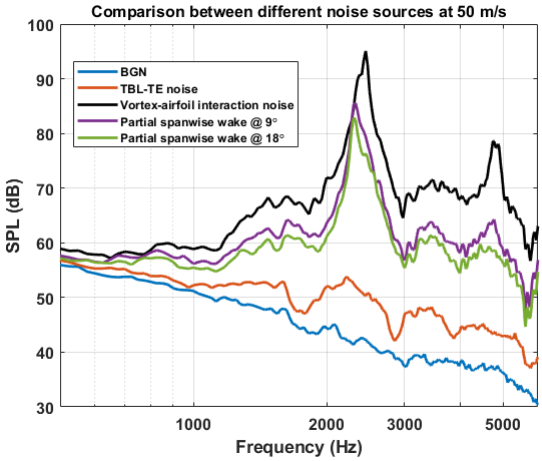

Figure 4.14: Comparison of different noise sources

The comparison between noise sources measured from this experiment is plotted in figure 4.14. As observed from the figure, the vortex - airfoil interaction noise seemed to dominate the airfoil self-noise, as expected. Complete span-wise impingement (default configuration) dominated the partial span-wise wake impingement, and there was a reduction in amplitude, with reducing vortex angle with respect to the airfoil span.

The main take-away from this experiment was that, partial span-wise wake impingement noise dominated the airfoil self-noise, which could be a vital result to be used in RLC configuration.

4.2. RLC configuration

The second experimental campaign was performed on the configuration consisting of the linear cascade of blades. As mentioned earlier, there were two configurations of microphones for this setup, two far-field directivity arcs containing 7 LinearX microphones in total, and a recessed beamforming array consisting of 16 Sonion microphones with a reference LinearX microphone facing the pressure side of the cascade, present on the test section wall, upstream of the cascade blades. Additionally, flow-field measurement using Hot-Wire Anemoemtry was done to analyse the flow statistics in free-stream and the uniformity in flow by measuring at the exit plane and also the wake characteristics at the leading edge of the cascade blades when the rod is in an angled configuration.

4.2.1. Test-section characterization

The first experiment is the characterization of test section using HWA. The rate at which heat is removed from the sensor is directly related to the temperature difference between the wire and the surroundings and the velocity of the fluid flowing over the sensor. This is the working principle of a hot-wire anemometer. Hot wire measurements were performed in the free-stream, to analyse the inflow turbulence and at the exit plane, to check for uniformity in the flow-field. There were two filaments used, one for measuring in the upstream, and one for measuring the velocity statistics in the test section outlet and the wake impingement region at the location of cascade blade leading edge. Calibration procedure of both the filaments was the same, and the procedure is detailed in brief as follows.

1. Calibration consisted of measuring voltage as a function of velocity across the wheatstone bridge, starting with a dry run and proceeding with optimized velocity steps

2. The first step was the calculation of operating resistance of the bridge, given as $R_{oper} = R_{probe} + \alpha(R_{20}(T_{sensor} - T_0))$, where R_{oper} is the operating resistance, α is the temperature coefficient of resistance of tungsten, which is 0.0036 /°C, R_{20} is the sensor resistance at 20 °. T_{sensor} is set at 230 ° and T_0 is ambient temperature

3. A shorting probe was used to calculate the cable resistance

4. The filament was inserted and probe resistance was measured

5. The operating resistance was calculated according to the formula prescribed above

6. The wind tunnel was turned on, and 17 data points were acquired at different velocities, starting from 0 to 55 m/s

7. The coefficients of a fourth order polynomial were obtained by an in-built LABView code and these coefficients enable the conversion from voltage to velocity ($U \propto E^4$, from King's law)

Once the conversion was done, the next step was to perform analysis on the signal to detect outliers. Outliers are a major source of error since they lead to an overestimation of the fluctuations. They are unrealistic and tend to skew the mean and rms results to higher values. Considering a Gaussian distribution, 99.9% of the data lies in the range $[U_{mean} - 3\sigma, U_{mean} + 3\sigma]$, where '$\sigma$' is the standard deviation of the dataset. All values outside this range were considered outliers and removed from the dataset to be processed. This is shown in figures 4.15a and 4.15b.

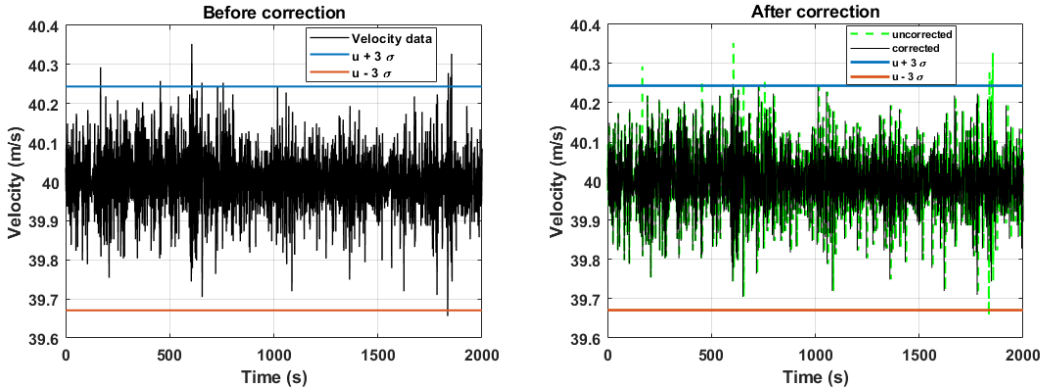

(a) Outliers

(b) Uncorrected vs corrected velocity data

Figure 4.15: Outlier detection and removal

After removing the outliers, the turbulence in the freestream was calculated. The formula for turbulence intensity, I_t, is given as the ratio of velocity fluctuations, u', to the mean-flow velocity U,

$$I_t = \frac{u'}{U}$$

I_t less that 1% is usually considered to be a low-turbulence freestream. By measuring the clean flow using hot-wire, the turbulence in the freestream was calculated to be 0.23%. The uncertainty of mean is prescribed by the formula,

$$U = k\frac{\sigma_u}{\sqrt{N}}$$

where U is the uncertainty, k is the coverage factor which is related to the confidence level and to the distribution of samples. For our case, k was considered to be 3, which corresponds to 99% confidence level. Upon calculation, uncertainty in the mean was found to be less than 1%, meaning, the measurements taken were with good accuracy.

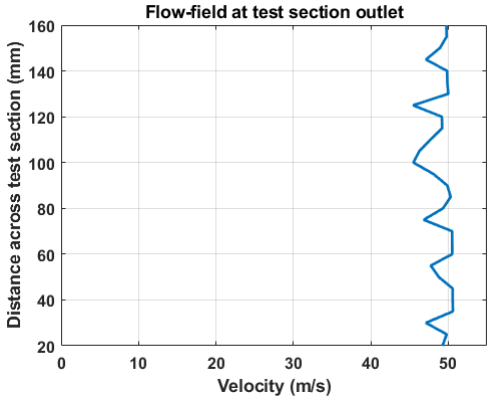

Figure 4.16: Mean flow velocity at test section outlet

To measure the uniformity in the flow-field, the hot-wire was traversed along the width of the test section exit along the mid-plane, thereby measuring the velocity statistics. This was done at 10D distance away from the exit plane. The mean flow velocity along the test section exit is shown in figure 4.16.

Notable from the figure 4.16 is the increase in mean flow velocity which can be attributed to the reduction in the contraction of the test section beyond the cascade blades. Due to cascade stagger angle setting, the test section downstream of cascade is narrower by 30%. For an inflow velocity of 40 m/s, the mean velocity at exit was found to be 50 m/s, corresponding to increase by 20%. The flow-field was observed to be uniform at the exit, i.e., the flow turning was made uniform, even when operating at an off-design condition. Also noticeable was the reduction in the mean velocities, which were attributed to the cascade blade wakes.

4.2.2. Attenuation of metallic mesh

The RLC configuration consists of a recessed microphone array covered by metallic mesh which prevents the flow from entering the recession, thereby keeping the microphones away from the influence of flow. They also have an advantage of being transparent to acoustic waves, but the frequency range might vary with experiments, and should be tested in-situ. Hence it was important to estimate the frequency range where the metallic mesh was transparent to acoustic waves. The reference LinearX microphone placed inside the test section was used for this purpose. The microphone was placed a few centimetres from the source and the measurement was taken without the mesh. The second measurement involved installing the mesh over the baffle and performing the measurement again.

From the results shown in figures 4.17a and 4.17b, the maximum frequency limit which can be trusted was found to be 4500 Hz. Hence for all further results involving the recessed microphone array, the upper bound of frequency is 4500 Hz.

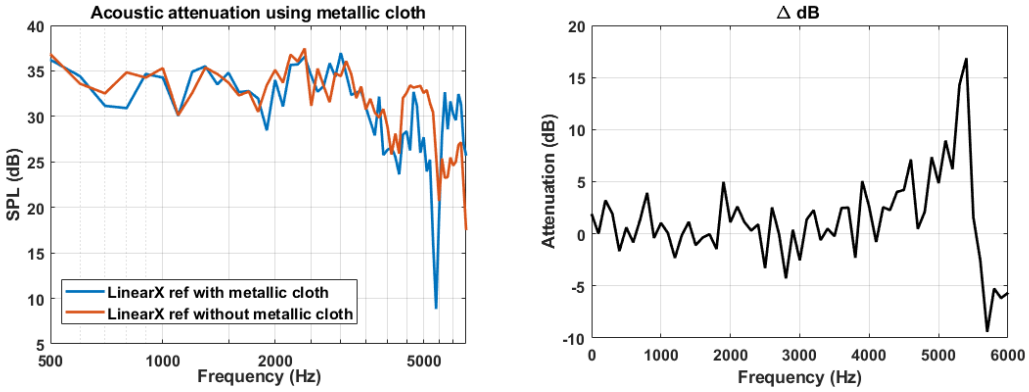

(a) Comparison with and without metallic mesh (b) Attenuation in dB

Figure 4.17: Acoustic characteristics of metallic mesh

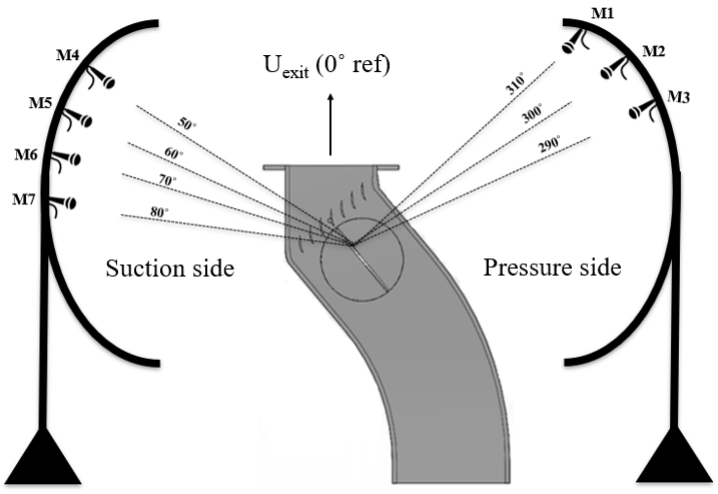

Figure 4.18: Far-field microphone placement

LinearX microphones were used in the external arc for measuring noise in the far-field. They were 7 in number and their placement is shown in figure 4.18. As mentioned in the RSA configuration, pistonphone calibration was done to obtain the sensitivity factors. It was important to mention that any result relating to the far-field spectra are the averaged levels between microphones on the arc, unless stated otherwise.

4.2.3. Beamforming

Beamforming is a signal processing technique used to isolate sound sources of interest from a particular region. Beamforming was performed in this experiment for the sole purpose of obtaining a higher SNR, by isolating the flow self-noise and reflections arising from the test section. A scan plane is usually defined which encompasses the source, and the array plane, where the microphone array is present. A Conventional Frequency Domain Beamforming (CFDBF) is used for evaluation of SPL values of all noise sources. Beamforming was performed on multiple horizontal scan planes having different distances from the array. This is shown in figure 4.19.

Each scan plane was divided into grid points where the SPL values were estimated. The result plane (source plane) was the plane of interest, which was taken at the leading edge of all cascade blades. Beamforming requires the evaluation of the Cross Spectral Matrix (CSM) and the steering vector, which includes the Green's function (transfer function). The CSM is (N× N× f) where f is the number of frequencies and N is the number of microphones. CSM is defined as C = <$\mathbf{pp}^*$>, and is conjugate symmetric and positive semi-definite. $\mathbf{p}$ and $\mathbf{p}^*$ are the fourier transformed pressure and its complex conjugate. For each frequency, an N× N matrix is obtained.

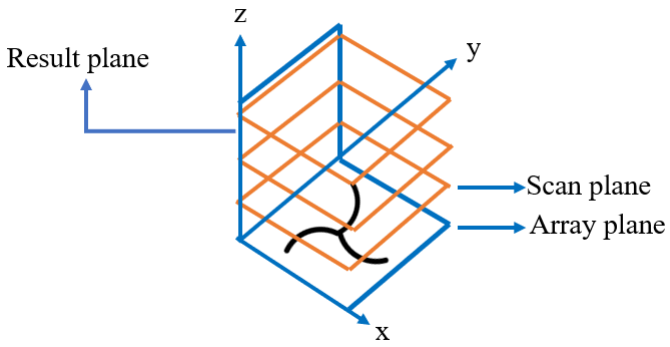

Figure 4.19: Scan plane definition of the beamformer

The CSM was obtained as follows:

1. The time domain pressure signal per microphone was split into various snapshots (segments), and a hanning window was applied to each snapshot. The frequency resolution depends on the window (snapshot) size and was adjusted such that the resolution obtained was 25 Hz

2. Fast Fourier Transform (FFT) was performed on all the snapshots on all the microphones. A single CSM was obtained from a single snapshot

3. The CSMs thus obtained were finally averaged to obtain a single CSM

The main diagonal of the CSM consists of the autospectra measured by the same microphones and the off-diagonal elements consists of cross-spectra measured by every pair of microphones. The incoherent noise sources add to the main diagonal elements, hence the main diagonal was removed from the CSM. The sound powers were obtained by minimizing the difference between the recorded pressures (obtained from CSM)and the modelled pressures at that particular grid point, giving the form

$$\mathrm{A} = w_j^* \mathrm{C} w_j$$

where C is the CSM, and w_j is the weighted steering vector. The steering vector was chosen in such a way to obtain the correct source location, meaning, the beamformer provides maximum output power when the assumed and the actual source position are the same, but with a slight (but constant) offset of actual source strength. This was the best formulation of a steering vector for 3-D beamforming, as shown by Sarradj [47]. The formulation was given as

$$w_{j,n} = \frac{1}{\mathrm{r_{t,j}}\sqrt{\mathrm{N}\sum_{\mathrm{n=1}}^{\mathrm{N}}(1/\mathrm{r_{t,j}^2})}} \mathrm{e}^{-\mathrm{ik}(\mathrm{r_{t,j}}-\mathrm{r_{t,0}})}$$

where $r_{t,j}$ represents the distance from the assumed source location at a grid point to a microphone location, N represents the microphones and $r_{t,0}$ represents the distance of the assumed source location to a microphone location.

The result of the minimization is the source power at the grid points per frequency. The final step lies in extracting the maximum SPL values at the plane dotting the leading edges of the cascade blades per frequency, which gives the final power spectra at the result plane.

4.2.4. Background noise

Measurement for background noise was done without the presence of the cascade blades or the rod. The recessed microphone array was present with the flush-mounted, reference microphone along with it. The SPL values were obtained using a hanning window with a frequency resolution of 25 Hz. The measured sound pressure levels are plotted in the figures 4.20a and 4.20b.

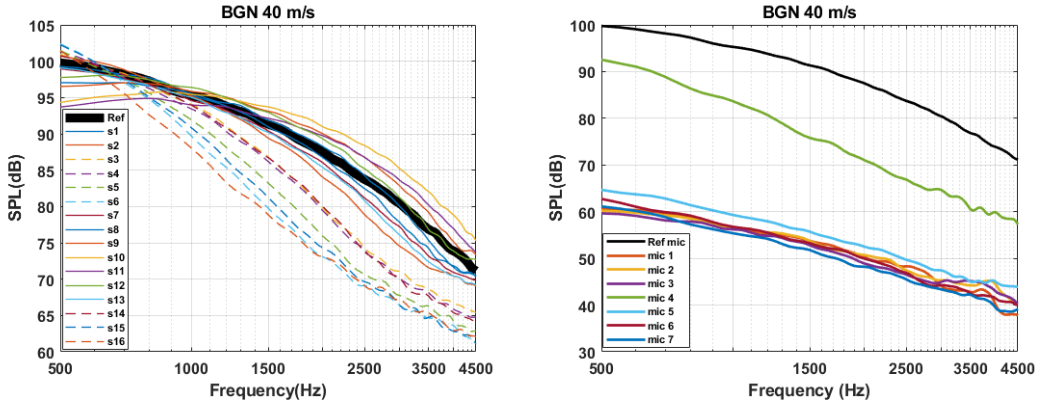

(a) Reference microphone vs recessed microphones (b) Reference microphone vs far-field microphones

Figure 4.20: BGN measurement at 40 m/s comparing the sound levels

It was interesting to note from the figure 4.20a that the flush mounted reference microphone and a majortiy of the recessed microphones were on the same levels. This could be attributed to the placement of microphomes compared to the boundary layer, which is slightly more than 10 mm thick and the microphones being placed at a recession depth of 10 mm. Hence the microphones could still be measuring the boundary layer pressure fluctuations. The metallic mesh and the recession were supposed to cause a decay in the TBL pressure fluctuations, atleast theoretically. According to Jaeger [48], the turbulent flow over an array surface imparts an evanescent pressure wave that decays exponentially over the space between the surface and the microphone, and the decay is given by the formula,

$$20\log_{10}(\Delta p'_{BL}) = -4.3\frac{4\pi f y}{U_c}$$

where y is the recession depth and U_c, the flow speed. The signals decay faster with frequency as microphones are separated from the TBL. But this is just an ideal theoretical scenario, as the boundary layer thickness will cause the actual decay to be less. There was no study relating the boundary layer thickness and the recession depth, as far as the author's knowledge concerns. The microphones which measured significantly lower levels than the reference microphone were located close to the curvature, immediately downstream of the microphone array. The curvature was designed such that the flow turned smoothly only in the presence of the cascade blades. Hence, the interaction of the flow with the wall curvature was believed to be affecting the values perceived by the microphones located close to it. This would also mean that the recessed microphones were in the near-field, for the BGN measurement. From figure 4.20b, microphone 4 from the far-field directivity arc seemed to be in the vicinity of the flow, which was attributed to the absence of blades. An important observation to be made is that, the microphones in the directivity arc were in the far-field when compared to the reference microphone (since the hydrodynamic fluctuations were higher than the acoustic fluctuations by a factor of 1000 approximately, corresponding to 30 dB).

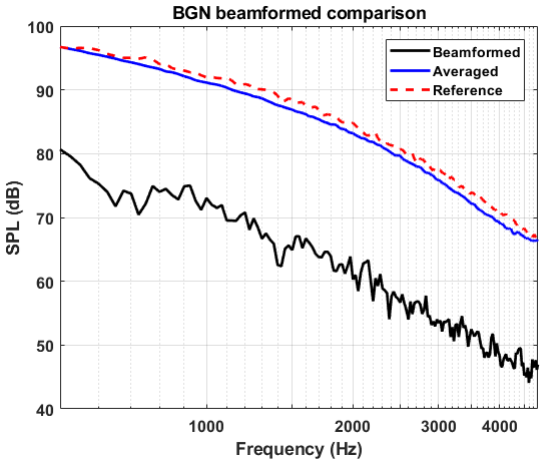

Figure 4.21: BGN, before and after beamforming at 40 m/s

Beamformed BGN levels are plotted as shown in figure 4.21. Beamforming to extract the results at the resultant plane helps in isolating the reflections thereby improving the SNR (Signal to Noise Ratio). As observed, a reduction in amplification of sound in all frequency ranges of interest was seen, with the levels being 20 dB.

4.2.5. Cascade self-noise

The first major result in the RLC configuration concerns the cascade self-noise. The beamformed results are first plotted, and a comparison with BGN levels is done. The far-field spectra are also compared with the absolute BGN levels. The directivity of this noise as extracted from the far-field arc is shown and discussed.

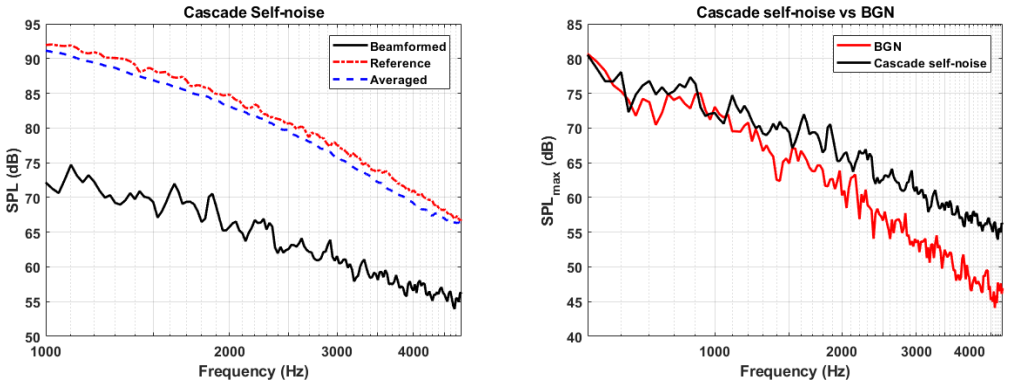

(a) Cascade self-noise comparison

(b) Cascade self-noise vs BGN

Figure 4.22: Cascade self-noise, beamformed data at 40 m/s

At 40 m/s, the the comparison of levels of the beamformed data with the averaged microphone data and reference are shown in figure 4.22a. A reduction in the range of 15-20 dB with respect to reference microphone levels was noticeable after beamforming. This was attributed to the reflections and the flow-self noise in the test section, which the beamformer was able to isolate. Also, the beamformed cascade noise data are plotted alongside the BGN as shown in figure 4.22b. The cascade self-noise was observed to dominate the BGN only above 1 kHz. Below that, cascade self-noise was measured to be on similar levels as the flow self-noise.

The cascade noise propagation downstream (far-field) is shown in figure 4.23 for 40 m/s. BGN seemed to be dominant until 2 kHz, beyond which cascade noise started dominating. But the range of dominance of BGN over the cascade self-noise was observed to increase with an increase in velocity. This trend was also noticeable in the beamformed levels, but at different, lower frequencies (figures show in appendix D).

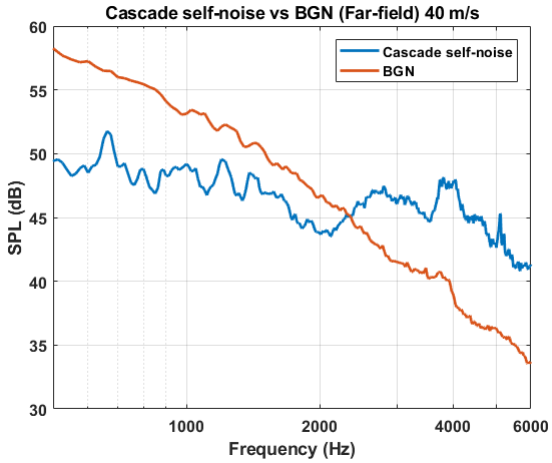

Figure 4.23: Cascade self-noise vs BGN (far-field) at 40 m/s

The BGN levels used as reference here were the averaged levels between microphones which were not under the influence of the flow. It was probably not entirely reliable to use the results from the far-field arc for further analysis of the cascade self-noise results. This was attributed to non-uniformity in flow-field in the test section due to absence of cascade blades due to sharp turning curvature of the test section on the suction side.

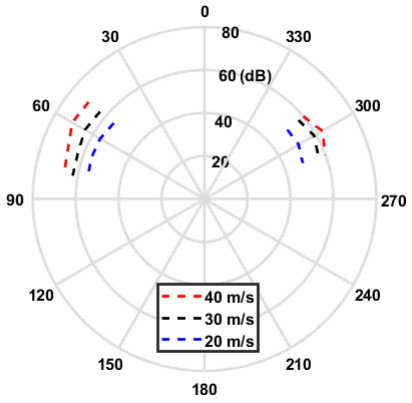

Figure 4.24: Directivity: Cascade self-noise

Nevertheless, the directivity of cascade self-noise source is plotted as shown in figure 4.24. The OSPL integration range was from the frequency where the cascade noise dominated the BGN until 12 kHz.

The Overall Sound Pressure Levels were greater on the suction side compared to pressure side of the cascade (as shown in figure 4.24). Scaling laws for cascade self-noise were not analysed in this thesis owing to the non-trustworthiness of BGN measurement.

4.2.6. RLC default configuration

The next set of results in the experiment concern the rod positioned in its default configuration (placed upstream of the central blade by a distance of 41 mm). This is depicted in figure 4.25.

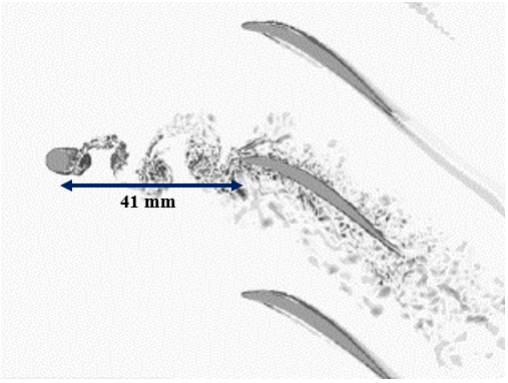

Figure 4.25: RLC default configuration [3]

From literature and from the RSA configuration, it was noted that the rod wake impinging on the leading edge of a blade caused local pressure fluctuations, and since the size of the vortices were smaller than the chord, it led to an edge diffraction phenomenon. But in the presence of the cascade, as in the case of RLC configuration, the acoustic waves produced due to rod wake impinging on the central blade undergo additional diffraction due to the presence of the nearby blades and cause pressure fluctuations throughout the inter-blade channels, whciha re of similar order. The results extracted for this experiment were the beamformed data, upstream of the cascade, and the far-field noise data, downstream of the cascade. Directivity plots and scaling laws were extracted and the results are observed and discussed.

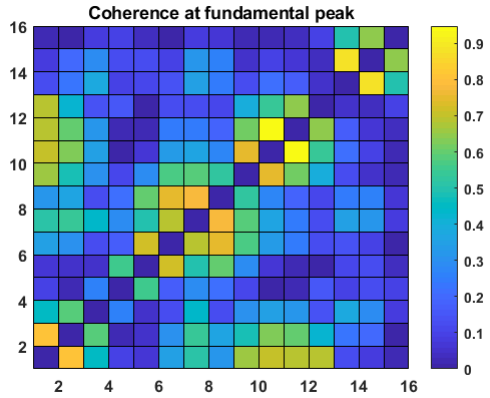

Figure 4.26: Coherence levels at fundamental frequency (2 kHz) at 40 m/s

During experiments, it was noticeable that the tonal noise at the fundamental shedding frequency dominated the spectra and levels measured by the microphones in the test section walls were similar. The acoustic signature at fundamental shedding frequency is a deterministic signal, which would mean that the coherence in the microphone signals are expected to be high (1 represents ideal maxima). Hence a check was done to see what the microphones actually measure. The coherence between microphone signals can be represented as,

$$\gamma^2 = \frac{P_{xy}^2}{P_{xx}P_{yy}}$$

where P_{xy}^2 represents the cross spectra between two different microphones signals; P_{xx}^2 and P_{yy}^2 represent the autospecta of microphones x and y. A CSM was constructed and the diagonal terms were removed. The coherence of the microphones are plotted along with their respective levels for fundamental frequency as shown in figure 4.26. Removing the diagonal terms were performed for obtaining a clearer picture.

At the fundamental shedding frequency, where the tonal noise dominates the microphone self noise, it was seen that there was some coherent behaviour between microphones, hinting at an observation that microphones could already be detecting deterministic signals. But the coherence levels in microphones were not observed to be always high, the microphone signals were clouded with the flow self-noise, which led to

lower coherence values. Hence this validated the usage of a beamforming array to obtain a high SNR inside the test section.

The maximum SPL values per frequency were obtained from the source maps at the source plane, as a result of beamforming. The result plane (source plane) was a vertical plane encompassing the leading edges of the cascade blades. The source map for the fundamental shedding frequency is shown in figure 4.27b. The resultant plane dotting the leading is compared with that of the plane extracted at location of the rod (figure 4.27a). The star represents the true source location, in the source maps which follow henceforth.

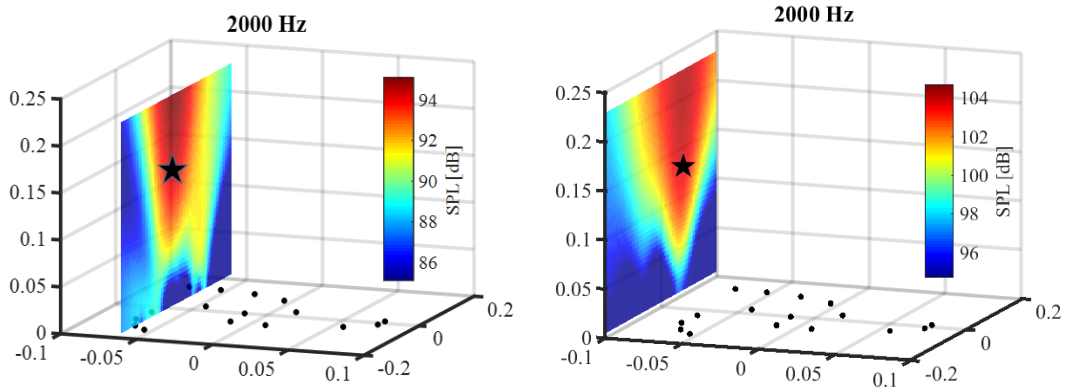

(a) Source map at location of rod

(b) Source map at LE of blades

Figure 4.27: Source maps for RLC default configuration at 2 kHz

From figure 4.27a 4.27b, it was observed that, in the presence of the cascade blades, there was an amplification in the levels of the noise which was caused due to vortex impinging on the leading edge of the wing. The source was seen to be stretched in the vertical direction. This was attributed to the effect of the resolution of the beamformer. The array diameter in the stream-wise direction was lower than that in the span-wise direction. Hence the span-wise resolution was expected to be better (also observed from the figure). Also, the effect of the distance of the source plane from the scan plane is seen to contribute to the decreased resolution (according to Rayleigh's formula [33]), causing the stretching phenomenon mentioned before. But this theory required a validation.

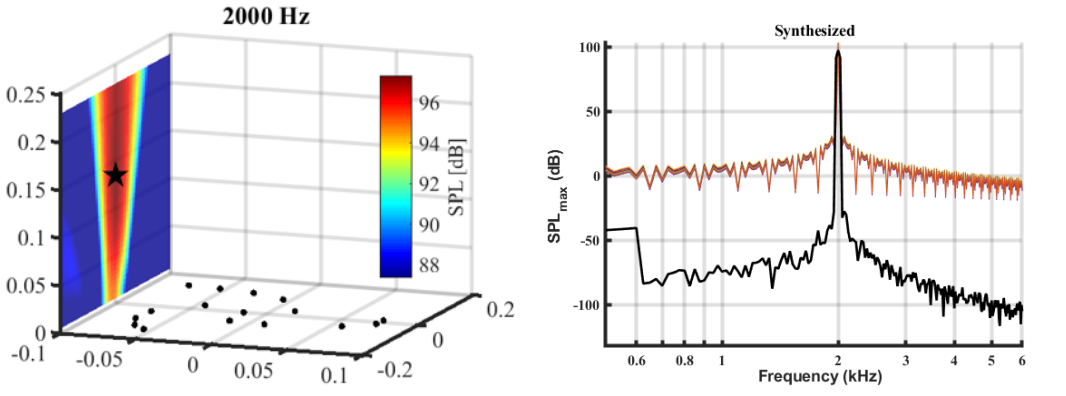

(a) Source map for the synthesized source

(b) Power spectra from the source map

Figure 4.28: Validation of beamforming capabilities using a synthesized source

To validate the beamforming capability at 2 kHz, an analysis with a synthesized data was performed. A point source with a peak of 100 dB at 2kHz was simulated at the location of the central blade (midspan) and the microphone array was steered to see this source. The results are plotted as shown in figures 4.28a and 4.28b

As seen from figure 4.28a, a similar stretching phenomenon was observed, the resolution of the beamformer at low frequency was found to be affected. The source, though placed in the center, was seen to be smeared throughout the vertical plane, the effect increasing with an increase in the distance between source plane and array plane. Figure 4.28b shows that the levels of the actual source was preserved quite well and the beamformer predicted 97.4 dB, at 2 kHz. The effect of smearing of the image was attributed to the non-uniform array diameter, which affected the resolution in turn. Hence, the beamformer predictions regarding the RLC default configuration (smearing of the source location) was expected.

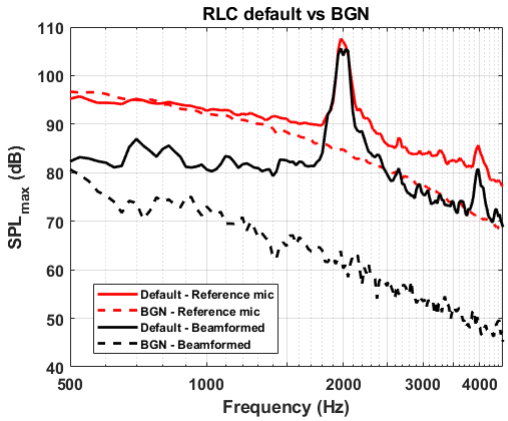

Figure 4.29: Capability of beamforming array in predicting the vortex- cascade interaction noise

The beamformed results along with the levels from the reference microphone are plotted in figure 4.29. It was seen that the vortex-cascade interaction noise was not entirely dominant over the BGN in the given frequency range of interest for the reference microphone. At lower frequencies, the flow self-noise seemed to be on similar levels as the broadband content of the default configuration. But as the frequency increased, above 1500 Hz, the levels of the default configuration seemed to dominate the flow self-noise, as measured by the reference microphone. Beamforming seemed to help in accounting for the reflections and isolation of flow noise in the test section, when the scan plane was chosen to be the leading edges of all the blades. At higher frequencies, the flow-self noise was not dominant over the vortex-cascade interaction noise. But a reduction in the levels of the default beamformed case was still observed, and was attributed to the reflections which are isolated by the beamformer. The levels of isolation were different for the broadband and the tonal peaks, as observed from the figure. This could be because the intensity of the tonal peaks were higher than the broadband, and with an increase in frequency, the damping rate of the reflections from the tonal peaks were lower compared to the broadband, less intense noise.

A comparison was done, where the beamformed data was extrapolated to 1 m and compared with the averaged levels measured by the microphones of the far-field directivity arc. It was observed from figure 4.30a, that the beamforming array was in the far-field for the frequency range of interest. This was important, since the placement of the microphones from the noise source (central blade leading edge) was less than 1 wavelength distance away at the fundamental shedding frequency. Also noticeable were the higher levels in the extrapolated beamformed data at Strouhal numbers lower than 0.18. This was attributable to a combined effect of the presence of cascade blades and the beamformer performance at low frequency.

To bolster this analysis, a comparison of the beamformed data with rod-alone configuration was brought about, the source plot and the spectra of which are shown in Appendix -D. It was seen that the levels of the default configuration were amplified at a frequency less than 1.8 kHz, when compared to the rod alone configuration, where the spectra merged with the background noise. Further analysis into the source maps showed that, in the frequencies lower than 1800 Hz, there were higher levels predicted in the regions where the source was not expected to be present.

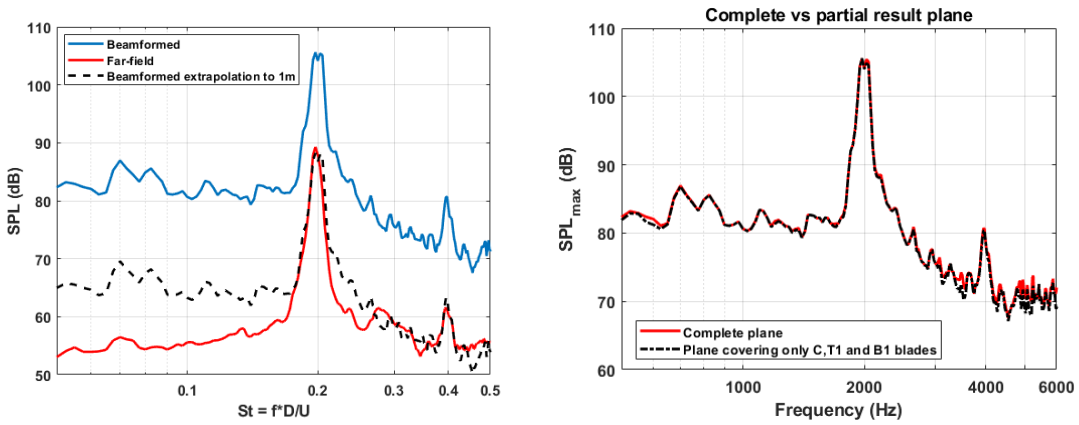

(a) RLC default near-field far-field comparison

(b) Result plane comparison

Figure 4.30: Comparisons in RLC default configuaration

Also, this phenomenon was observed only in the presence of cascade blades. Since the beamforming methodology used here was to extract the maximum SPL from the source plane, we were seeing spurious sources, which the beamformer was not able to isolate. This placed a lower limit on the frequency range which could be trusted for the configuration containing the cascade blades, the frequency being 1800 Hz. The spurious levels at frequencies lower than 1800 Hz are shown in Appendix-D. Nevertheless, the beamformer was seen to have the ability to quantify the propagation of noise from the cascade in the upstream direction, quite accurately.

To zero-in on the actual location of noise in the configuration, the domain of the result plane was reduced to include only the region encompassing C, T1 and B1 blades and the results were compared with the result plane which contains all blades. This is depicted in figure 4.30b. It was observed that the total noise from the result plane was indeed due to the acoustic waves diffracting from the central, T1 and B1 blades as observed in simulation [3].

The directionality of noise and the scaling law in this configuration are shown in figures 4.31 and 4.32.

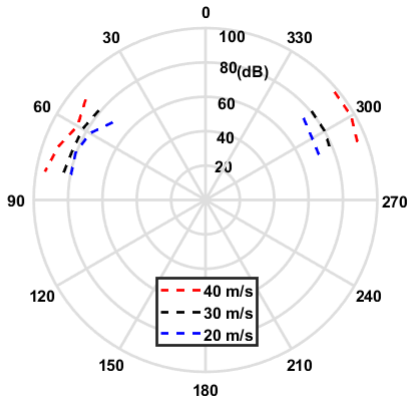

Figure 4.31: Directivity: RLC default configuation

OSPL was again obtained in the Strouhal range comprising of the fundamental, the first harmonic and the intermediate broadband levels. Immediately observable was the non-uniformity in the directionality. The suction side at 40 m/s showed an increase in levels as the microphone placement got perpendicular to the cascade blades (mic 6,7, near 90 °). This could be because of the lower shielding of the noise where the directivity is expected to be the maximum, due to the absence of the side wall, as mentioned in the initial sections.

The vortex-airfoil interaction in the presence of cascade hence scaled as U^6. As mentioned initially, this was an expected scaling due to the pressure fluctuations occurring due to the diffraction of the acoustic waves

emanating from the LE of the central blade, which are of the same order throughout the surface of the wing, hence radiating as a dipole.

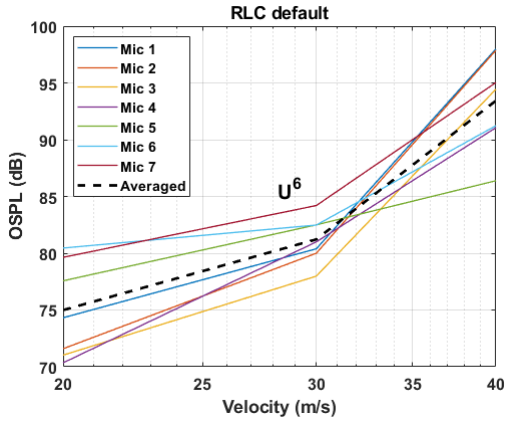

Figure 4.32: Scaling law for RLC default configuation

Finally, a comparison between RSA and RLC configuration in the far-field is brought about in figure 4.33. The fundamental peak due to the quasi-periodic nature of the rod wake was observed to be on similar levels. Apart from the fundamental peak, the RLC seemed to relatively silent, compared to RSA configuration. One important thing to note was that the control variables in both the experiments were not the same. Experiments on RSA configuration were performed in open test section, whereas RLC was performed on a closed test section, so attribution of the difference in levels to a single phenomenon was not possible. One possible reason for the lower levels was that, at higher harmonics (higher frequencies), diffraction became less effective.

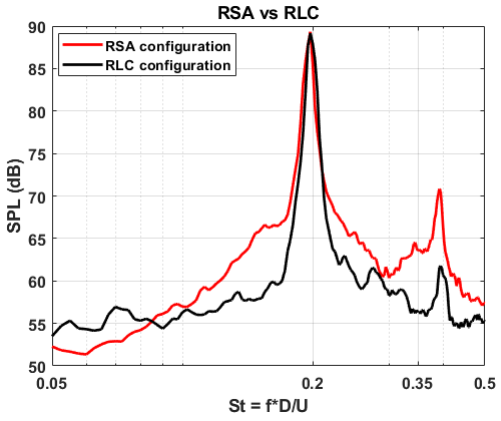

Figure 4.33: RSA vs RLC

4.2.7. RLC default-upstream and angled configuration

Following the results from the default configuration, the rod was translated further upstream, (100 mm from the central blade leading edge) and the acoustic results in this section comprise of the results taken at this particular stream-wise location of the rod. Two experiments were performed in this stream-wise location. The first one was where the rod was not tilted and is denoted the default - upstream configuration. The second configuration was when the rod was inclined in the wall-normal direction to achieve partial span-wise wake impingement on 5 blades and was denoted the default - angled configuration. This experiment was performed in an attempt to achieve impingement on maximum number of blades possible and compare it with the default configuration.

The source levels for the default upstream and angled configurations are prescribed in figures 4.34a and 4.34b. The maximum source levels for both these configurations seemed to be on a similar scale, at first instance. A deeper look into the spectra would provide valuable information. The beamformed results were

plotted along with the BGN. Upon translation of rod in the stream-wise direction, it was seen that the strength of the vortex interacting with the central blade leading edge was low compared to when the rod is placed 41 mm upstream, but this interaction noise was still dominant over the BGN (shown in figure 4.35).

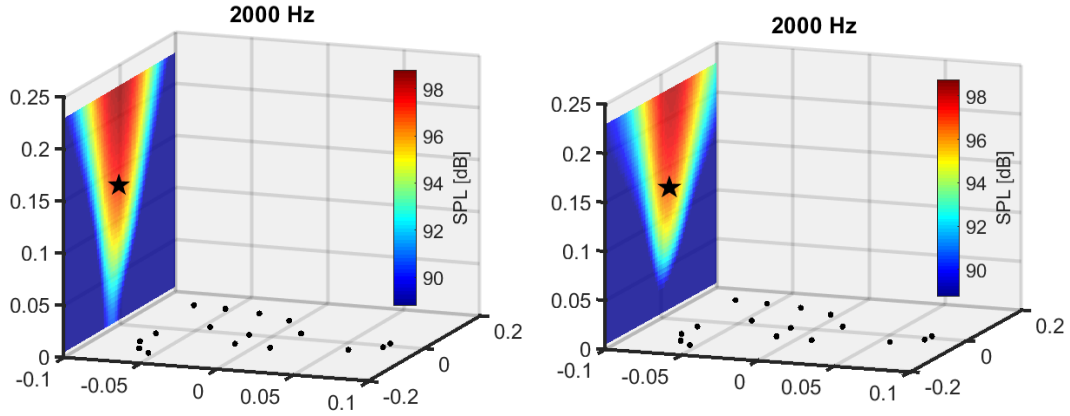

(a) Source map - default upstream

(b) Source map - angled configuration

Figure 4.34: Source maps for upstream configurations

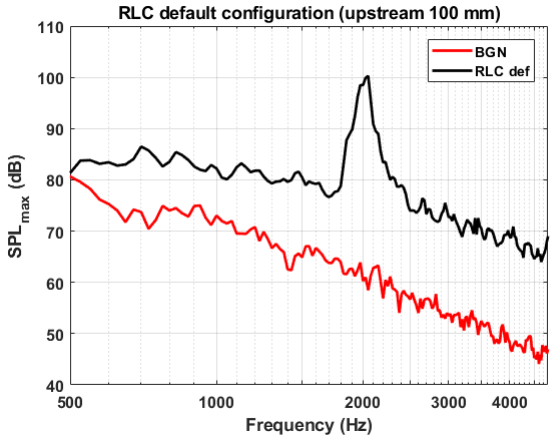

Figure 4.35: Default RLC-upstream configuration vs BGN (Beamformed)

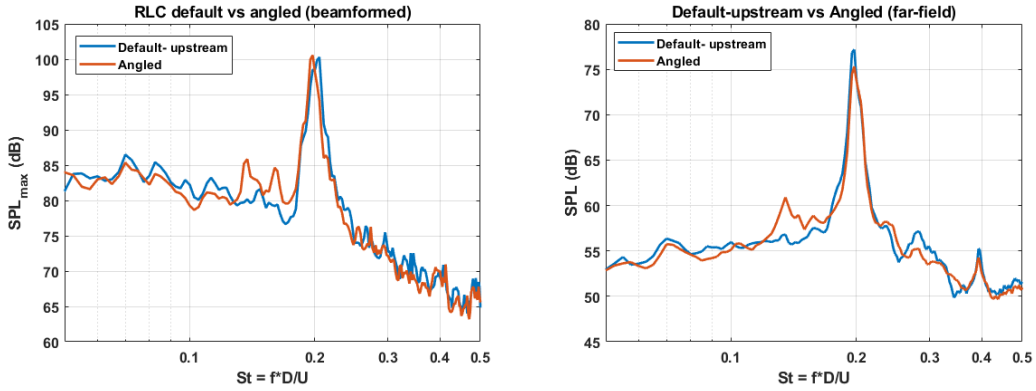

(a) Default upstream vs angled, beamformed

(b) Default upstream vs angled, far-field

Figure 4.36: RLC default upstream vs Angled configuration comparison of max SPL (dB)

The beamformed results of the rod in an angled condition is depicted in figure 4.36a. This was compared to the rod in the default condition, upstream. It was interesting to note that the levels at fundamental shedding frequency, as well as broadband levels in both the cases matched. A similar plot was obtained in the far-field, comparing the levels of the default and the angled case, and is shown in figure 4.36b. It was observed that the they indeed were on similar levels, the difference with the angled configuration at the peaks being less than 2 dB. A suitable explanation for this could be given from the analysis of hot-wire measurements performed with the angled rod configuration without any cascade blade in the test section. The leading edge location of the blades were simulated and velocity statistics were obtained. This is plotted in figure 4.37a.

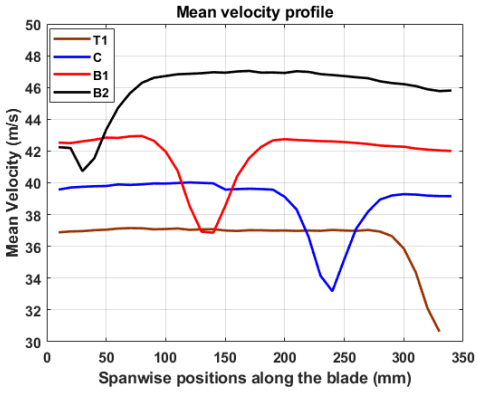

(a) Hot-wire measurements at LE of blades

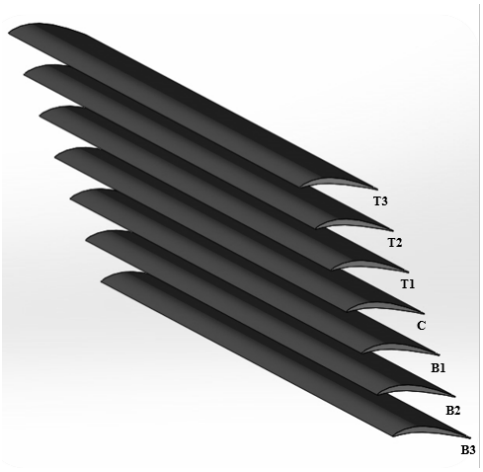

(b) Cascade blade nomenclature

Figure 4.37: Hot-wire measurements at leading edges of cascade blades

The first observation was the difference in the mean flow velocity at the simulated leading edges of the blades. The side-wall used for this experiment was not cut-off (unlike the configuration of the wall with the microphone array), thus enabling a uniform exit plane. This configuration would thus allow smooth turning only in the presence of the cascade blades. Nevertheless, it was observed that, at the central blade location (C, in figure 4.37b), the mean flow speed was measured to be 40 m/s. The second and most relevant observation here was the span-wise extent of the wake on the leading edges of the blades. In the few blades sampled in the experiment, regardless of the mean flow velocity, the spanwise wake impingement location spanned around 100 mm, per blade. This roughly translated to 500 mm, if all 5 blades were impinged partially (100 mm) by the angled rod. The span-wise correlation length of the wake, as measured from simulations [3], for the rod placed 41 mm in-front of the central blade LE was found to be 3.64 mm, for a 5.2 mm rod diameter. The correlation length decreases as the wake expands, hence when the rod is placed further upstream, it can be considered that the correlation length is too small to be of significance, i.e., the sources are uncorrelated and add up linearly. Hence both the noise sources effectively correspond to similar sound pressure levels.

The directivity plots for the default- upstream configuration and the angled configuration are represented in figures 4.38 and 4.39 and were observed to be similar. This observation bolstered the fact that, though the manner of noise production mechanism was different (the wake was angled in one case), the radiation to the far-field was only dependent on the nature of the source, here, a rod wake diffracting from the leading edge.

The scaling laws were yet again obtained in a similar fashion as before. The method of extracting the scaling law, which was used for the RLC configuration, was validated in this section. The default-upstream case, where the rod is placed 100 mm upstream, had the same noise production mechanism as when the rod is placed 41 mm in-front of the central blade leading edge. Thus, the scaling law in both the cases must be the same, if the methodology utilised in obtaining them were correct, which was also seen, as shown in figure 4.40a. Hence, the vortex-airfoil interaction, in the case of rod translated upstream, also scaled as U^6.

Similarly, the scaling law obtained for angled rod configuration is plotted in figure 4.40b.

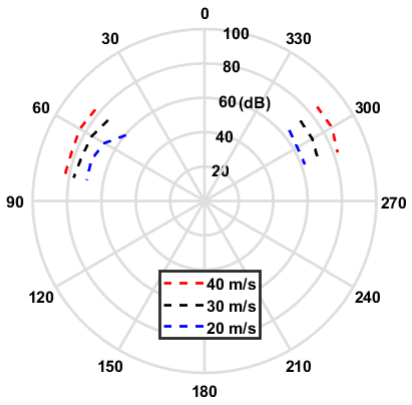

Figure 4.38: Directivity: RLC default- upstream

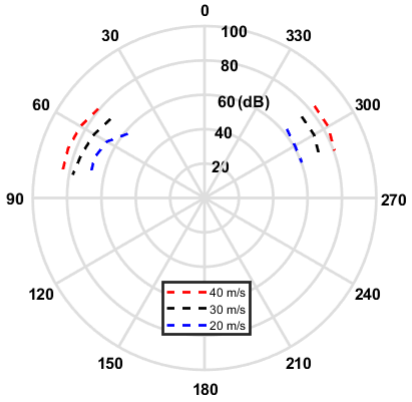

Figure 4.39: Directivity: RLC angled

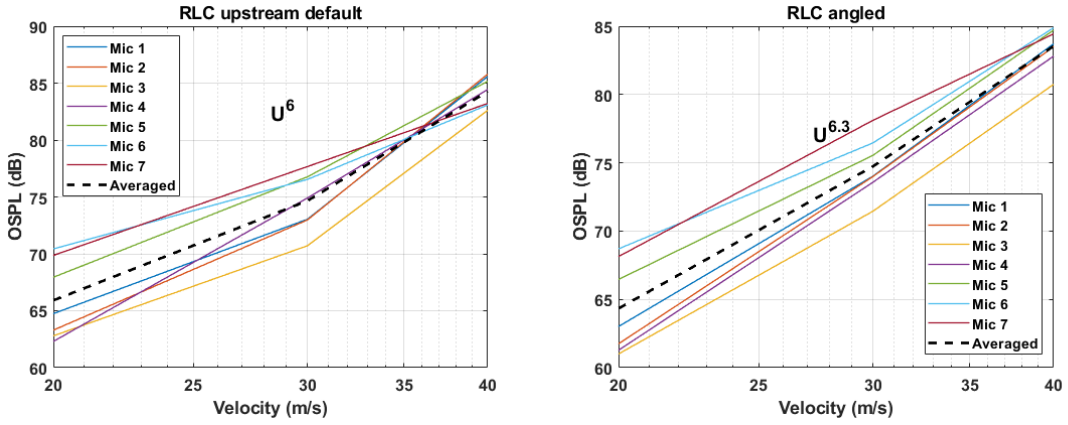

(a) Scaling law for RLC default-upstream configuration (b) Scaling law for RLC angled configuration

Figure 4.40: Scaling law analysis

The vortex-leading edge interaction noise in the angled rod configuration scaled as $U^{6.3}$, similar to the default-upstream configuration.

4.2.8. Overall comparison between different noise sources

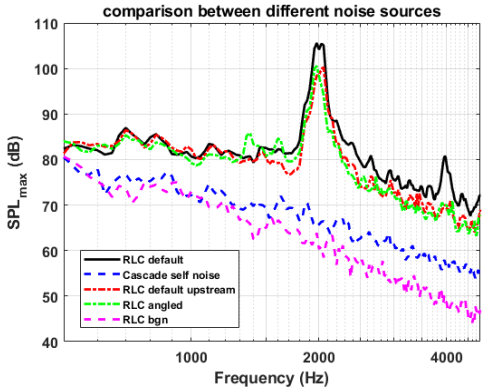

(a) Comparison between all noise sources, beamformed

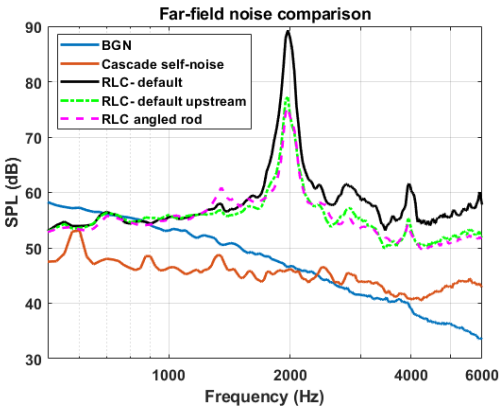

(b) Default upstream vs angled, averaged and in far-field

Figure 4.41: Comparison between all noise sources, far-field

The overall beamformed results are plotted as shown in figure 4.41a. As expected, vortex-airfoil interaction noise was the most dominant upstream, and the cascade self-noise propagation upstream was seen to be dominant over the BGN only beyond 1500-2000 Hz and this dominance was not seen at the same frequency from the far-field results. Beamforming on the small array in the test section did help in improving the SNR, by isolating the flow noise and accounting for the reflections. As far as the far-field measurements were concerned, the trend observed was similar, apart from the BGN. The BGN measurements, as mentioned before, were not to be trusted entirely owing the irregular turning of the test section without the cascade blades.

5

Conclusions and Recommendations

5.1. Conclusions

The conclusions from the results can be broadly divided into two, one, pertaining to the RSA configuration and two, which concerns the RLC configuration.

Experiments were performed on the RSA configuration to analyse the various noise sources and predict their dominance. These experiments were done on a wing with NACA 5406 profile, which mimics the mean aerodynamic loading of the central blade of RLC configuration. The notion behind was that, if the aerodynamic phenomenon which causes the LE noise were preserved, isolation of OGV blades could be made possible to study its individual characteristics. Concluding remarks from the results of this configuration are given as follows:

- Scaling laws were obtained by a method of averaging the OSPL obtained from the microphones, which were validated by measuring the deviations in the microphone levels, per velocity
- Airfoil self-noise for the current experiment was concluded to scale with $U^{5.79}$ and the vortex-leading interaction noise, with $U^{5.11}$ for the fundamental peak, and U^{6}, for the Strouhal range of interest (0.1-0.42)
- An important experiment in this configuration concerned that of partial span-wise wake impingement. From this experiment, it is concluded that indeed, with a reduction in the vortex angle with respect to the span of the blade, there is a reduction in the far-field noise perceived, which is still dominant over the airfoil self-noise
- Scaling laws were calculated for the noise due to partial span-wise wake impingement. The noise scaled as $U^{3.95}$ and $U^{4.02}$ scaling with the fundamental peaks for 9 and 18 ° rod tilt, and as $U^{5.02}$ and $U^{4.89}$ for the Strouhal range under consideration for 9 and 18 ° rod tilt. The reason for this scaling is not yet established, and it is concluded that further analyses need to be done to understand the scaling obtained
- The wing bending problem was analysed using an analytical formulation. Applying the wind tunnel corrections for C_l and correction to the lift measured by the load cells using the analytical formulation, a difference of 6.1% in C_l with X-Foil was obtained

The different noise production mechanisms analysed in the RSA configuration are given in the decreasing order of dominance as:
Vortex-airfoil interaction (Full spanwise wake impingement)> Partial spanwsie wake impingement (9 ° > 18 °)> TBL-TE noise > BGN.

A major portion of the experimental campaign concerned that of the RLC configuration. Experiments performed on RLC configuration included that of the cascade self-noise, vortex-cascade interaction noise and noise due to partial span-wise wake impingement on the cascades with angled rod configuration. Hot-wire measurements done included flow-field characterization of the test section at the exit plane, to check for

uniformity in flow at the leading edges of the cascade blades (without the physical presence of the blades), to measure the span-wise extent of the wake, and in free-stream, to measure the turbulence intensity. The conclusions from the RLC configuration are given as follows:

- The freestream turbulence was calculated to be 0.23%, for the RLC configuration. From the measurements at exit plane, it was found that the cascade blades turn the flow uniformly, even when operating at an off-design condition. The span-wise wake extent of the rod wake on the blade leading edge when the rod is angled was measured to be approximately 100 mm
- The dominance of cascade self-noise over the BGN was found to occur at different frequencies, when measured upstream and downstream, for the same velocity. This difference in frequency was attributed to the non-trustworthiness of BGN from the far-field measurements, at low frequencies. Scaling law was hence not obtained for cascade self-noise in this experiment
- From the beamformed results, it is concluded that the vortex-cascade interaction noise dominates the BGN throughout the frequency range of interest. Reducing the resultant plane to one which consists of C,T1 and B1 blades alone, and comparing with the default plane consisting of all the blades shows same levels throughout the frequency range of interest. Hence the maximum noise production is found to arise from the immediate region surrounding the central blade, which is in line with the findings in simulation [3]
- Comparison of the beamformed data of the default case with the microphone arc in the far-field, downstream, showed that the microphone array is indeed in the far-field, above 1.8 kHz. The amplification in the levels below this frequency was attributed to the detection of spurious sources by the beamformer, at lower frequencies, thereby placing a lower limit on the frequency which can be trusted from the beamformed results, for the measurements of RLC. It can also be inferred, based on the limited knowledge from this experiment, that, the microphone array need not be placed at a distance greater than twice the wavelength (far-field) for them to be in the far-field, for analysing the vortex-cascade interaction noise. From the directivity plots, it was seen that the directivity in the far-field was not uniform, which was attributed to the absence of the side wall, thereby not shielding the noise as it propagated to the far-field. The vortex-cascade interaction noise was found to scale with U^6
- From the comparison of the default RLC configuration with that of RSA, it was concluded that the RLC was relatively silent, except for the fundamental peak, where the levels matched. Diffraction at higher harmonics becoming less effective could be stated as the cause for the lower levels, although a proper explanation for this could not be obtained from this experiment
- The comparison between sound levels of partial span-wise wake impingement and the configuration of complete span-wise wake impingement is done and the sound levels are found to be approximately on the same scale throughout the frequency range of interest. The reason is attributed to the linear addition of uncorrelated sources and the extent of the partial span-wise wake impingement being on the same order as that of the complete span-wise wake impingement.

Looking back at the research goals, it seems that all of them have been addressed on a satisfactory level. The RLC setup was indeed successful in predicting the vortex-cascade interaction noise. The beamforming array was able to improve the SNR throughout the frequency range of interest. The beamforming array was thus able to quantify the upstream propagation, and for the RLC default configuration, the array seemed to be already in the farfield, thereby allowing a direct comparison with the measurements taken from microphones in the directivity arc. The far-field directivity arc manufactured was able to successfully predict the directionality of the noise sources, and scaling laws derived from them were also as expected.

5.2. Recommendations for future work

Recommendations for utilizing this RLC configuration better are crucial for future research. Certain preliminary tests could have been performed, which would have certainly helped in obtaining accurate results, thus bettering the analyses. In this section, certain recommendations are provided, based on the learnings of the experimental campaign, which could help in efficiently obtaining better results in the future. They are enumerated as follows:

1. An important recommendation concerning the RLC configuration is the calibration of the Sonion microphones. They are small, hence the pistonphone, which is designed for microphones with 1/2 or 1/4 inch diameters are not suitable for calibrating the Sonions. A special holder must be designed, which locks into the duct given by the pistonphone on one end, and holds the exposed diaphragm of the Sonion microphone on the other end. This would enable in calibrating the microphones better. An important aspect of frequency calibration of microphones is to have very few or no obstacles to the wave propagation when white noise is being played, i.e., it must be done in the free-field. Calibration with and without the test section flanges must be done. The difference between the two ensures that proper weighting per frequency is obtained for every microphone, thus accounting the installation effects

2. Analysis of the acoustic capabilities of the metallic mesh must be done in-situ. This analysis is important in determining the operating frequency range of the mesh (transparency to acoustic waves). The LinearX microphone which was exposed to white noise from an omni-directional source was not entirely in the free-field. This led to reflections and bizarre response in the presence of the metallic mesh, beyond 5 kHz. A sound alternative to this would be to use a calibrated microphone placed in free-field, and white noise from a speaker be recorded, with and without the metallic mesh installed over the microphone baffle. The difference would validate the transparency of the metallic mesh to the acoustic waves

3. Metallic mesh was used to cover the recession in the RLC configuration because of its ease of installation. From literature, Kevlar is seen to have better attenuation capabilities than the metallic mesh, and the recessions to be covered are also small, hence Kevlar can also be used in comparing the results with the metallic mesh, to choose the best material for this experiment

4. The experiments on the RLC were performed at an off-design condition, at 40 m/s where the whole test-section was designed for 72 m/s. The developing flow-field inside the test section has the potential to separate along the curvature and re-attach. This might cloud the data measured by the recessed microphones, although hot-wire measurements taken at the exit plane show that the flow-field is uniform (atleast starting from the leading edge of the cascade blades). Hot-wire measurements at the test section walls on which the microphones are recessed must be performed for estimating the boundary layer thickness, if future experiments are also to be performed at an off-design condition

5. BGN measurements in the RLC configuration were not straight-forward. The removal of the side walls of the test section exit plane had a sharp turning flange, and from hot-wire measurements, a reduction in velocity (and thereby, an increase in velocity on the other side (conservation of mass)) was observed. The sharp deflection was also seen to affect the low frequency part of the BGN measurement. It is proposed to have the test section wall removed in such a way that there is no sharp contour in the exit plane. It is also desirable, in the future, to have a wall which can be re-attached, since the removal is required only for BGN measurements, so that the test section exit plane is uniform. This would enable better comparisons with cascade self-noise and also give a clearer picture of the directionality of different noise sources, when compared to having a non-uniform test section outlet

6. Acoustic calibration of the test section must be performed and recorded by microphones in the far-field, to understand the effect of the duct and also the obstacles placed in the duct (cascade blades). A simple experimental procedure is proposed as a recommendation. The first step would be to place a speaker playing white noise at the inlet of the empty test section and cover the remaining gap at the inlet with absorbing foam, so that remaining region in the inlet does not become a hard wall. Next step is to place the microphones in the far-field directivity arc at the same location as in the experiments and record white noise emitted from the speaker. The third and the final step is to add the cascade blades inside the test section and play the white noise. This would help in understanding the effect of cascade blade in modifying the acoustic waves in the frequency range of interest

7. Although Rayleigh's criterion wasn't satisfied, the beamforming array was placed to improve SNR. It was seen that, after beamforming, the broadband levels were reduced on an average by 15 dB, attributed to reflections from the walls and flow-self noise, meaning the beamforming array does help in localizing the noise source arising from the region of interest, the cascade leading edges. Nevertheless, a better methodology must be adapted in designing the beamforming array. The first step would be to calculate the boundary layer thickness developing over the surface of the wall to determine the recession height.

It would be better to keep the recession atleast a few boundary layer thickness away from wall, so that the large scale structures contributing to the turbulence (low frequency) decay and are not detected by the microphones. From results of the current beamforming array, it was seen that spatial resolution at lower frequencies were low. This is usually tackled by having a bigger array aperture, but owing to limited spacing in this test section, the number of microphones can be increased in a different fashion. Instead of a multi-spiral array configuration, a logarithmic line array can be swept in an annular fashion (improving the low frequency resolution), thereby increasing the number of overall microphones in the configuration. This would also reduce the spatial aliasing at high frequency, (microphone spacing $< \lambda/2$)

8. To have a direct comparison of the RLC with RSA configuration, it is necessary to keep the control variables consistent. This means that RSA must be performed in a closed test section, like the RLC configuration. Also, the propagation of vortex-leading edge interaction noise occurs in free-field when compared to the RLC, where there are modifications due to the presence of the cascades and the exit walls, before propagating to the far-field. Translating the beamforming array to the wall facing the suction side of the blade in RSA configuration, performing the experiment and comparing would give a clarity in the propagation mechanism in both the configurations

9. From the results of RLC, it was observed that the levels of the angled configuration and default-upstream were similar throughout the frequency range of interest. Also, the slot allowed impingement only on 5 of 7 blades. A modification to the side wall can be made, which allows the rod to be translated to various locations downstream and also achieve partial span-wise wake impingement on all blades. This increases the coherency of the rod wake on the leading edges, and also enabling a better comparison with the partial span-wise wake impingement of the RSA configuration

10. Since RLC is designed to operate at higher velocities, also the regime at which the actual noise mitigation techniques should be concentrated, it is better to perform experiments at velocities greater than 40 m/s. This would also ensure better working capability of the current beamforming array. This is possible in the current upgrade of the wind tunnel which was done as soon as the experimental campaign came to an end. Any discrepancies which could have possibly arise due to the off-design operation would be mitigated this way

Appendix A

Wind tunnel corrections are performed for both the experimental campaigns. For the RSA configuration, both corrections for open jet, and shear layer directivity and amplitude are performed.

An elliptical open jet is considered, which represents the experimental setup [49]. Because of the flow expansion , the effective angle of attack perceived by the wing decreases , which reduces the C_l. The streamline curvature effect for the wing states;

$$\Delta\alpha_{\text{wing}} = \delta \frac{\text{S}_\text{w}}{\text{C}} \text{C}_\text{l}(57.3)$$

$$\Delta\text{C}_\text{l} = -\text{a} \times \Delta\alpha$$

where δ represents the boundary correction factor, S/C represent the ratio of wing to tunnel cross section area and a is the lift curve slope. δ is obtained by knowing the values of λ, which represents the ratio of minor to the major axis of the jet and k, which represents the ratio of span to the major axis (figure 1).

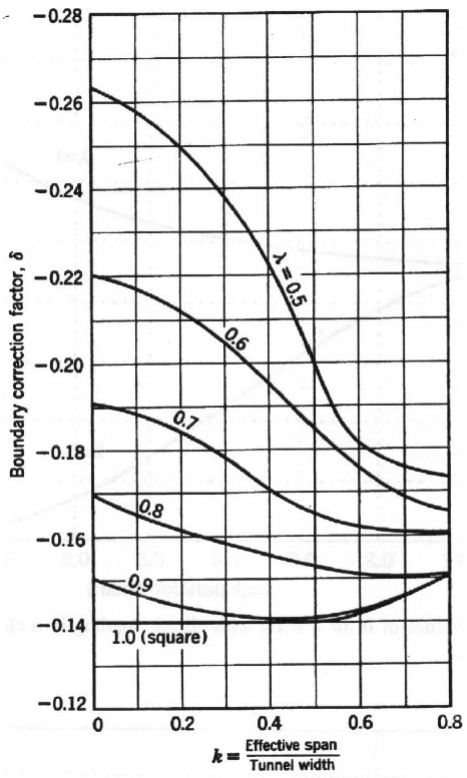

Figure 1: Values of δ for a wing with uniform loading in an open rectangular jet [49]

From the figure, the value of δ obtained was -0.18. By using the formulations prescribed, $\Delta\alpha_{wing}$ is 1.94 ° and ΔC_l was obtained to be 0.15. Hence, a correction factor of 0.15 is added to the obtained C_l.

The shear layer refraction correction for far-field noise is performed, which accounts for the bending of the acoustic waves as they pass through the shear layer to the free-field. This is mentioned here as the correction to be applied for the far-field directivity measurement, both in RSA and RLC configuration. The bending of the waves as they pass through the shear layer modifies the directivity and the amplitude of the noise propagating the far-field. According to Amiet and Schlinker [50][51], the angle correction is independent of

the type of shear layer interface or its thickness, whereas, the amplitude correction is dependent on whether the shear layer is plane or cylindrical, and on the shear layer thickness.

For a plan zero-thickness shear layer, the angle correction is given as

$$\tan\theta_c = \frac{\zeta}{(\beta^2\cos\theta + M)}$$

where,

$$\zeta^2 = (1 - M\cos\theta)^2 - \cos^2\theta, \qquad \beta^2 = 1 - M^2$$

θ_c is the corrected angle and M is the mach number .

the amplitude correction is prescribed as

$$|P_c/P_m| = \frac{1}{2}(1 - M\cos\theta)[(\zeta/\sin\theta) + (1 - M\cos\theta)^2]$$

where P_m represents the measured pressure and P_c represents the corrected pressure.

Based on these calculations, an example of the angle and amplitude correction for the case of TBL-TE noise at 40 m/s in the RSA configuration is given in the table 1

Distance (m)	1	1	1	1	1
θ (degrees)	120	100	80	60	40
θ_c (degrees)	118.18	99.79	79.79	57.91	32.66
$\frac{P_{corr}}{P_{meas}}$	1.13	1.06	0.93	0.76	0.55
Δ OSPL (dB)	-1.03	-0.46	0.6	2.35	2.62

Table 1: Shear layer refraction correction

Appendix B

A few issues with the NACA 5406 wing were faced during the experiment. First, the geometric angle of attack, which was supposed to be at an angle of attack of 8 °, was measured to be at 5.7 °. Secondly, the wing was manufactured using Aluminium, a lightweight alloy. Since it was a slender configuration, the stiffness was very low, leading to bending of the wing, which was noticeable upon visual inspection. Hence, all the acoustic measurements done on the RSA configuration was based on a reduced span (from 400 mm to 250 mm), where the remaining non wetted span was reinforced to avoid bending, which led to an under-prediction in the expected lift.

This underestimation of lift could possibly be attributed to:

1. Wing bending, where only a component of the lift is acting in the direction perpendicular to freestream

2. Spanwise change in geometric angle of attack, which possibly modify the flow-field around the wing, modifying the lift measured

3. Instrumentation error

Accounting for this seemed of top priority, to know how much lift was lost due to bending. A structured approach was followed, where a combination of displacement measurement using laser and analytically formulating the problem to relate the displacement and load were performed to account for bending, the details of which are summarized below.

The first step in the analysis was to experimentally estimate the stiffness of aluminium, 'EI'. A known set of weights are placed on one end of a string suspended on a pulley. the other end is attached to the mid-span of the wing. The schematic is shown in figure 2. This situation mimics that of a simply supported beam, which gives us the formulation of a point load as,

$$\delta = \frac{PL^3}{48EI}$$

where δ is the displacement (in m), P is the point load (in N) and EI is the stiffness of the material of the wing. The displacement upon loading is measured using a laser source, whose error in measurement is ±1 mm. The calibration setup is shown in figure 2

Load (Kg)	Measured load (N)	Measured displacement (δ) (m)	EI (N/m)
1	9.52	3	4.231
1.5	13.82	4	4.606
2	18.46	5	4.922
2.5	23.06	7	4.392

Table 2: Estimation of stiffness, *EI*

Figure 2: Figure showing the setup for estimating *EI*

The laser source (not shown in figure 2, is to the left) is placed at a reference distance. Upon loading, the wing bends, and this distance is recorded by the laser source. The difference between the reference and the recorded distance is δ. The measured displacements and the corresponding loads are tabulated in table 2, and the average EI is estimated to be 4.884 N/m.

The second step in accounting for wing bending is the formulation of an analytical expression, relating the displacement to the load, the lift. This is done by considering a uniformly distributed load over a simply supported beam, where the load distribution is imparted only to the wetted region, 250 mm. This is shown in the figure 3

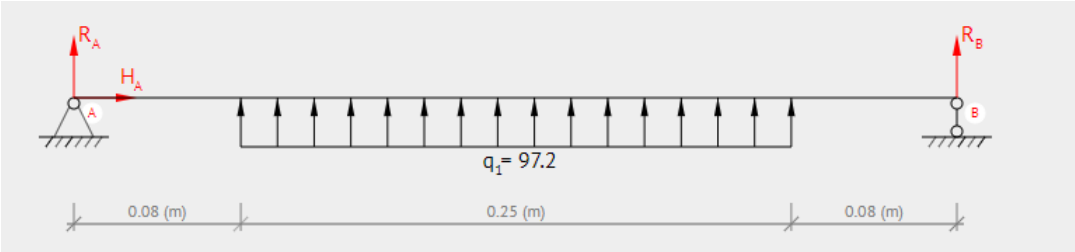

Figure 3: Schematic of the load distribution over the wing

q_1, as shown in figure 3 refers to the UDL, in N/m. According to the second order differential equation for elastic curve of a beam deflection,

$$EI\frac{d^2y}{dx^2} = M$$

where M is the bending moment and y is the deflection of the beam. Solving this equation using boundary conditions which specify that deflection is 0 at both ends, the formulation obtained was

$$P = \frac{EI\delta_{max}}{\left(\frac{bL^3}{16} - \frac{baL^2}{4} - \frac{(bL)^2}{8}\right)}$$

where b is the distance of the beam which is loaded (0.25m in this case), a is the distance which is not loaded (0.08m for this case) and L is the overall length of the beam. A calibration curve was then constructed relating the force measured by the load cell and the force expected from the analytical formulation, where

the input is the δ_{max} measured by the laser cell. The wind tunnel was turned on and the data obtained is tabulated in table 3.

Velocity (m/s)	δ_{max} (mm)	Force (N) from formula	Force (in Kg)	Force (N) measured by load cell
20	1	4.99	0.51	2.25
30	1	4.99	0.51	4.82
40	2	9.98	1.01	8.28
50	3	14.97	1.53	12.82
55	3	14.97	1.53	15.87
58	4	19.95	2.03	17.23

Table 3: Data for constructing the calibration curve

The calibration curve hence constructed is shown in figure 4.

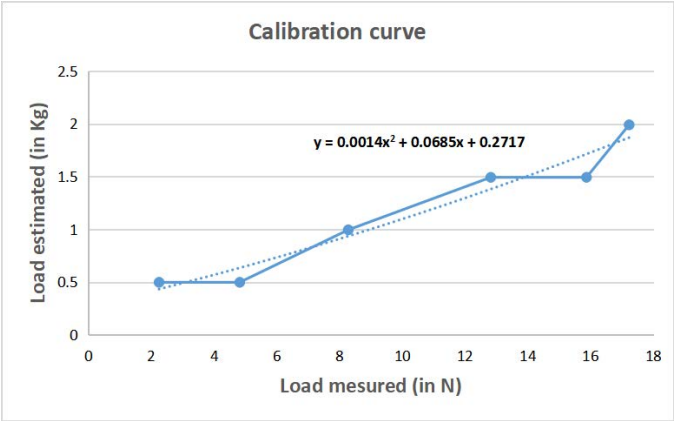

Figure 4: Calibration curve

fitting a polynomial of order 2 gives the equation of the curve as

$$y = 0.0014x^2 + 0.0685x + 0.2717$$

The overall correction = correction to lift measured by load cell using analytical formulation + correction to C_l measured from streamline curvature effect (refer Appendix B). For 40 m/s, the corrected C_l is 1.06 and X-Foil predicted C_l for the same condition is 1.13, which leads to a difference of 6.1 %.

Appendix C

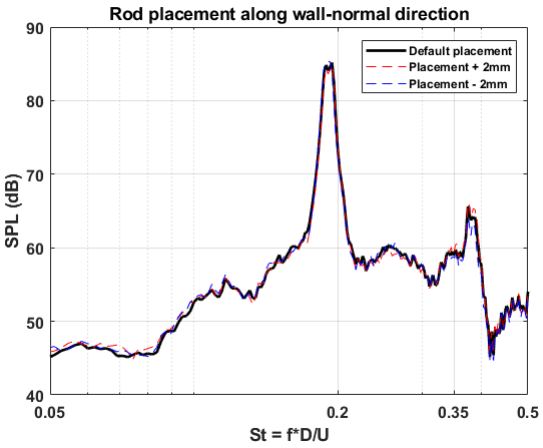

Figure 5: Analysis of rod placement location along wall normal direction of wing

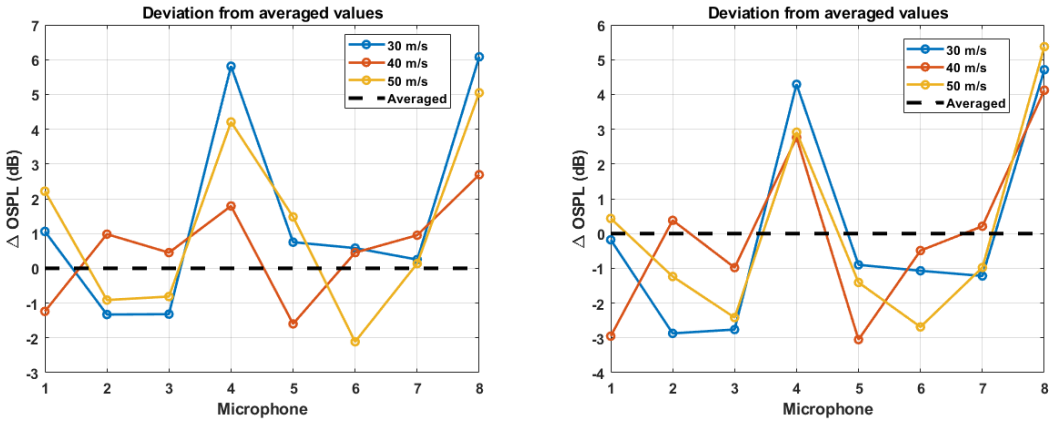

(a) Deviation of measured OSPL from averaged levels (b) Deviation of measured OSPL from averaged levels

Figure 6: Analysis of deviation in measurements for fundamental peak for partial span-wise wake impingement *Left: 9 degree tilt; Right: 18 degree tilt*

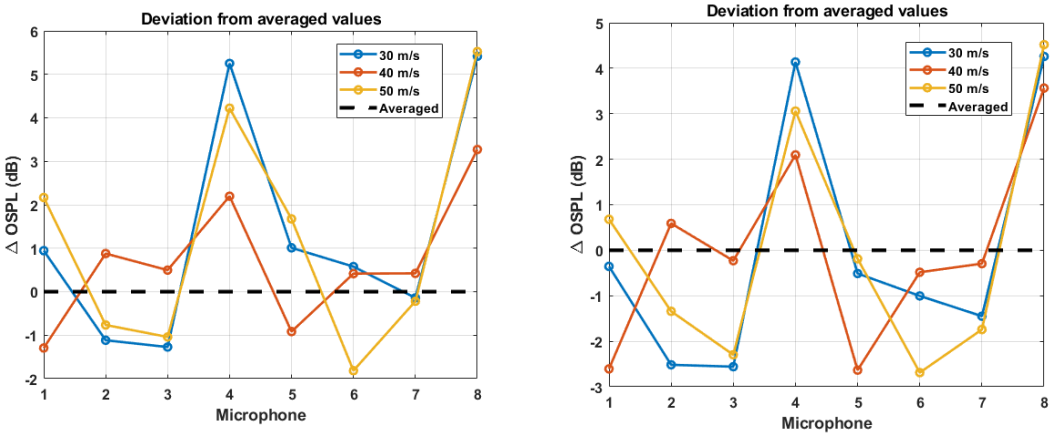

(a) Deviation of measured OSPL from averaged levels

(b) Deviation of measured OSPL from averaged levels

Figure 7: Analysis of deviation in measurements for strouhal range (0.1 - 0.42) for partial span-wise wake impingement *Left: 9 degree tilt; Right: 18 degree tilt*

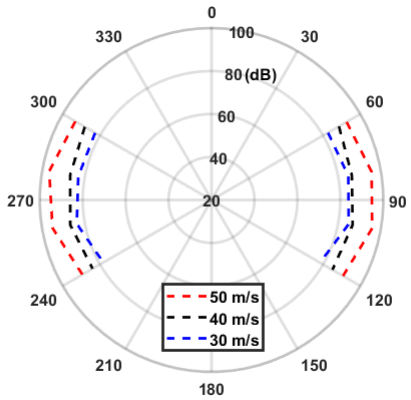

Figure 8: Directivity of partial spanwise wake impingement noise: vortex orientation of 81 degree

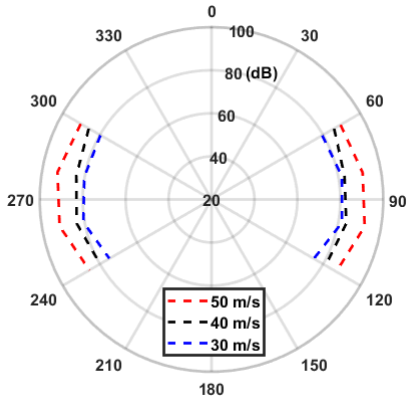

Figure 9: Directivity of partial spanwise wake impingement noise: vortex orientation of 72 degree

Appendix D

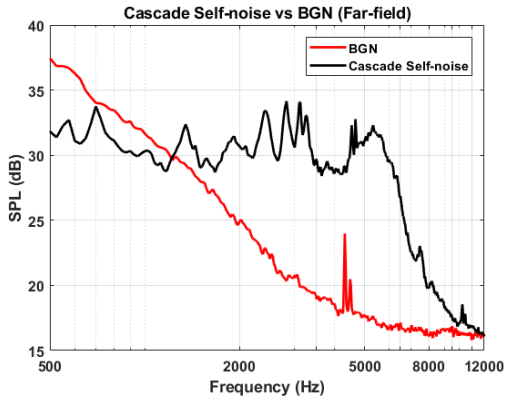

(a) Casacade self noise vs BGN (Far-field)

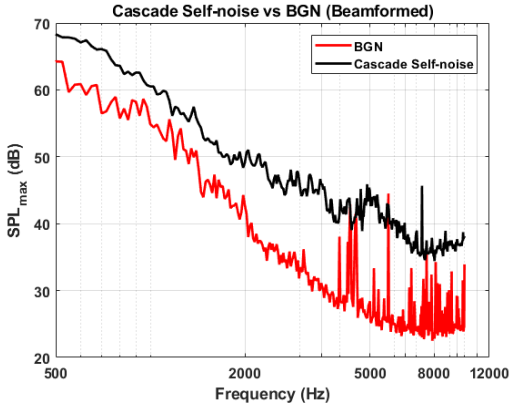

(b) Casacade self noise vs BGN (Beamformed)

Figure 10: Analysis of Cascade-Self noise vs BGN at 20 m/s

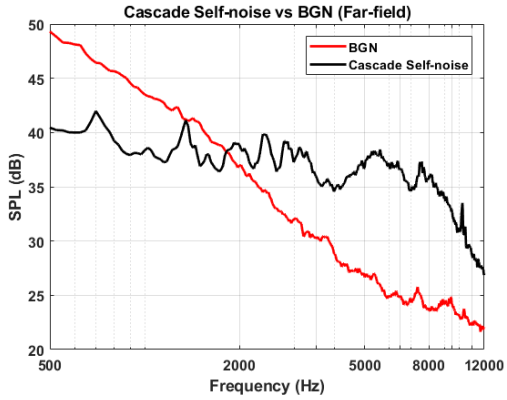

(a) Casacade self noise vs BGN (Far-field)

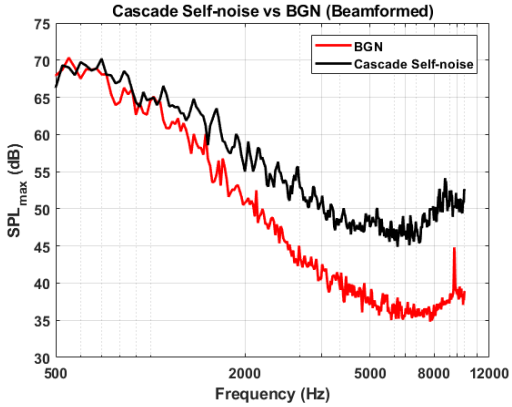

(b) Casacade self noise vs BGN (Beamformed)

Figure 11: Analysis of Cascade-Self noise vs BGN at 30 m/s

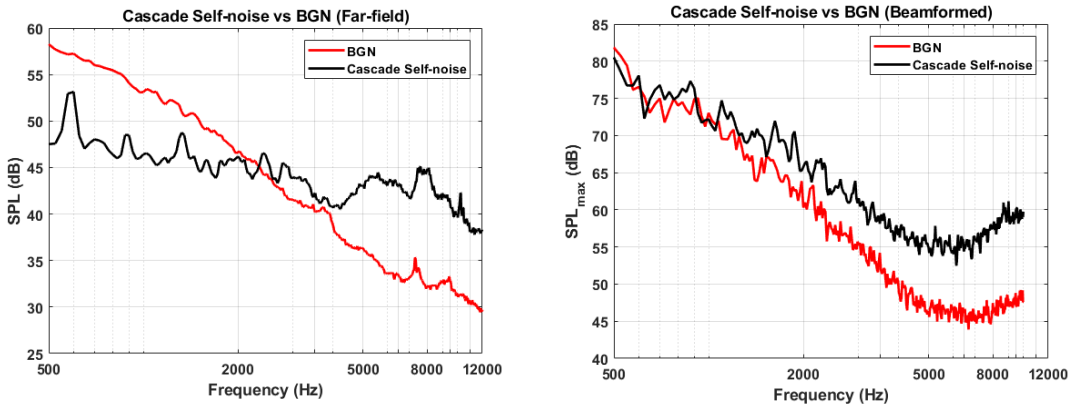

(a) Casacade self noise vs BGN (Far-field)

(b) Casacade self noise vs BGN (Beamformed)

Figure 12: Analysis of Cascade-Self noise vs BGN at 40 m/s

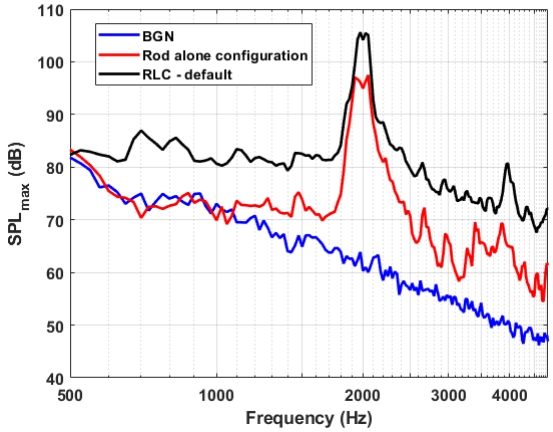

Figure 13: Comparison of rod alone configuration from beamformed data with the default configuration plotted along with the BGN at 40 m/s

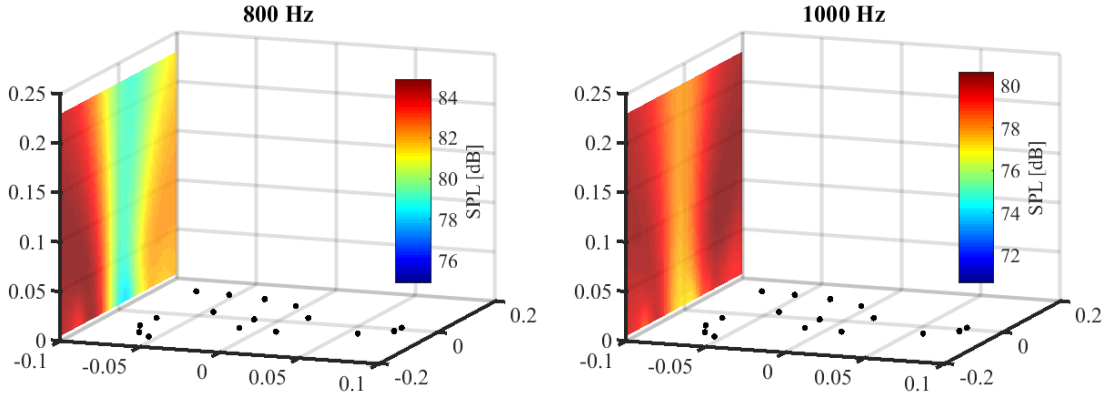

(a) Source map for default configuration at 800 Hz

(b) Source map for default configuration at 1000 Hz

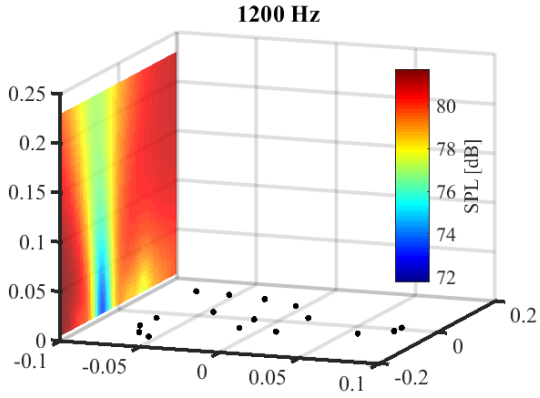

(c) Source map for default configuration at 1200 Hz

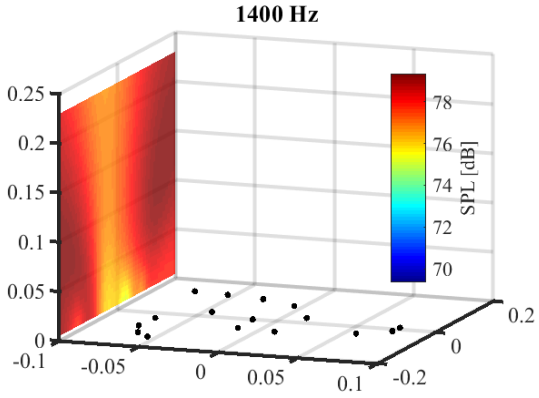

(d) Source map for default configuration at 1400 Hz

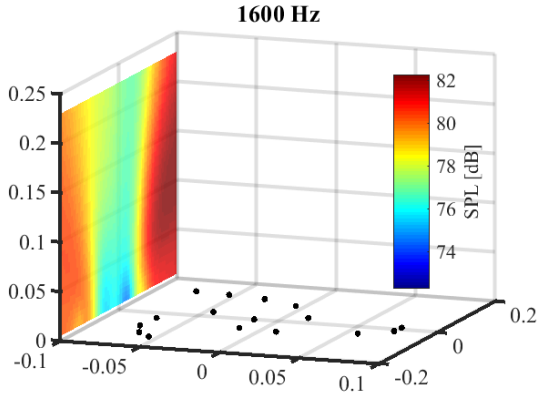

(e) Source map for default configuration at 1600 Hz

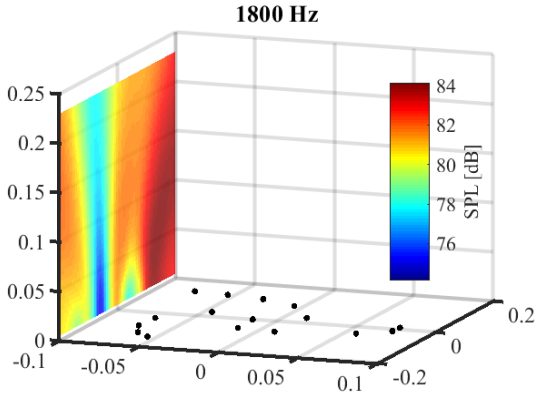

(f) Source map for default configuration at 1800 Hz

Figure 14: Analysis of beamformer performance at low frequencies

Bibliography

[1] B. Greschner and F. Thiele, "Wall modeled les simulation of rotor-stator-cascade broadband noise," in *17th AIAA/CEAS Aeroacoustics Conference (32nd AIAA Aeroacoustics Conference)*, p. 2873, 2011.

[2] A. Dankanich and D. Peters, "Turbofan engine bypass ratio as a function of thrust and fuel flow," 2017.

[3] C. Teruna, D. Casalino, D. Ragni, and F. Avallone, "Numerical analysis of a linear cascade model for rotor-stator interaction aeroacoustics," in *2018 AIAA/CEAS Aeroacoustics Conference*, p. 4189, 2018.

[4] R. K. Amiet, "Acoustic radiation from an airfoil in a turbulent stream," *Journal of Sound and vibration*, vol. 41, no. 4, pp. 407–420, 1975.

[5] J. K. Staubs, *Real airfoil effects on leading edge noise*. PhD thesis, Virginia Tech, 2008.

[6] R. Amiet, "Airfoil gust response and the sound produced by airfoil-vortex interaction," *Journal of sound and vibration*, vol. 107, no. 3, pp. 487–506, 1986.

[7] N. Curle, "The influence of solid boundaries upon aerodynamic sound," *Proc. R. Soc. Lond. A*, vol. 231, no. 1187, pp. 505–514, 1955.

[8] M. Howe, "Contributions to the theory of sound production by vortex-airfoil interaction, with application to vortices with finite axial velocity defect," *Proc. R. Soc. Lond. A*, vol. 420, no. 1858, pp. 157–182, 1988.

[9] R. K. Amiet, "Noise due to turbulent flow past a trailing edge," *Journal of sound and vibration*, vol. 47, no. 3, pp. 387–393, 1976.

[10] R. Paterson and R. Amiet, "Acoustic radiation and surface pressure characteristics of an airfoil due to incident turbulence," in *3rd Aeroacoustics Conference*, p. 571, 1976.

[11] S. Moreau and M. Roger, "Effect of angle of attack and airfoil shape on turbulence-interaction noise," in *11th AIAA/CEAS aeroacoustics conference*, p. 2973, 2005.

[12] P. Chaitanya, J. Gill, S. Narayanan, P. Joseph, C. Vanderwel, X. Zhang, and B. Ganapathisubramani, "Aerofoil geometry effects on turbulence interaction noise," *AIAA Paper*, vol. 2830, p. 2015, 2015.

[13] M. C. Jacob, J. Boudet, D. Casalino, and M. Michard, "A rod-airfoil experiment as a benchmark for broadband noise modeling," *Theoretical and Computational Fluid Dynamics*, vol. 19, no. 3, pp. 171–196, 2005.

[14] Y. Li, X.-n. Wang, Z.-w. Chen, and Z.-c. Li, "Experimental study of vortex–structure interaction noise radiated from rod–airfoil configurations," *Journal of Fluids and Structures*, vol. 51, pp. 313–325, 2014.

[15] J. Mayer, "Active change of permeable material properties for low-noise trailing edge applications," 2019.

[16] R. Parker, "Resonance effects in wake shedding from parallel plates: some experimental observations," *Journal of Sound and Vibration*, vol. 4, no. 1, pp. 62–72, 1966.

[17] S. Kaji and T. Okazaki, "Propagation of sound waves through a blade row: Ii. analysis based on the acceleration potential method," *Journal of Sound and Vibration*, vol. 11, no. 3, pp. 355–IN1, 1970.

[18] S. Kaji and T. Okazaki, "Propagation of sound waves through a blade row: I. analysis based on the semi-actuator disk theory," *Journal of Sound and Vibration*, vol. 11, no. 3, pp. 339–353, 1970.

[19] R. Amiet, "Transmission and reflection of sound by a blade row," *AIAA Journal*, vol. 9, no. 10, pp. 1893–1894, 1971.

[20] R. Amiet, "Transmission and reflection of sound by two blade rows," *Journal of Sound and Vibration*, vol. 34, no. 3, pp. 399–412, 1974.

[21] S. A. L. Glegg, "Airfoil self-noise generated in a cascade," *AIAA journal*, vol. 36, no. 9, pp. 1575–1582, 1998.

[22] N. Peake and E. Kerschen, "Influence of mean loading on noise generated by the interaction of gusts with a flat-plate cascade: upstream radiation," *Journal of Fluid Mechanics*, vol. 347, pp. 315–346, 1997.

[23] I. Evers and N. Peake, "On sound generation by the interaction between turbulence and a cascade of airfoils with non-uniform mean flow," *Journal of Fluid Mechanics*, vol. 463, pp. 25–52, 2002.

[24] M. Sabah and M. Roger, "Experimental study and model predictions of cascade broadband noise," in *7th AIAA/CEAS Aeroacoustics Conference and Exhibit*, p. 2243, 2001.

[25] H. Posson and M. Roger, "Experimental validation of a cascade response function for fan broadband noise predictions," *AIAA journal*, vol. 49, no. 9, pp. 1907–1918, 2011.

[26] A. Finez, M. Jacob, E. Jondeau, and M. Roger, "Experimental investigation of trailing-edge noise from a linear cascade of cambered airfoils," in *17th AIAA/CEAS Aeroacoustics Conference (32nd AIAA Aeroacoustics Conference)*, p. 2876, 2011.

[27] J. M. Tyler and T. G. Sofrin, "Axial flow compressor noise studies," tech. rep., SAE Technical Paper, 1962.

[28] S. Glegg and W. Devenport, *Aeroacoustics of low mach number flows: fundamentals, analysis, and measurement*. Academic Press, 2017.

[29] S. Discetti and A. Ianiro, *Experimental Aerodynamics*. CRC Press, 2017.

[30] B. D. Van Veen and K. M. Buckley, "Beamforming: A versatile approach to spatial filtering," *IEEE assp magazine*, vol. 5, no. 2, pp. 4–24, 1988.

[31] M.-H. Golbon-Haghighi, "Beamforming in wireless networks," in *Towards 5G Wireless Networks-A Physical Layer Perspective*, InTech, 2016.

[32] S. Oerlemans and P. Migliore, "Aeroacoustic wind tunnel tests of wind turbine airfoils," in *10th AIAA/CEAS Aeroacoustics Conference*, p. 3042, 2004.

[33] L. Rayleigh, "Xxxi. investigations in optics, with special reference to the spectroscope," *The London, Edinburgh, and Dublin Philosophical Magazine and Journal of Science*, vol. 8, no. 49, pp. 261–274, 1879.

[34] R. Merino Martinez, *Microphone arrays for imaging of aerospace noise sources*. PhD thesis, Delft University of Technology, 2018.

[35] S. Luesutthiviboon, "Design of an optimized acoustic array for aero-acoustic research in an open-jet anechoic wind tunnel," 2017.

[36] W. Humphreys, Jr, T. Brooks, W. Hunter, Jr, and K. Meadows, "Design and use of microphone directional arrays for aeroacoustic measurements," in *36th AIAA aerospace sciences meeting and exhibit*, p. 471, 1998.

[37] J. R. Underbrink, "Aeroacoustic phased array testing in low speed wind tunnels," in *Aeroacoustic measurements*, pp. 98–217, Springer, 2002.

[38] T. Mueller and M. Prasad, "Aeroacoustic measurements," *Applied Mechanics Reviews*, vol. 56, p. B66, 2003.

[39] V. Fleury, L. Coste, R. Davy, A. Mignosi, C. Cariou, and J.-M. Prosper, "Optimization of microphone array wall mountings in closed-section wind tunnels," *AIAA journal*, vol. 50, no. 11, pp. 2325–2335, 2012.

[40] S. Jaeger, N. Burnside, P. Soderman, W. Horne, and K. James, "Microphone array assessment of an isolated, 26%-scale, high-fidelity landing gear," in *8th AIAA/CEAS Aeroacoustics Conference & Exhibit*, p. 2410, 2002.

[41] V. Fleury, L. Coste, R. Davy, A. Mignosi, C. Cariou, and J.-M. Prosper, "Optimization of microphone array wall mountings in closed-section wind tunnels," *AIAA journal*, vol. 50, no. 11, pp. 2325–2335, 2012.

[42] R. Woodward, C. Hughes, R. Jeracki, and C. Miller, "Fan noise source diagnostic test–far-field acoustic results," in *8th AIAA/CEAS Aeroacoustics Conference & Exhibit*, p. 2427, 2002.

[43] A. L. Braslow, R. M. Hicks, and R. V. Harris, "Use of grit-type boundary-layer-transition trips on wind-tunnel models," 1966.

[44] T. F. Brooks and T. Hodgson, "Trailing edge noise prediction from measured surface pressures," *Journal of sound and vibration*, vol. 78, no. 1, pp. 69–117, 1981.

[45] T. F. Brooks, D. S. Pope, and M. A. Marcolini, "Airfoil self-noise and prediction," 1989.

[46] J. F. Williams and L. Hall, "Aerodynamic sound generation by turbulent flow in the vicinity of a scattering half plane," *Journal of fluid mechanics*, vol. 40, no. 4, pp. 657–670, 1970.

[47] E. Sarradj, "Three-dimensional acoustic source mapping with different beamforming steering vector formulations," *Advances in Acoustics and Vibration*, vol. 2012, 2012.

[48] S. Jaeger, W. Horne, and C. Allen, "Effect of surface treatment on array microphone self-noise," in *6th Aeroacoustics Conference and Exhibit*, p. 1937, 2000.

[49] J. B. Barlow, W. H. Rae Jr, and A. Pope, "Low speed wind tunnel testing," *INCAS Bulletin*, vol. 7, no. 1, p. 133, 2015.

[50] R. Amiet, "Refraction of sound by a shear layer," *Journal of Sound and Vibration*, vol. 58, no. 4, pp. 467–482, 1978.

[51] R. H. Schlinker and R. K. Amiet, "Refraction and scattering of sound by a shear layer," *The Journal of the Acoustical Society of America*, vol. 70, no. 6, pp. 1797–1799, 1981.